HABILITATION À DIRIGER DES RECHERCHES
DE
L'UNIVERSITÉ DE LILLE 1

Spécialité : **Sciences pour l'ingénieur**

présentée par

Michaël BAUDOIN

Acoustofluidique micro-échelle

Soutenance prévue le **16 Novembre 2015** devant le jury composé de

M.	José	**BICO**	ESPCI	Rapporteur
M.	Olivier	**BOU MATAR**	Ecole Centrale de Lille	Garant
M.	Ayache	**BOUAKAZ**	Inserm	Rapporteur
M.	Henrik	**BRUUS**	DTU	Examinateur
M.	Lionel	**BUCHAILLOT**	CNRS	Invité
M.	Benjamin	**DOLLET**	CNRS	Rapporteur
M.	Jacques	**MAGNAUDET**	CNRS	Examinateur
M.	Philippe	**PERNOD**	Ecole Centrale de Lille	Invité
M.	Stéphane	**ZALESKI**	Université Paris 6	Examinateur
M.	Farzam	**ZOUESHTIAGH**	Université Lille 1	Examinateur

Table of contents

Chapitre 1

Introduction

1.1 Summary

Since most micro-flows are incompressible, one might think that acoustics and microfluidics are two disconnected fields. In fact, acoustic waves and micro-flows can interact in many ways. For example, when acoustic waves propagate in suspensions of particles in the so-called long wavelength regime (that is to say when the size of the particles is much smaller than the wavelength), incompressible micro-flows around particles can dramatically alter the amplitude and phase of the acoustical wavefield. In this first case, coupling occurs due to the difference of length scales involved in the problem leading to compressible flows at the scale of the acoustic wave and incompressible flows at the scale of the particles. Then, nonlinear effects such as acoustic streaming and radiation pressure can be used to control microfluidics flows or manipulate particles and cells. In this second case, coupling occurs due to nonlinear cumulative effects that create a link between fast time scale (acoustic wave) and slow time scale (fluid flow or interface deformation). Finally fast interfacial microfluidic flows like soap bubbles popping or the rupture of liquids plugs in microchannels can generate sound due to the very short characteristic time scales associated with interfacial ruptures that create pressure discontinuities and thus sound sources.

All these phenomena are involved in a multitude of natural and engineered systems such as the propagation of sonic boom in the atmosphere, acoustic spectroscopy, acoustical tweezers, micro-TAS, the rupture of soap bubbles or pulmonary obstructive diseases. In this manuscript, we investigate the tremendous possibilities offered by acoustic-microfluidic interactions, not only to improve our knowledge of complex phenomena but also to solve some engineering or health issues and develop original microsystems.

A significant part of my research work in the last 10 years has been devoted to the study of multiple scattering of acoustic waves by suspensions of particles, in particular for concentrated particles with strong particle-particle micro-hydrodynamic interactions. The theories developed have been applied in the field of nanoparticles spectroscopy and the alteration of sound propagation induced by atmospheric clouds. Nevertheless since most of this work is discussed at length in my PhD thesis manuscript, it will not be reproduced here. The first scientific chapter of this manuscript is thus dedicated to the use of surface acoustic waves (SAWs) and nonlinear phenomena for microfluidic flow control and in particular the investigation of the potential of specific wavefields called acoustical vortices to achieve vorticity control and 3D single particle manipulation in fluid samples. The second chapter is dedicated to the sound produced by interfacial micro-flows. In particular the catastrophic dynamics of liquid plugs rupture in a binary network is studied in connection with some pulmonary obstructive diseases. The sound produced by interface rupture is then studied on the more academic case of soap bubble bursting.

This manuscript does not summarize all my research activities since it focuses mainly on microfluidic-acoustic interactions. For example our recent work with F. Zoueshtiagh on the controlled formation of cylindrical armoured bubbles in capillaries [1] is not presented here. But there is still a chance that we find some interesting phenomena related to vibrations in this area before the defense...

1.2 Acknowledgements

This work is the result of collaborations both inside and outside IEMN and involves the participation of very gifted undergraduates, master, PhD students. It has strongly benefited from all these interactions.

On the scientific aspects, I would like to thank Jean-Louis Thomas, my former PhD advisor and now collaborator on the AWESOM ANR project. He still remains one of the researchers I most admire, not only for his high general knowledge of physics, his ability to design experiment that always work along with relevant associated theories but mostly because of his real passion for science. Discussions with Jean-Louis are always extremely valuable. Then I would like to thank François Coulouvrat, Charles Baroud and Paul Manneville, all former PhD and Postdoc mentors. I learned a lot by working them, both on scientific and management aspects. More recently, it has been a pleasure to work with Alan Renaudin, Maria Isabel Rocha Gaso, Frederic Sarry and Denis Beyssen on the AWESOM ANR project, Jason Butler and Christine Faille on the armored bubbles problems, Olivier Coutier on bubbles cavitation, and Regis Wunenburger, Arnaud Antkowiak and François Olivier on the sound produced by bubbles break up.

Concerning master, PhD and postdoc student, I must say that I have been extremely lucky to find so nice, talented and hard working collaborators. So thanks to Adrien Bussonière for his work on the physics of droplet actuation by SAW and biological applications, Antoine Riaud for his work on acoustical vortices, Ilyesse Bihi for his work on fingering capillary instability driven by particles, Stephanie Signé Mamba, Juan Carmelo Magniez and Chang Liu for their work on liquid plugs in networks, Nicolas Chastrette for his work on the origin of droplet interfacial instability induced by SAW, and finally Johny Jose and Gaurav Prabhudesai for their work on armored bubbles. A major part of the work presented in this manuscript is theirs.

This work has also strongly benefited from the high quality environment at IEMN (the clean-room facilities, our new microfluidic experimental facilities but also from the various skills that are gathered in this laboratory).

In particular, I would like to thank Philippe Pernod, who is a nice, honest and righteous group leader. He always think about the group interest first and this is for sure the origin of the good atmosphere in the group. Then I would especially like to thank Farzam Zoueshtiagh, Olivier Bou Matar, Philippe Brunet and Alain Merlen for welcoming me in the group and helping me financially and scientifically to start my projects. Nothing would have been possible without their support. I would also like to thank my "office-mate" Stefano Giordano, who is one of the most gifted (and nice) researchers I know. He helped me to solve many of my mathematical and physical problems even if his research field is quite different from mine. I must also underline that the nice environment at IEMN is also the result of the involvement of many engineers, technicians, secretaries, accountants, managers... that help you daily in all the technical aspects of your projects. So thanks to Helène Delsarte, Marie Lefranc, Nathalie Haye, Farha Bensafia, Sandrine Fugère, Alice Jendrzekczak, Hervé Avelin, Sylvie Laby, Nora Benbahlouli, Pascal Delmotte, Damien Ducatteau, François Neuily, Véronique Labbé, David Guerin, Gauthier De Smet, Mickael Masquelin,... for their help. Finally, I would like to thank Lionel Buchaillot, the Director of IEMN, for always supporting me in my projects and helping our microfluidic team to integrate IEMN in excellent conditions.

From the family side, I would like to thank my browther Emmanuel, that is always there when I need him (especially every year, when we decide to rent or buy a new house), my sons Yann and Maël who help me think about something else than science and equations when I come back home, my parents for everything (since the birth of my children, each day I understand better all they have done for me), and last but not least, my wife Marie, for her support, even at late hour, even during week-ends or "holidays" when I have work to finish. She sometimes knows better than me the content of my manuscripts and presentations.

Finally, I would like to express my gratitude to the jury, Dr. José Bico, Pr. Olivier Bou Matar, Dr. Ayache Bouakaz, Pr. Henrik Bruus, Dr. Lionel Buchaillot, Dr. Benjamin Dollet, Dr. Jacques Magnaudet, Pr. Philippe Pernod, Pr. Stéphane Zalesky and Pr. F. Zoueshtiagh for accepting to review this HDR and attend its defense.

Chapitre 2

Curriculum Vitae

Michaël Baudoin,
34 years old,
Université Lille 1 / IEMN,
Avenue Poincaré,
59652 Villeneuve d'Ascq cedex, France,
+33 (0)3 20 19 79 58,
michael.baudoin@univ-lille1.fr,
http://films-lab.univ-lille1.fr/michael/

Current position

Assistant Professor at Université Lille 1 (France) and researcher at IEMN laboratory. My research activities mainly focus on microscale acoustofluidics that is to say subjects at the interface between acoustics, microfluidics and microsystems :

— **Design and physical study of microsystems based on surface acoustic waves for the control of fluids (biological, chemicals) at microscales**. In particular we study the highly nonlinear coupling between acoustic waves and the flows and/or interfacial deformations they produce.

— **Study of the sound produced by microfluidic two-phase flows.** In particular we aim at improving the physical understanding of the sound produced by the rupture of liquid plugs in pulmonary airways due to obstructive pulmonary diseases. Such knowledge might greatly improve their diagnosis.

— **Multiple scattering of acoustic waves by dense suspensions of particles** both for the design of new acoustic materials but also the characterization of suspensions (spectroscopy)

Responsibilities

International

2015 **Member of the organizing committee (5 people) of an international Summer School entitled "Microfluidics'15"**, Porquerolles, France, 21 to 26 june 2015 (all courses in English, speakers from France, Germany, United States and Denmark)

- Organizer and Chair of the short talk session
- Organizer and Chair of the poster session

2012 **Member of the organizing committee (4 people) of an international workshop entitled "Acoustic waves for the control of microfluidic flows"**, Lorentz Center, the Netherlands, 23 to 27 april 2012

- Objective : bring together international experts of different scientific communities (physics of fluids, acoustics, microsystems) to improve our understanding of microfluidic actuators based on acoustic waves
- 52 participants from 12 different countries

2011 **Member of the organizing committee (3 people) of an international summer school entitled "Lab-based Workshop on bubbles and drops"**, University of Florida, 20 to 25 june 2011

- Funding : American NSF-PIRE program
- Participants : 30 researchers, PhD students and MSc students from US, France and Japan

National

Since 03/2015 **Member of the "GDR Microfluidique" steering committee**

2011-2015 **Member of the National Board of French Universities** (CNU)

- Evaluation of the applicants for Assistant Professor qualification
- Evaluation of the assistant and Associate Professors applying for promotions
- Participation in the collegial decisions concerning the evolution of French Universities

Local

Since 05/2015 **Member of the "UFR de Mathématique" board**

Since 09/2014 **Director of undergraduate studies in mechanics** (125 students)

- Complete reorganization of the training in mechanics to obtain a more attractive, coherent and efficient program
- Creation of partnerships with companies working in the field of mechanics (PSA - ONERA - NUMECA - CENAERO)
- Daily management of the undergraduate studies in mechanics

Since 09/2014 **Head of the Master of Engineering in Mechanics (CMI)**, a selective program with additional activities to prepare students to the job of scientific expert in companies

- A Master of Engineering in France can obtain the CMI label only after examination of the project by a national commission. I developed the project with the help of the professors of my department and defended it to obtain the label
- Organization of the additional activities

Current and past fundings

2012-2016 **Coordinator (with the support of Pr. Olivier Bou Matar) of the ANR project "AWESOM"**, which aims at developing a Lab on a Chip based on hybrid technologies for the manipulation and characterization of biofluids

- Partnership between 5 French and Canadian institutes (IEMN / Université Lille 1, INSP / Université Paris 6, IJL / Université de Nancy, UMI-LN2 /Université de Sherbrooke, MSC / Université Paris 7)
- Grant from the French National Agency for Research (ANR) / Amount : **532 k€**

2011-2018 **Obtention of 5 grants for PhD students working on my research activities** from (i) the Region "Nord-Pas-de-Calais", (ii) the French General Directorate for Armament (DGA), (iii) the University of Lille and (iv) the "Ecole Normale Supérieure"

- Total amount of the grants : **486 k€**

Supervision

Supervision of 5 PhD students :

- *Adrien Bussonière (2011-2014)* (50%)
  — Subject : "SAW microsystems for microfluidics : from physical understanding to biological applications"
- *Ilyesse Bihi (2012-...)* (25%)
  — Subject : "Removal of particles and spores from food production lines with bubbles and/or droplets"
- *Antoine Riaud (2013-...)* (33%)
  — Subject : "Hybrid lab on a chip for the manipulation and characterization of biological fluids : potential of inverse filter for versatile platform"
- *Stéphanie Signé Mamba (2014-...)* (75%)
  — Subject : "From the dynamics of liquid plugs in synthetic microfluidics networks to the diagnosis and treatment of pulmonary obstructive diseases"
- *Juan Carmelo Magniez (2014-...)* (75%)
  — Subject : "Two-phase flows in microfluidics complex networks"

Supervision of 5 master students

Review of PhD, projects and papers

08/2014	**Reviewer of D.J. Collins PhD**, entitled "Manipulation in microfluidics systems using Surface Acoustic Waves (SAW)", Monash University, Australia
08/2013	**Grant review panelist for the DFG** (German Research Funding Agency)
12/2013	**Member of the jury of T. Roux-Marchand** entitled "SAW microfluidics systems : from DNA replication to PCR", Université de Lorraine, France
05/2013	**Extern member** of an appointment committee for an Assistant Professor position in "Fluid Biomechanics", UTC Compiègne, France
2008-...	**Scientific content reviewer for peer-reviewed publications including :** New Journal of Physics, Journals of Micromechanics and Microengineering, Sensors and Actuators B, Acta Acustica united with Acustica, Soft Matter, Langmuir, Journal of the Acoustical Society of America, Journal of Fluids Engineering, Lab on a Chip, Measurement Science and Technology, Proceedings of the Royal Society A, Advanced Functional Materials.

Honors and awards

2014	**Front cover of "Soft Matter" journal (IF : 4,1)** for our work on the controlled synthesis of armored bubbles. Our paper entitled "Capillary tube wetting induced by particles : towards armoured bubbles tailoring" has also been highlighted as one of the hot papers of the year.
2013	**Distinguished by the national award for excellence in research (PES)**

Education

2008	**Postdoctoral fellow in microfluidics, Ecole Polytechnique, LadHyX** — Subject : "Dynamics of liquid plugs in microfluidic networks" — Advisors : C. Baroud et P. Manneville
2004/07	**PhD in Acoustics and Fluid Mechanics, Université Paris 6** — Delivered the 11th January 2008 — Thesis topic : "Nonlinear acoustics and multiple scattering in suspensions of rigid particles — Advisors : F. Coulouvrat (d'Alembert) and J.L. Thomas (INSP)
2003/04	**MSc in Fluid Mechanics at Université Paris 6 with First Class Honours**
2001/04	**MSc in Mechanical Engineering at ENSTA**
1999/01	**Undergraduate studies at lycée Lakanal and lycée Henri IV**

Skills

Language proficiency	**English :** fluent (TOEIC : 970/990) **German :** basics **French :** native language

Informatics and numerics	**Numerical methods :** finite elements, finite differences, optimization **Programming languages :** C/C++, Java, HTML **Softwares :** COMSOL, ANSYS, Gerris, Maple, Matlab **Operating systems :** Windows, Linux, Mac OS X
Experimental skills	**Clean room proficiency :** Fabrication of microchannels in PDMS with soft-lithography technics - Fabrication of interdigitated fingers (soft lithography, metal sputtering, ...) on piezoelectric substrates for the the synthesis of surface acoustic waves **Microfluidics :** High-speed imaging **Acoustics :** Synthesis of complex acoustic wavefields with inverse filter method **Chemistry :** Synthesis of silica nanoparticles

Past and current collaborators

— **C. Baroud** Professor, Laboratoire d'Hydrodynamique (LadhyX), Ecole Polytechnique, FRANCE
— **H. Bruus** Professor, DTU, DENMARK
— **J. Butler**, Professor, University of Florida, UNITED STATES
— **C. Chanéac**, Professor, Laboratoire de Chimie de la Matière Condensée, Université Paris 6, FRANCE
— **F. Coulouvrat**, CNRS Director of research, Institut Jean le Rond d'Alembert, Université Paris 6, FRANCE
— **O. Coutier**, Professor, Laboratoire de Mécanique de Lille, FRANCE
— **C. Faille**, INRA Director of research, FRANCE
— **P. Manneville**, CNR Director of research, Laboratoire d'Hydrodynamique (LadhyX), Ecole Polytechnique, FRANCE
— **A. Renaudin**, Assistant Professor, Laboratoire de Biophotonique et d'Optoélectronique, University of Sherbrooke, CANADA
— **J.L. Thomas**, CNRS Director of research, Institut des NanoSciences de Paris, Université Pierre et Marie Curie, FRANCE

Publications and conferences

All the following publications can be downloaded at the following address :
http://films-lab.univ-lille1.fr/michael/

A. Publications in peer-reviewed international journals

The corresponding authors are underlined.

Submitted

- [**A14**] A. Bussonière, **M. Baudoin**, P. Brunet and O. Bou Matar, Dynamics of sessile and pendant drop excited by surface acoustic waves : gravity effects and correlation between oscillatory and translational motions, *submitted to Phys. Fluids*, October 2015
- [**A13**] A. Riaud, J.L. Thomas, **M. Baudoin** and O. Bou Matar, Taming the degeneracy of Bessel beams at anisotropic-isotropic interface : toward 3D control of confined vortical waves, *submitted to Phys. Rev. X*, September 2015

2015 (Accepted)

- [**A12**] A. Riaud, J.L. Thomas, E. Charron, A. Bussonière, O. Bou Matar and **M. Baudoin**, Anisotropic swirling surface acoustic waves synthesis by inverse filter for on-chip generation of acoustical vortices, *Accepted for publication in Phys. Rev. Appl.*, August 2015

2014

- [**A11**] F. Zoueshtiagh, **M. Baudoin**, D. Guerrin, Capillary tube wetting induced by particles : towards armoured bubbles tailoring, *Soft Matter*, 10(47) : 9403-9412, 2014
- [**A10**] A. Bussonière, Y. Miron, **M. Baudoin**, O. Bou-Matar, M. Grandbois, P. Charette, and A. Renaudin, Cell detachment and label-free cell sorting using modulated surface acoustic waves in droplet-based microfluidics, *Lab on a chip*, 14 : 3556, 2014
- [**A9**] A. Riaud, **M. Baudoin**, J.-L. Thomas, O. Bou-Matar, Cyclones and attractive streaming generated by acoustical vortices, *Phys. Rev. E*, 90 : 013008, 2014

2013 — [**A8**] **M. Baudoin**, Y. Song, P. Manneville, C.N. Baroud, Airways re-opening through catastrophic events in a hierarchical network, *Proc. Nat. Ac. Sci. (IF : 9,7), 110 : 859-864, 2013*

2012 — [**A7**] **M. Baudoin**, P. Brunet, O. Bou-Matar, E. Herth, Low power sessile droplet actuation via modulated surface acoustic waves, *Appl. Phys. Lett.*, 100 : 154102, 2012

2011 — [**A6**] **M. Baudoin**, F. Coulouvrat, J.-L. Thomas, Clouds impact on the attenuation of sound, ultrasound and sonic boom, *J. Acoust. Soc. Am.*, 130 : 1142-1153, 2011

— [**A5**] **M. Baudoin**, J.-L. Thomas, F. Coulouvrat, C. Chanéac, Scattering of ultrasonic shock wave in suspensions of rigid particles, *J. Acoust Soc. Am.*, 129 : 1209-1220, 2011

— [**A4**] Y.Song, **M. Baudoin**, P. Manneville and C.N. Baroud, The air-liquid flow in a microfluidic airway tree, *Medical Engineering and Physics*, 33 : 849-456, 2011

(2010) — [**A3**] P. Brunet, **M. Baudoin**, O. Bou Matar, F. Zoueshtiagh, Droplet displacement and oscillations induced by ultrasonic surface acoustic waves : a quantitative study, *Phys. Rev. E*, 81 : 026315, 2010

(2008) — [**A2**] **M. Baudoin**, J.L. Thomas, F. Coulouvrat, On the influence of spatial correlations on sound propagation in concentrated solutions of rigid particles, *J. Acoust. Soc. Am*, 123 : 4127-4139, 2008

(2007) — [**A1**] **M. Baudoin**, J.L. Thomas, F. Coulouvrat, D. Lhuillier, An extended coupled phase theory for the sound propagation in polydisperse concentrated suspensions of rigid particles, *J. Acoust. Soc. Am*, 121 : 3386-3397, 2007

B. Invited international conferences and invited lectures at international summer schools

— **[B5]** **M. Baudoin**, invited for an extended presentation, *IEEE International Ultrasonic Symposium, 21-24 october 2015, Taipei (Taiwan)*
— **[B4]** **M. Baudoin**, Lecture on "Nonlinear acoustics for microfluidics", *CNRS Summer School on "Nonlinear acoustics in complex media", 1-6 june 2014, Oleron (France)*
— **[B3]** **M. Baudoin**, P. Brunet, O. Bou Matar, Low power sessile droplet actuation via modulated surface acoustic waves, *Acoustics 2012 Hong Kong, joint conference from ASA, ASC, WESPAC and HKIOA*, 13-18 may 2012, Hong Kong (China)
— **[B2]** **M. Baudoin**, 3 Lectures on Interfacial flows, *Lab-based workshop on bubbles an drops, University of Florida, 20-25 june 2011*
— **[B1]** **M. Baudoin**, P. Brunet, O. Bou Matar, Droplet motion and deformation induced by SAW, *6th IEEE-NEMS Conference*, 20-23 february 2011, Kaohsiung (Taiwan)

C. International conferences

The conference speaker is underlined.

— **[C22]** A. Riaud, **M. Baudoin**, J.L. Thomas, O. Bou Matar, Acoustical twisting, *Condensed Matter in Paris*, 24-29 august 2014, Paris (France)
— **[C21]** **M. Baudoin**, Y. Song, P. Manneville, C.N. Baroud, Airways reopening through catastrophic events in a hierarchical network, *Flow 2014 Conference*, Twente (The Netherlands)
— **[C20]** A. Bussonière, A. Renaudin, Y. Miron, M. Grandbois, **M. Baudoin** and P. Charette, Removal of living cells from biosensing surfaces in droplet based microfluidics using surface acoustic waves, *ICA 2013*, joint meeting from the Acoutical Society of America and the Canadian Acoustical Association, 2-7 june 2013, Montreal (Canada)
— **[C19]** **M. Baudoin**, P. Brunet, O. Bou-Matar and E. Herth, Sessile droplet resonances and low power SAW actuation, *USWNET 2012 Conference*, 21-22 september 2012, Lund (Sweeden)
— **[C18]** P. Brunet, **M. Baudoin**, O. Bou-Matar, Drops subjected to surface acoustic waves : flow dynamics *APS 65th annual DFD Meeting*, 18-20 november 2012, San Diego (US)

— **[C17]** P. Brunet, **M. Baudoin**, O. Bou Matar, E. Herth, F. Zoueshtiagh, On the influence of viscosity on droplet actuation by surface acoustic waves, *2nd European Conference on Microfluidics*, 8-10 december 2010, Toulouse (France)

— **[C16]** **M. Baudoin**, Y. Song, P. Manneville, C. Baroud, Airways reopening through cascades of plug ruptures in a binary network, *Multiflow*, 8-10 november 2010, Brussel (Belgium)

— **[C15]** P. Brunet, **M. Baudoin**, O. Bou Matar, F. Zoueshtiagh, Droplet motion and deformation induced by acoustic streaming and radiation pressure, *20th International Congress on Acoustics*, 23-27 august 2010, Sydney (Australia)

— **[C14]** P. Brunet, **M. Baudoin**, O. Bou Matar, F. Zoueshtiagh, Drop diplacement and deformation induced by surface acoustic wave, *5th Conference of the International Marangoni Association*, 7-10 june 2010, Florence, Italy

— **[C13]** **M. Baudoin**, F. Coulouvrat and J.L. Thomas Infrasound absorption by atmospheric clouds *EGU general assembly*, 2-7 may 2010, Vienna (Austria)

— **[C12]** P. Brunet, **M. Baudoin**, O. Bou Matar, F. Zoueshtiagh, Droplet mixing and displacement by surface acoustic wave, *Ultrasonic Standing Wave Network Conference 2009*, 30 November-1st december 2009, Stokholm (Sweeden)

— **[C11]** P. Brunet, **M. Baudoin,**, F. Zoueshtiagh, A. Merlen, Drop mixing and diplacement by surface acoustic wave, *French/Chinese conference on microfluidics*, 11-15 october 2009, Paris (France)

— **[C10]** Y. Song, **M. Baudoin**, P. Mannevile and C.N. Baroud, *2nd French-Chinese Conference on Microfluidics*, The air liquid flow in a microfluidic airway tree, 11-15 october 2009, Paris (France)

— **[C9]** P. Brunet, **M. Baudoin,**, F. Zoueshtiagh, A. Merlen, Drop mixing and diplacement by surface acoustic wave, *International workshop Bubble and Drop Interfaces*, 23-25 september 2009, Thessaloniki (Greece)

— **[C8]** Y. Song, **M. Baudoin,**, P. Manneville, C. Baroud, The air-liquid flow in a microfluidic airway tree, *2nd Micro and Nano Flows Conference*, 1-2 september 2009, London (UK)

— **[C7]** **M. Baudoin**, Y. Song, C. Baroud, P. Manneville, Microscopic airways reopening through cascades of plug ruptures, *7th International Conference on Nanochannels, Microchannels and Minichannels*, 22-24 juin 2009, Pohang (South Corea), CDROM, ISBN : 978-0-7918-3850-1

— **[C6]** **M. Baudoin**, Y. Song, P. Manneville and C.N. Baroud, Reopening of a microfluidic airway tree in the presence of liquid plugs., *61st Annual Meeting of the APS Division of Fluid Mechanics*, 23-25 November 2008, San Antonio, Texas (US) (Bulletin of the American Physical Society, vol. 53, n° 15, p. 115)

— **[C5]** **M. Baudoin**, Y. Song, P. Manneville and C.N. Baroud, The air-liquid flow in bifurcating newtorks of micro-channels, *7th Euromech Fluid Mechanics Conference*, 14-18 september 2008, Manchester (Angleterre)

- **[C4] M. Baudoin**, J.L. Thomas, F. Coulouvrat, C. Chanéac, Acoustic shock wave propagation through solutions of nanoparticles, *18th International Symposium on Nonlinear Acoustics*, 7-10 july 2008, Stockholm (Sweeden), AIP Conf. Proc. 1022, 241-244"

- **[C3] M. Baudoin**, J.L. Thomas, F. Coulouvrat, D. Lhuillier, A self-consistent effective medium theory for the sound propagation in concentrated suspensions of rigid particles, *19th International Congress on Acoustics*, 2-7 september 2007, Madrid (Spain), CDROM, ISBN : 84-87985-12-2

- **[C2]** J.L. Thomas, F. Coulouvrat, R. Marchiano, **M. Baudoin**, L. Ganjehi, Experimental simulation of the sonic boom at the laboratory scale, *19th International Congress on Acoustics*, 2-7 september 2007, Madrid (Spain), CDROM, ISBN : 84-87985-12-2

- **[C1] M. Baudoin**, F. Coulouvrat, J.L. Thomas, Absorption of sonic boom by clouds, *17th International Symposium on Nonlinear Acoustics*, 18-22 july 2005, Penn-State (US), AIP Conf. Proc. 838, 619 (2006),

D. National conferences

- **[D6] M. Baudoin**, A. Riaud, J.L. Thomas, O. Bou Matar, Cyclones and attractive streaming generated by acoustical vortices, *Journée nationale du GDR "Micro/Nano-Systèmes et Micro/nano- Fluidique*, 7-8 july 2014 (France)
- **[D5] M. Baudoin**, J.-L. Thomas et F. Coulouvrat, Influence des nuages sur l'atténuation du son, des infrasons et du bang sonique, *10ème Congrès Français d'Acoustique*, 12-16 april 2010, Lyon (France), CDROM

- **[D4]** P. Brunet, **M. Baudoin**, O. Bou Matar, F. Zoueshtiagh, Déformation de gouttes par ondes acoustiques de surface, *10ème Congrès Français d'Acoustique*, 12-16 april 2010, Lyon (France), CDROM

- **[D3]** P. Brunet, **M. Baudoin**, O.B. Matar, F. Zoueshtiagh, Déplacement et oscillations de gouttes sous l'effet d'ondes de surface ultrasonores, *Résumé des exposés de la 13ème Rencontre du Non-Linéaire*, 13 january 2010, Paris (France)

- **[D2] M. Baudoin**, J.L. Thomas, F. Coulouvrat, D. Lhuillier, Un modèle diphasique self-consistant pour la propagation du son dans les solutions concentrées de particules rigides *18ème Congrès Français de Mécanique*, 27-31 august 2007, Grenoble (France), CDROM (CFM2007-1129)

- **[D1] M. Baudoin**, F. Coulouvrat, J.L. Thomas, Propagation d'ondes de choc dans des suspensions diluées, *8ème Congrès Français d'Acoustique*, 24-26 april 2006, Tours (France), CDROM

E. Invited seminars in French laboratories

— **[E4]** **M. Baudoin**, Y. Song, P. Manneville, C.N. Baroud, Cascade of plug ruptures : from milk-shake to pumonary airways, *Laboratoire Gullivaire, ESPCI*, 1st october 2012

— **[E3]** **M. Baudoin**, Y. Song, P. Manneville, C.N. Baroud, Cascades de ruptures de ponts liquides : du milk-shake à l'arbre pulmonaire, *Laboratoire Transferts, Interfaces et Procédés, Université Libre de Bruxelle*, 10 june 2011

— **[E2]** **M. Baudoin**, Y. Song, P. Manneville, C.N. Baroud, Cascades de ruptures de ponts liquides : du milk-shake à l'arbre pulmonaire, *Institut de Physique de Rennes, Université de Rennes 1*, 21 october 2011

— **[E1]** **M. Baudoin**, Y. Song, P. Manneville, C.N. Baroud, Cascades de ruptures de ponts liquides : du milk-shake à l'arbre pulmonaire, *Institut Jean le Rond d'Alembert, Université Paris 6*, 21 october 2010

Chapitre 3

Microfluidic control with acoustics

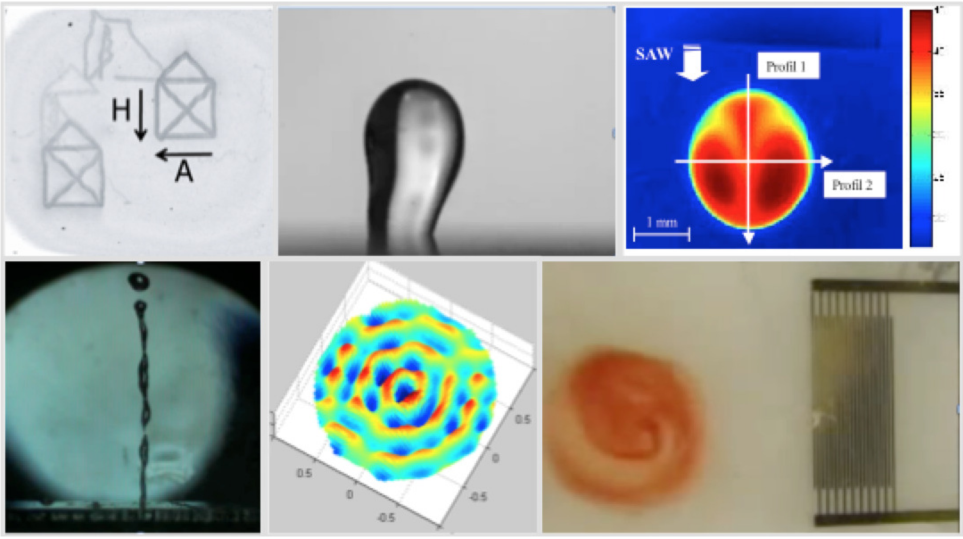

FIGURE 3.1: Stack of images illustrating the numerous possibilities offered by SAWs for microfluidic actuation.

3.1 Introduction

Since the early development of microfluidics, researchers have explored the possibilities offered by acoustics for the precise manipulation of fluids samples, particles and cells. Acoustic actuation is achieved through nonlinear effects since linear acoustic cannot result in any time average net movement. The main nonlinear effects used in microscale acoustofluidics are the so-called "acoustic streaming" and "acoustic radiation pressure".

Acoustic streaming is a fluid flow resulting from the nonlinear transfer of energy from the acoustic irrotational mode to the viscous incompressible mode of linearized Navier-Stoke equations.

Indeed, when an acoustic wave is attenuated, a part of the dissipated energy is transferred into heat and the other part into flow. In liquids, most of the energy is (at least initially) transformed into flow. Different forms of streaming are generally distinguished according to the underlying dissipation mechanism [2, 3]. *Boundary layer-driven streaming* [4] arises due to dissipation inside the viscous boundary layer when an acoustic wave impinges a fluid/solid interface. This form of streaming can be decomposed between *inner streaming*, also called Schlichting streaming [5], occurring inside the viscous boundary layer and counter rotating *outer streaming* outside it [6]. The former is not exclusive to acoustics since it does not require compressibility of the fluid but only the relative vibration of a fluid and a solid. The latter, first enlightened by Lord Rayleigh, can be seen either as the fluid entrainment outside the boundary layer induced by Schlichting streaming or as a consequence of the tangential velocity continuity requirement for an acoustic wave at a fluid/solid boundary. Finally *bulk streaming*, or so-called Eckart streaming [7], is due to the thermo-viscous dissipation of acoustic waves and the resulting pseudo-momentum transfer to the fluid [8, 9]. In microfluidics, acoustic streaming can be used to generate controlled flows in fluids samples.

Acoustic radiation pressure or more exactly acoustic radiation stress (since it is not necessarily normal to the interface) is a time averaged stress exerted by an acoustic wave on an interface between two phases. It was first theoretically predicted by Rayleigh in 1902 and later extended to various configurations (for comprehensive reviews on the subject, see [2, 10, 11]). In particular, Brillouin [12, 13] was the first to unveil the tensorial nature of the radiation stress and Langevin calculated the radiation pressure exerted by an acoustic beam of finite width on a perfectly reflecting obstacle irradiated at normal incidence. It is worth noting that Langevin only "published" the derivation of his expression on the black board of the Collège de France. However, one of his students, Pierre Biquard, published an account of his derivation in Revue d'Acoustique [14], so that Langevin contribution can be documented. In microfluidics, radiation pressure can either be used to deform fluid/fluid interfaces [15–17] or to manipulate particles or cells. Indeed, King in 1934 [18] was the first to study the force exerted by an acoustic wave on incompressible particles suspended in an inviscid fluid. This analysis was further extended by Yosika and Jawasima [19] in 1955 to include the compressibility of the particles and generalized by Gorkov in 1962 [20] for inviscid fluids in the Long Wavelength Regime (that is to say for particles smaller than the Wavelength). Later on, Settnes and Bruus [21] extended this formulation in 2011 to include the effect of the fluid viscosity and Baresch et al. [22] computed the three dimensional acoustic radiation force exerted on an arbitrarily located elastic sphere. For particles, the source of the radiation force is the alteration of the momentum flux due to scattering of the wave by the particle.

To achieve the necessary amplitude for these nonlinear effects to be significant, two main strategies have been developed in the literature : (i) the use of resonant cavities excited with low frequencies (wavelength comparable to the size of the cavity) bulk transducers and (ii) the use

a) Rayleigh SAW

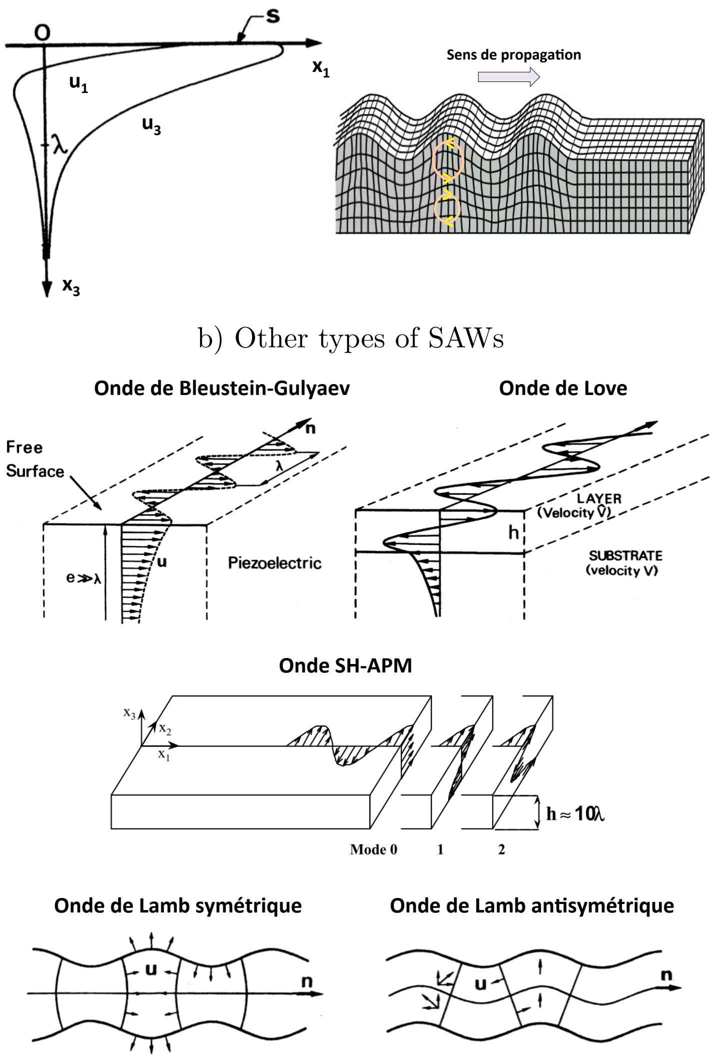

FIGURE 3.2: Schemes representing the different kind of surface acoustic waves.

of higher frequency surface acoustic waves (SAWs). Indeed, in resonant cavities, energy is continuously pumped inside the cavity and the amplitude of the acoustic field inside it is only limited by dissipation mechanisms and leakage out of the cavities. So cavities allow to reach high amplitude acoustic field and thus high nonlinear effects. The second strategy consist in using SAWs to radiate energy inside a fluid sample. Many SAWs can be synthesized (Bleustein-Guliayev, Love, Lamb, Rayleigh,...) (see Fig. 3.2), but to ensure efficient transmission of energy to the liquid, it is necessary to induce deformation normal to the interface. So generally, only Rayleigh and Lamb waves are considered for actuation of fluids. For these waves, the energy remains essentially located at the surface of the substrate (penetration depth inside the substrate is typically one wavelength (see Fig. 3.4)) where the liquid sample is lying, ensuring a good energy transfer to it. The basic difference between Rayleigh and Lamb waves is that in the case of Rayleigh waves the substrate height h is much larger than the wavelength λ while for Lamb waves the substrate height is smaller or of the order of λ. Thus, in this second case, the wave sees both interfaces while in the first case they only see one of the interfaces.

Rayleigh SAW

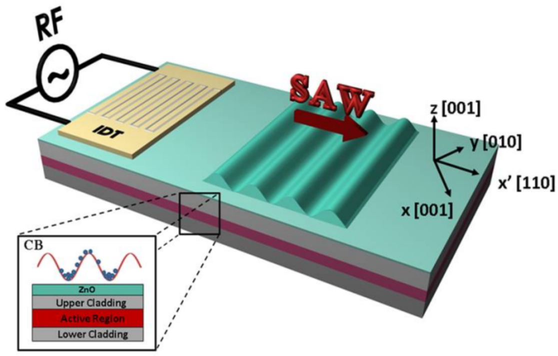

FIGURE 3.3: Schemes representing the synthesis of a Rayleigh type SAW with InterDigitated Transducers (IDTs)

In microfluidics, Rayleigh and Lamb waves are generally synthesized at the surface of a piezoelectric substrates with so called interdigitated transducers (IDTs) (that is to say equally spaced electrode fingers deposited by metal sputtering and photolithography techniques on the substrate (see Fig. 3.3)) by applying sinusoidal voltage to them. A major advantage compared to bulk transducers is that there is no reflected wave (only a refracted one) at the liquid/substrate interface and thus all the energy of the surface wave is transmitted to the liquid within a distance called the leaky-wave attenuation length L_{lw}. This characteristic length is of the order of 4 mm at 20 MHz (see Fig. 3.4)) and decreases quasi-linearly with the frequency. Thus the use of SAWs of typically 10 to 500 MHz allows excellent energy transfer for scales typically used in microfluidics.

Systems based on cavities can be used to generate micro flows in microchannels or for particles sorting [23–26]. On the other hand surface acoustic waves (SAWs) are versatile tools for the actuation of fluids at small scales. In digital microfluidic, they can be used to move [27–29], divide [30], merge [31], atomize [32–36] or mix [37] sessile droplets. In microchannels, they allow fluid pumping [38, 39] and mixing [40, 41] [42]. Finally, in both configurations, they can be used to manipulate and sort particles[43–50] and cells [51–58].

Despite an extensive literature in this field, many challenges lie ahead. First, while many systems are now available for practical purposes, a clear understanding of the underlying physics is still missing for many of them (especially in the field of SAWs where the exciting field can be extremely complex and constantly and nonlinearly interacting with the fluid sample). We will see that a better understanding of the underlying physics can lead to dramatic improvement of the technology. Second, all the operations described above require a specific design of the

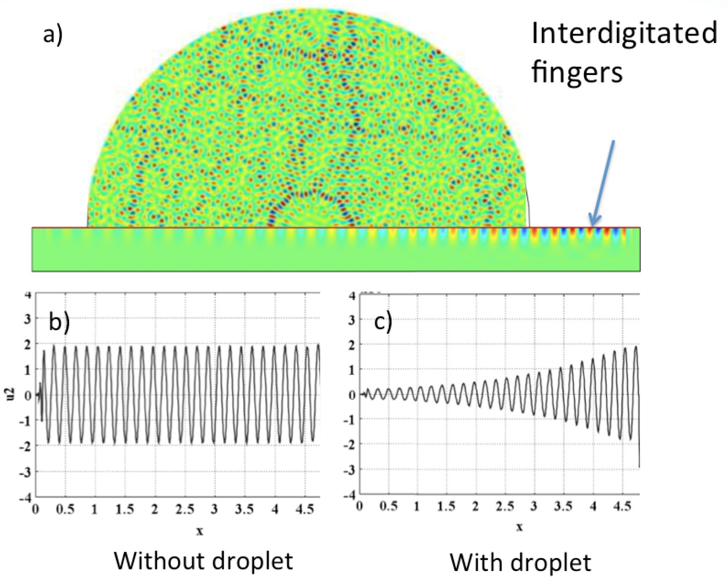

FIGURE 3.4: a) Simulation (Comsol) showing the transmission of an acoustic wave from a Niobate Lithium piezoelectric substrate to a droplet lying on the substrate. The excitation frequency is 20 MHz, the liquid is water and the radius of the drop is 2 mm. The wave is propagating from the right to the left. b) Evolution of the amplitude of the Rayleigh SAW (vertical displacement u_2) at the surface of the substrate when no droplet is lying on it. c) Evolution of the amplitude of the Leaky Rayleigh SAW when a droplet is lying on it (and thus acoustic energy is transmitted from the substrate to the drop).

actuators, thus limiting the range of applications. Third, only the simplest spatio-temporal waveforms (such as plane and focused waves) have been explored so far. With these wavefields, some operations such as precise vorticity control or unique particle or cell 3D manipulation cannot be achieved. Finally, the use of acoustics for biological operations is still at its infancy. In particular no platform allows so far both precise control of biofluids samples and measurement of their biological properties.

The objective of AWESOM ANR project was to tackle these fundamental issues. The physics behind SAW actuators (in particular droplets displacement by SAWs) has been explored experimentally through extensive measurement campaigns but also theoretically and numerically with the development of appropriate models to explain the observed tendencies. This knowledge has been used to adapt the acoustical signal to the droplet physics and achieve drastic reduction of the acoustic power required for their actuation. Then the possibilities offered by advanced wavefields have been explored with a new platform based on arrays of transducers, inverse filter and a programmable electronics that allows the synthesis of any prescribed wavefield compatible with the piezoelectric substrate properties (such as sound speed anisotropy). This platform not only allows to perform all classical operations with a single set of transducers but also to explore the possibilities offered by Bessel beams (also called acoustical vortices) for acoustical tweezing and twisting. Finally, we worked on biological applications (label-free cell sorting) and we are currently working on the design of a platform combining actuators and sensors for both precise control and characterization of biofluid samples.

3.2 Some physics behind droplet actuation with SAWs

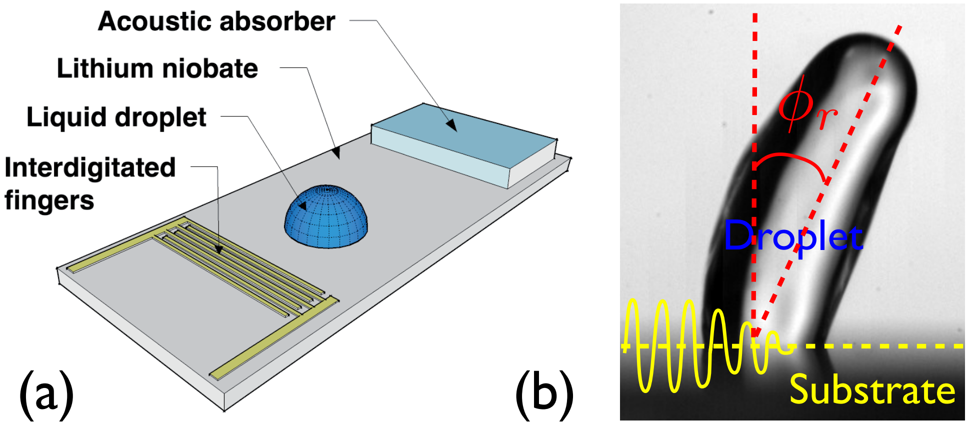

FIGURE 3.5: (a) Sketch of the experimental setup. (b) Drop undergoing large deformation along the acoustic wave refraction angle ϕ_r.

This work has been mainly performed in collaboration with Pr. O. Bou Matar from IEMN laboratory, Dr. P. Brunet from MSC laboratory and a PhD student of our group Dr.Adrien Bussonière. It led to publications : [29, 59, 60]

This section is mainly centered on the physical understanding of droplets dynamics excited by planar propagative SAWs. When a drop is excited by SAWs, it undergoes both oscillatory and translational motions [29, 61] that are strongly coupled to each other [59] (see Fig. 3.6). Droplet displacement by SAWs was first investigated experimentally by Wixforth et al. and Renaudin et al. in 2004 and 2006 [27, 28]. But at this time the coupling between droplet oscillations and translation had not been observed since it requires high speed imaging to visualize it.

The typical system investigated in this section is depicted on Fig. 3.5 : Rayleigh SAWs are generated at the surface of a 1.05 mm thick piezoelectric substrate (X-cut Niobate Lithium $LiNbO_3$) by a transducer consisting of interdigitated fingers [1] excited by a function generator and an amplifier at a frequency around 20 MHz. A liquid droplet of typically 1 to 30 μl (corresponding to a drop radius of 1 to 2 mm) is then placed on the substrate along with an acoustic absorber (some PDMS) on the edge of the substrate to avoid reflection by the boundaries and maintain a propagating wave. The substrate has been treated with an OTS Self Assembled Monolayer to reach a contact angle of about 90^o. Then the droplet dynamics is recorded with a high speed camera mounted on a microscope.

From the standpoint of physical analysis, this is a particularly difficult problem. One reason is that the nonlinear coupling between the acoustic wave and the liquid response involves time

1. Interdigitated fingers are designed with the following process : 1) A titanium (Ti) layer of 20 nm and a gold (Au) layer of 200 nm are successively sputtered on a $LiNbO_3$ substrate 2) The substrate is coated with AZnlof2020 resist, which is patterned by conventional photolithography technique 3) The Au/Ti layers are successively wet-etched by potassium iodide (KI) and hydrofluoric acid (HF 50%), and 4) AZnlof2020 is removed by acetone.

and length scales that differ by several orders of magnitudes, along with nonlinear effects, which render the analysis and simulation of these behaviors extremely difficult. Nonlinearities are involved both at the excitation level (acoustic radiation pressure and acoustic streaming) and at the droplet response one (nonlinear oscillations). In references [29, 59, 60], we have explored the complexity of both the excitation and response. This knowledge helped us to adapt the acoustic field to the specificity of the drop dynamics and considerably optimize droplet displacement. We are now willing to unveil the complex underlying coupling between the acoustic field and the drop oscillation.

3.2.1 Analysis of the drop nonlinear response

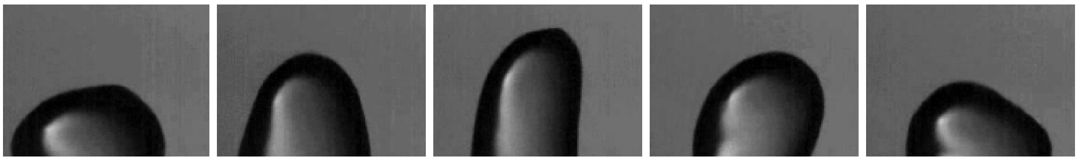

FIGURE 3.6: Oscillatory and translational dynamics of a drop of water of 6 μl excited by SAWs of frequency 20 MHz. Time elapsed between two successive images is 2 ms.

When drops are excited by SAWs, they undergo both translational and oscillatory motions that are strongly coupled to each other (see Fig. 3.6).

Drop oscillations : experimental characterization

To identify the nature of the drop quadripolar oscillations (see Fig. 3.6), we studied the evolution of the drop oscillation frequency f_r as a function of the drop volume $\mathcal{V}$ (see Fig. 3.7). We found a dependency in $f_r \propto \mathcal{V}^{-1/2}$ which is characteristic of inertio-capillary Rayleigh-Lamb modes of drop vibrations [62, 63]. This power law dependance can be recovered from simple dimensional analysis. Let's consider a droplet of liquid with a density ρ and radius R_o surrounded by a gas. When the drop is deformed, capillary effects tend to bring back the drop to its spherical form and thus constitute the spring of this spring-mass system. The mass is simply the inertia of the moving liquid. The order of magnitude of inertial effects can be estimated from the term $\rho \frac{\partial \vec{v}}{\partial t}$ in Navier-Stokes equations :

$$f_i \sim \rho \frac{\partial \vec{v}}{\partial t} \sim \rho R_o f_{RL}^2$$

This term is homogeneous to a force per volume unit. Then capillary effects can be estimated from Laplace formula. Since Laplace pressure jump is equal to $2\sigma/R_o$, the associated force per unit volume is :

$$f_s \sim \sigma / R_o^2$$

with σ the surface tension. Then $f_s \approx f_i$ gives

$$f_{RL} \propto \sqrt{\frac{\sigma}{\rho R_o^3}} = \sqrt{\frac{\sigma}{\rho}}\mathcal{V}^{-1/2}$$

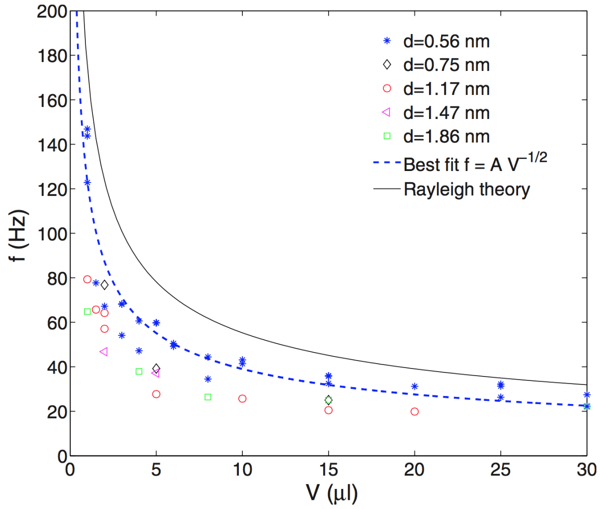

FIGURE 3.7: Evolution of the drop oscillation frequency as a function of the drop volume for different amplitudes of the acoustic wave quantified by the measurement of the amplitude of the normal displacement to the surface d with a laser interferometer.

Rigorous calculation allows the determination of the missing coefficient, which depends on the order n of the mode considered :

$$\omega_{RL} = \sqrt{(n+2)n(n-1)\frac{\sigma}{\rho R_o^3}}$$

with ω_{RL} the angular Rayleigh-Lamb frequency.

It was performed by Rayleigh in 1879 [62] from energy considerations, Lagrange method and spherical harmonics decomposition. Then, it was extended by Lamb in 1932 [63] for a droplet of density (ρ) surrounded by a fluid of density (ρ') :

$$\omega_{RL} = \left[(n+2)(n+1)n(n-1)\frac{\sigma}{[(n+1)\rho + n\rho']\, R_o^3}\right]^{1/2} \tag{3.1}$$

The effect of the fluids viscosity has been introduced later on by Miller and Scriven (1968) [64] and Prosperetti (1980) [65]. Then, larger (nonlinear) vibrations have been considered by Foote (1971) [66], Tsamopoulos and Brown (1983) [67], and more recently by Smith [68]. An interesting result is that when droplet oscillations become larger, the characteristic frequency ω_{RL} decreases due to nonlinear effects. This effect is indeed observed on Fig. 3.7 : as the amplitude of excitation d increases, the drops undergoes larger droplet oscillations and a decrease of Rayleigh-Lamb frequency is observed. Finally, while these models have been developed for levitating drops, they can also be adapted to sessile drops. In this case, the droplet vibration is affected by the contact angle [69] and the pinning of the contact line [70].

A still unsolved issue in the case of droplets excited by SAWs is the origin of these drops quadripolar oscillations. Indeed, the vibrations appear naturally, although the forcing frequency is of the order of 20 MHz, far above Rayleigh-Lamb frequencies (typically 100 Hz). An interesting observation is that the cleaner the substrate is (and thus the smaller the hysteresis is) the less the drop oscillates (or maybe since we do not have an infinite substrate, the more time it takes for the instability to develop). So there might be a link between the triggering of these oscillations and the hysteresis. Indeed energy efficiency considerations might show that stick-slip oscillatory locomotion is more energetically effective than slip motion [71]. We are also exploring a coupling between the drop shape and the radiation pressure in analogy with optomechanical resonators or gravity waves detectors (see Issenmann et al. [72]) to explain the origin of these oscillations.

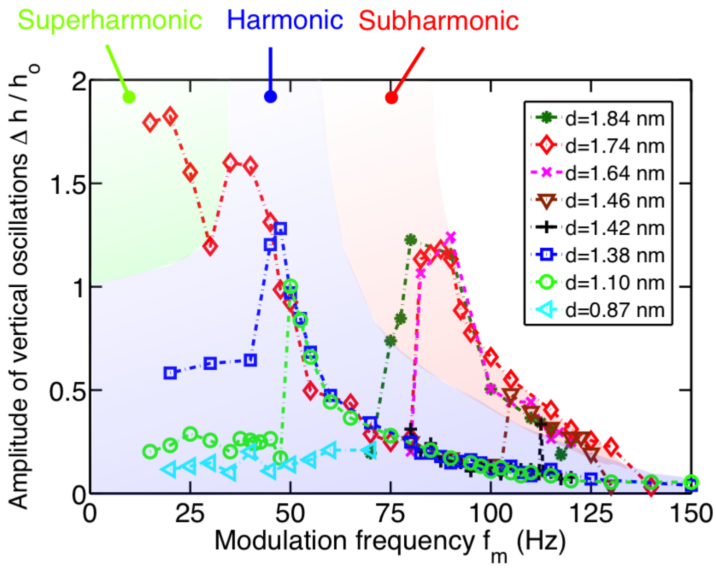

FIGURE 3.8: Amplitude of vertical oscillations of the drop Δh divided by the initial height of the droplet h_o as a function of the modulation frequency f_m for different amplitudes d of the surface acoustic wave. In the green, blue and red regions, the droplet response is respectively superharmonic, harmonic and subharmonic (compared to the frequency of modulation).

Before delving into this fundamental subject, we wanted to characterize further the oscillation of the drop and its link with the translational motion. So instead of looking at naturally appearing drop oscillations, we forced these oscillations by modulating the acoustic signal at a frequency f_m around the drop Rayleigh-Lamb frequency. Results are summarized on Fig. 3.8, which shows the drop amplitude of oscillation Δh (divided by the initial height h_o) as a function of the modulation frequency f_m for different amplitudes of the acoustical signal d. Three regions are observed on this graph depending on the drop response frequency f_r compared to the modulation frequency f_m :

Harmonic region ($f_r = f_m$) : shift of resonance. In the blue area of Fig. 3.8, a peak of response is obtained when f_m reaches the inertio-capillary characteristic frequency f_o, which can be estimated from Rayleigh formula : $f_o = (8\sigma/3\pi\rho V)^{1/2} \approx 89$ Hz for the dipolar ($l = 2$) oscillation of a $7.5\mu l$ droplet, with σ the surface tension and V the droplet volume. At intermediate power (d=1.10 nm, d=1.38 nm), the peak is asymmetric, with a skewness directed to low frequencies and the resonance frequency decreases with the amplitude of oscillation. This response is typical of an *anharmonic* oscillator with softening spring ($\beta < 0$) :

$$\ddot{x} + 2\lambda\dot{x} + \omega_o^2 x + \alpha x^2 + \beta x^3 = F cos(\Omega t) \tag{3.2}$$

where x is the dynamic variable (here the deformation of the drop), t the time, λ the damping coefficient, $\omega_o = 2\pi f_o$ the angular eigen frequency, α and β two nonlinearity coefficients, F the amplitude of excitation and Ω the excitation frequency. Such nonlinear behavior has already been reported by Perez et al. [73] for levitating drops larger than the capillary length and more recently by Miyamoto et al. [74] for sessile droplets smaller than the capillary length, with pinned contact line. These authors determine the coefficient appearing in Eq. (3.2) from experiments and compare successfully the frequency response of the drop to theoretical predictions. In our system the oscillation damping is due to dissipation in the viscous boundary layer and in the neighborhood of the contact line [75]. The nonlinear response of droplets appears when they undergo finite-amplitude deformations [67, 68], leading to a shift of the resonance frequency to lower frequencies as the amplitude of oscillation increases. For sessile drop, additional nonlinearity results from the up-down asymmetry of boundaries and the presence of a contact line.

Superharmonic region : combination of modes. In the green region of Fig. 3.8, low f_m and large Δh, the drop response is a combination of harmonic and superharmonic modes. Indeed, the drop is pushed by the acoustic wave when the signal is on. Then, the drop keeps bouncing in the period with no forcing (signal is off) and oscillates a whole cycle before the next push. After a transient phase, this synchronization of forced and natural bouncing results in large drop oscillations.

Subharmonic region ($f_r = f_m/2$) : parametric resonance. In the red region of Fig. 3.8, the droplet responds at $f_m/2$. This subharmonic response appears only above a threshold : $d \geq 1.42$ nm, with a frequency window broadening progressively with the amplitude of oscillation Δh. This is typical of a so-called *Arnold Tongue*. Furthermore, the amplitude of the subharmonic response at fixed f_m is independent of the amplitude of excitation d. All these properties are characteristic of parametric resonance. Parametric instability of an oscillator is enabled when its characteristic frequency ω_o is modulated in time near $2\omega_o$ [76]. It can be modeled with a Mathieu equation :

$$\ddot{x} + 2\lambda\dot{x} + \omega_o^2[1 + A\cos(2\omega_o + \epsilon)t]x \tag{3.3}$$

with $\epsilon \ll \omega_o$. Such Mathieu equation can be obtained when an anharmonic oscillator described by Eq. (3.2) is excited near $2\omega_o$: $\Omega = 2\omega_o + \epsilon$ [77]. Indeed, from the asymptotic expansion of the variable x in Eq. (3.2) : $x = x_1 + x_2$, with x_1 the solution of the harmonic oscillator and $x_2 \ll x_1$, we obtain at second order :

$$\ddot{x_2} + 2\lambda \dot{x_2} + \omega_o^2 \left[1 - \frac{2\alpha F}{3w_o^4}\cos(2\omega_o + \epsilon)t + ...\right] = 0 \tag{3.4}$$

Drop oscillations : theoretical analysis

The considerations developed in the previous section to interpret the frequency spectrum are only phenomenological. To obtain a quantitative theoretical description of the phenomenon, the oscillator equation of the quadripolar mode is required. With Adrien Bussonière, we calculated this equation for a spherical, levitating drop using weakly nonlinear perturbation approach, Lagrangian formalism and spherical harmonics decomposition. After "a few" pages of calculation, the following formula was obtained :

$$\ddot{x}_2 + 2\lambda_2\ \dot{x}_2 + \omega_2^2\ x_2 + t_2\ x_2\ddot{x}_2 + c_2\ \dot{x}_2^2 + s_2\ x_2^2 = 0. \tag{3.5}$$

In this expression, x_2 is the projection of the interface perturbation on the second spherical harmonic, ω_2 and λ_2 the dimensionless frequency and dissipation coefficient of mode 2, given by the general formula for mode n :

$$\omega_n^2 = n(n+2)(n-1) \qquad \lambda_n = Ca(n-1)(2n+1)$$

with $Ca = \mu R_o f/\sigma$ the capillary number which compares viscous and capillary stress and $t_2 = \frac{9\sqrt{5}}{14\sqrt{\pi}}$, $c_2 = \frac{4\sqrt{5}}{7\sqrt{\pi}}$ and $s_2 = \frac{4\sqrt{5}}{7\sqrt{\pi}}$ three coefficients of nonlinearity resulting from nonlinearities of Navier-Stokes equation and nonlinearities in the interfacial deformation.

This equation would allow to study the free response of the drop. However, the study of the forced response requires the integration of the forcing term in the equation, which is not straightforward since the forcing itself depends on the shape of the drop. We are currently working on the integration of various forcing conditions (magnetic, acoustic levitation, ...) and on the stability analysis of parametric response using Floquet theory. Experimental databases exist in the case of magnetic forcing and acoustic levitation and numerical simulations are performed with Gerris flow software for comparison with our model.

Then, the next step will be to adapt this equation for sessile drops by following the method developed by Strani and Sabetta [69]. Dissipation at the contact line must also be accounted for to obtain a realistic model, that could be quantitatively compared with our experiments.

Drop translational motion and link with its oscillations : experiments

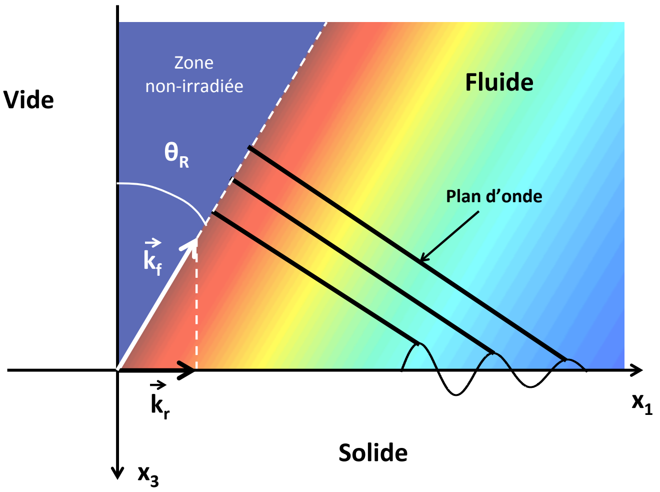

FIGURE 3.9: Scheme of a leaky Rayleigh wave propagating in a solid substrate and radiated inside an infinite liquid medium

The translational motion of the drop is induced by the asymmetry of the acoustic field radiated inside the drop. Indeed, the transmission of the acoustic wave from the substrate to the drop follows Snell-Descartes law. Since the SAW incidence angle is equal to $\pi/2$, the wave is radiated inside the liquid according to the Rayleigh angle θ_R defined by $\sin\theta_R = c_f/c_R$ where c_f is the sound speed in the fluid and c_R the speed of the Rayleigh SAW in the substrate (see Fig. 3.9).

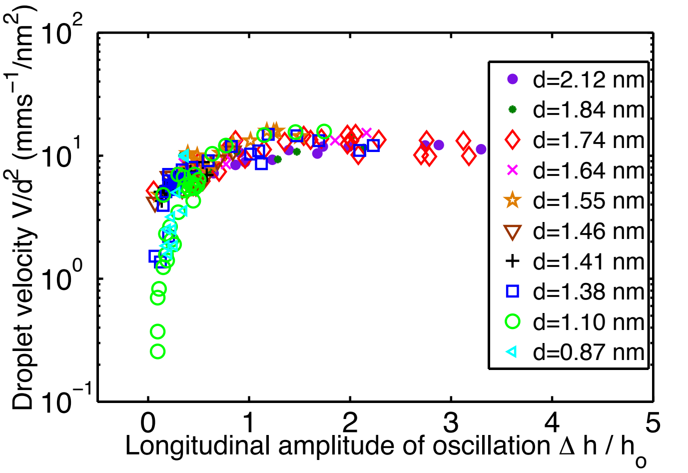

FIGURE 3.10: Velocity of the drop divided by the square of the surface acoustic wave amplitude d^2 (corresponding to the acoustic power radiated into the drop up to a prefactor) as a function of the longitudinal amplitude of oscillation $\Delta h/h_o$. Each marker corresponds to a specific amplitude d.

As a consequence the resulting acoustic streaming and radiation pressure will deform the drop asymmetrically provoking its motion on the substrate due to the difference between the advancing and receding contact angles. So the asymmetry of the impinging wavefield is the driving mechanism of the drop translation. Nevertheless, we evidenced experimentally [59] that there is a strong correlation between the drop amplitude of oscillation and its translational velocity (see Fig. 3.10). This figure shows the drop velocity (divided by the acoustic power) as a function of the longitudinal amplitude of oscillation for all the experiments previously shown on Fig. 3.8, that is to say for different frequencies of modulation, different drop responses (superharmonic, harmonic and subharmonic) and different amplitudes of the acoustic wave d. The excellent collapse of the data shows that the velocity of the drop is mainly determined by the drop amplitude of oscillation, underlying the strong correlation between drop translational and oscillatory motions. Moreover, we can see on this figure that high amplitudes of oscillations are not required to achieve good droplet locomotion. Indeed, while low amplitude oscillations (up to 30% of the initial drop height) drastically improve the drop displacement, saturation of the curve shows that larger amplitude does not result in improved mobility.

Drop translational motion and link with its oscillations : analysis

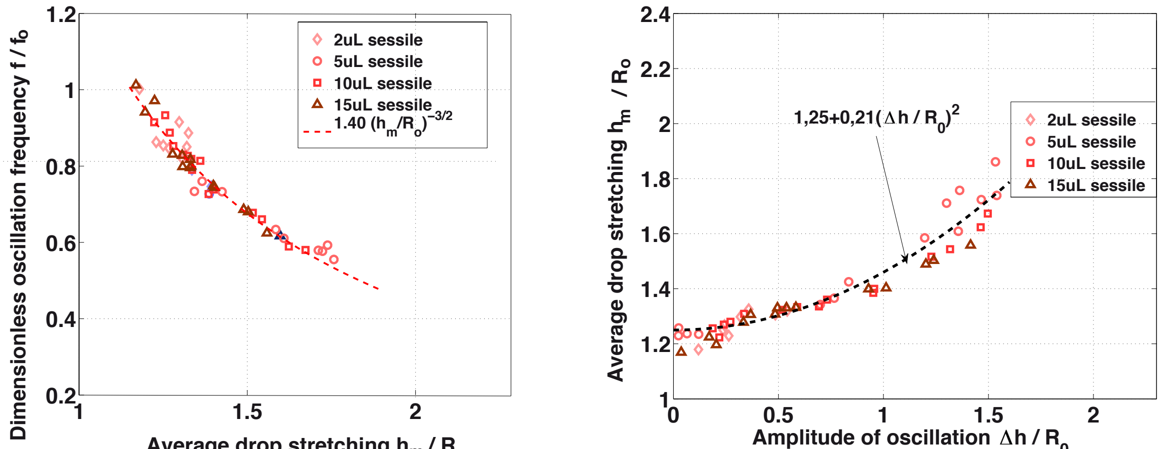

FIGURE 3.11: a. Evolution of the drop oscillation frequency f divided by the corresponding Rayleigh-Lamb frequency $f_o = 1/2\pi\sqrt{8\sigma/\rho R_o^3}$ as a function of the average drop stretching h_m divided by the drop initial radius R_o. b. Evolution of the average drop stretching h_m as a function of the drop amplitude of oscillation Δh..

To further analyze the origin of this peculiar behavior, we performed many experiments where we measured the evolution of the drop oscillation frequency, its translational velocity and the mobility of the contact lines for different drop volumes and input acoustic power [60]. Analysis of the data shows that :

1. The drop response frequency f_r (obtained without modulation of the acoustical signal) solely depends on the average drop stretching $h_m = 1/T \int_t^{t+T} h(t)dt$ (with $h(t)$ the drop height), that itself depends on the drop amplitude of oscillation Δh (see Fig. 3.11). To understand it, let's consider a spring-mass system. If the spring stiffness is constant (linear system), the oscillation frequency does not depend on the mean stretching of the system.

But for a nonlinear system, average stretching of the spring result in a modification of the eigenfrequency explaining the first relation. Then, if the system has quadratic nonlinearities, due to the trigonometric identity $\cos^2(\omega t) = (1 + \cos(2\omega t))/2$, quadratic terms will generate both a static deformation (frequency $\omega = 0$) and oscillations at twice the driving frequency (2ω). Since in this case the static deformation is the result of interactions between oscillatory terms, it can be shown that it is proportional to the square of the amplitude of oscillation. This is indeed observed on Fig. 3.11 b. where $h_m \propto \Delta h^2$. As we have shown (equation 3.5) that drops can be modeled as oscillators with quadratic nonlinearities, such behaviors are indeed expected.

2. The mobility of the contact line per oscillation cycle also depends quasi linearly on the amplitude of the drop stretching [60].

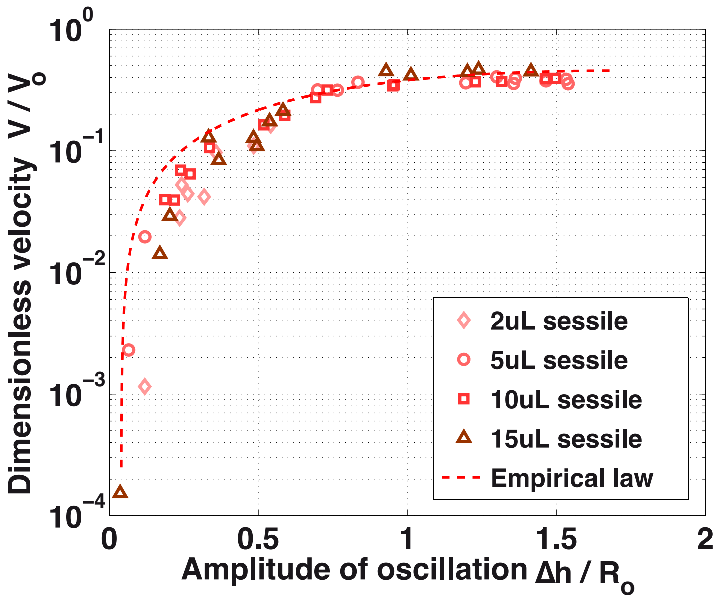

FIGURE 3.12: Translational drop velocity V divided by the characteristic velocity of drops oscillations $V_o = f_o R_o$ as a function of the amplitude of oscillation Δh divided by the drop radius R_o. The dashed curve correspond to equation 3.6.

All these considerations are detailed in reference [60]. Since the drop translational velocity is the product of the drop frequency oscillation times the mobility of the contact line per cycle, the combination of these relations results in a semi-empirical formula that allows to predict the evolution of the drop velocity as a function of its amplitude of oscillations :

$$\frac{V}{V_o} = C_1 \left[\frac{\Delta h}{R_o} + C_2\right] \times \left[1 + C_3 \left(\frac{\Delta h}{R_o}\right)^2\right]^{-3/2} \tag{3.6}$$

with V the translational velocity of the drop, $V_o = f_o R_o$ the characteristic velocity associated with drops oscillations and C_1, C_2 and C_3 three constants whose value is determined experimentally. With this equation, we recover qualitatively the behavior observed experimentally for different drop sizes and acoustical power (see Fig. 3.12) and we can now explain the observed tendency. In particular we can infer from this result that the saturation of the velocity as a function of the amplitude of oscillation described previously relies on the decrease of the oscillation frequency as a function of the average drop stretching induced by quadratic nonlinearities.

3.2.2 On the complexity of the acoustic field in the drop.

Drops are very peculiar acoustical resonators, especially when they are excited by SAWs :

- First drops are cavities with high quality factors : once the acoustic energy is radiated inside the drop, most of it reminds inside it. Indeed, the liquid-air drop interface is almost a perfectly reflecting interface (due to the large impedance contrast between the two phases). Moreover, while the transfer of energy from the substrate to the drop is very efficient, the acoustical wavefield inside the liquid can only recreate a Rayleigh SAW if it impacts the surface with Rayleigh angle. But due to the spherical drop shape, only a slight portion of the acoustic wavefield is reflected with this angle. If the wave in the liquid impacts the substrate with another angle, it can nevertheless be transmitted into a longitudinal bulk wave, but, in this case, the transmission coefficient relies on the impedance contrast between the liquid and the substrate.
- Then, since the surface of the drop is perfectly reflecting and spherical, it simply acts as a spherical mirror. So if a beam is transmitted to the drop with a given angle (in this case the Rayleigh angle), focalization will occur at half the height of the drop (for a droplet with contact angle $\pi/2$).
- Finally, and most interestingly, the field inside the drop can be extremely complex and even chaotic depending on the drop size, the excitation frequency and the attenuation length. From the standpoint of wave physics, a chaotic cavity is a cavity for which slight changes in the shape of the cavity or in the properties of the impinging wave result in completely different stationary wavefield patterns.

The first condition to obtain such chaotic behavior is that the wavefield in the drop is a stationary wavefield resulting from multiple reflection at the cavity boundaries. So the acoustic wave attenuation length in the liquid must be much larger that the characteristic size of the cavity. The viscous attenuation length is defined in a liquid by the formula :

$$L_{att} = \frac{2\rho c^3}{(\frac{4}{3}\mu + \mu^b)\omega_{ac}^2}$$

with ρ, c , μ and μ^b the density, sound speed, shear and bulk viscosity respectively and ω_{ac} the acoustic frequency. Fig. 3.13 shows the number of reflection inside the drop according to its size

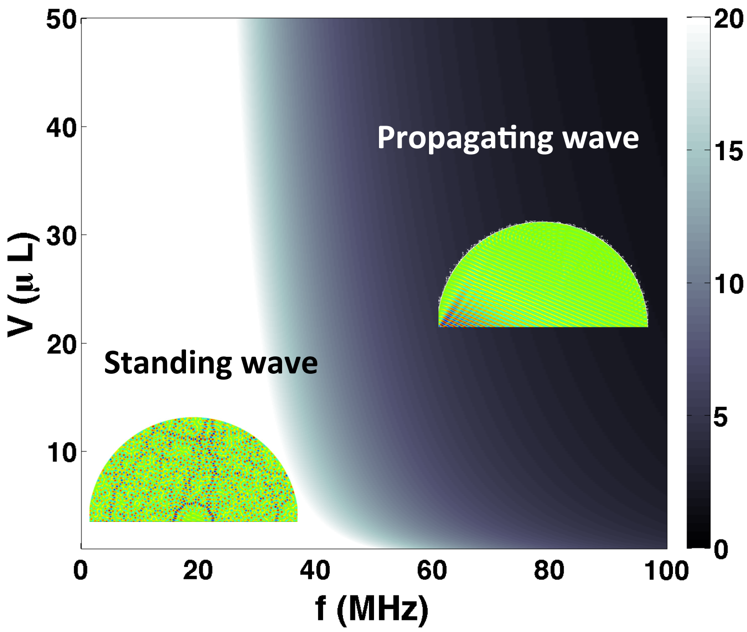

a.

FIGURE 3.13: Number of wave reflections in the cavity according to the acoustic frequency and the drop size.

and the excitation frequency. At 20 MHz, for a droplet of a few micrometers, the standing wave is always observed.

The second condition is that the resonance peaks of the cavity modes overlap one another. A drop is an acoustic cavity with eigenmodes associated with a eigenfrequency (see Fig. 3.14). If dissipation in the cavity is neglected, the modes resonance peaks are Dirac functions at well defined frequencies and the modes are orthogonal. However, due to dissipation, the resonance peaks have a finite width. As a consequence, when the frequency increases, peaks become closer, and finally overlap one another. When it occurs, different modes can coexist at the same excitation frequency leading to chaotic behavior A criterion was proposed by Schröder [78] to define the transition to a chaotic cavity. This criterion (see Fig. 3.15) shows that our experiments are indeed performed in the chaotic regime.

One might think that, in this case, the resulting streaming patterns and interface deformation will be extremely complicated to handle. In fact, we expect and observe the exact opposite behavior. Indeed, since the droplet shape is continuously modified, the acoustic field inside the drop evolves constantly and the drop will only be sensitive to the average of the chaotic acoustic fields over all configurations. We have shown in reference [29] that when such averaging is performed, chaotic fluctuations disappear and only the impinging field remains, explaining why experimentally we indeed observe asymmetric deformation of the drop.

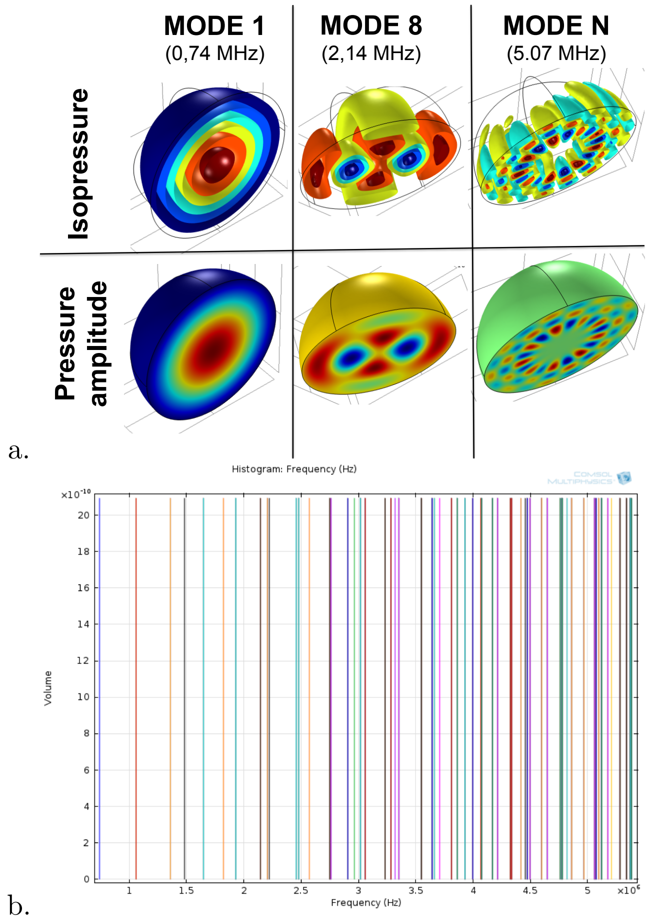

FIGURE 3.14: a. Illustration of three acoustic eigenmodes of a drop of 1mm diameter with contact angle $\pi/2$. b. Spectral density of the modes (each peak correspond to an eigenmode).

We are now working on some statistical methods to determine properly the acoustic radiation pressure and streaming that would result from chaotic wavefields.

3.2.3 Adaptation of the acoustic signal to the specificity of the drop response

We have shown in this section (i) that droplet inertio-capillary oscillation modes can be excited either directly or parametrically by modulating the acoustic signal at appropriate frequencies and (ii) that droplet oscillations considerably facilitate the drop translation at a given acoustic power. Thus, adaptation of the acoustic signal to the specificity of the drop physics can lead to dramatic decrease in the required acoustic power for droplet actuation (see accompanying movie). This is of primary interest for the manipulation of biofluid samples, where heating resulting from the use of excessive acoustic power can be detrimental to the biological content. This principle is illustrated in subsection 3.4.

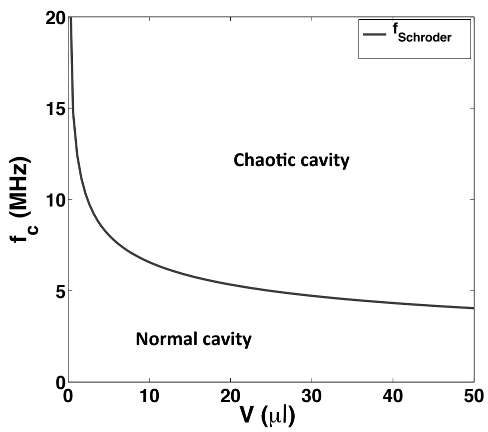

FIGURE 3.15: Schröder criterion showing for which frequencies f_c and droplet volume V a half sphere is a chaotic cavity.

3.3 Advanced wavefields synthesis : toward vorticity control and 3D single particle manipulation

The work of this section has been mainly performed in collaboration with Pr. O. Bou Matar from IEMN Laboratory, Dr. J.L. Thomas from INSP laboratory and a PhD student from our group Antoine Riaud. It has led to publications : [79–81].

In this section, we explore the possibilities offered by multi-arrays of transducers and inverse filter technique (i) to design a versatile platform that is able to perform all the operations already demonstrated in the literature with a single design and (ii) to explore possibilities offered by new wavefields such as "swirling surface acoustic waves" to perform operations that cannot be achieved with plane or focalized waves.

3.3.1 Multi-arrays of transducers and inverse filter for advanced wavefields synthesis

a) b)

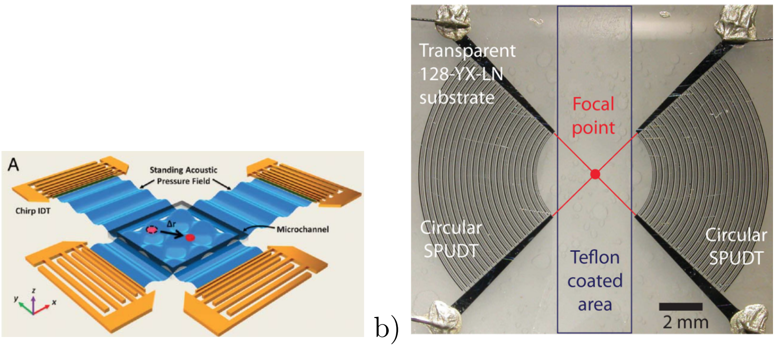

FIGURE 3.16: Different IDTs designs used in the literature. a) Design with four IDTs for the displacement of particles in micro channels. b) Design with two focused IDTs for droplets jetting.

In the literature, Rayleigh waves are always synthesized at the surface of piezoelectric substrates by a single or the combination of at most four plane or focalized IDT(s) (see Fig. 3.5 and 3.16). With these designs, only the possibilities offered by "plane" of "focalized" waves can be explored and each system is specific to a given task (droplet actuation, jetting, mixing, particles displacement, ...). Moreover, it is worth noting that the focalized designs used in the literature do not consider the anisotropy of the piezoelectric materials. The fingers are arranged into concentric circles (see Fig. 3.16) with a constant distance between them while the speed of sound (and thus the wavelength at fixed frequency) differs according to the crystallographic direction. Thus, these designs do not actually synthesize focalized waves.

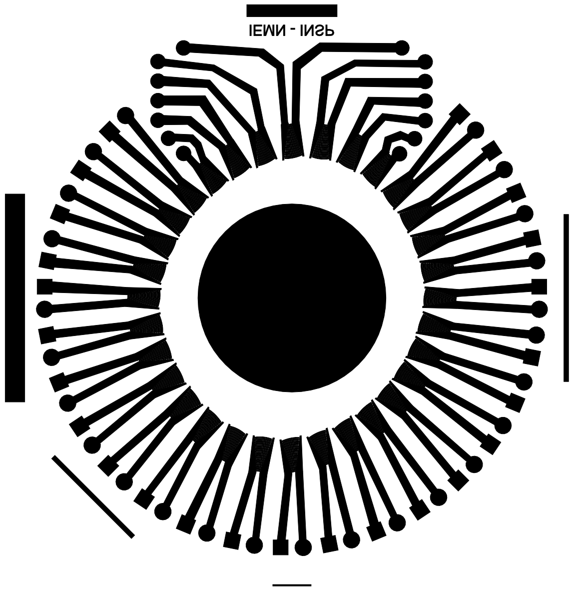

FIGURE 3.17: Array of 32 IDTs developed at IEMN for inverse filter. The black area at the center is the acoustic scene. Each transducer wavelength is adapted to the sound speed in the corresponding direction. Diffraction is optimized so that the acoustic beam emitted by each transducer covers the acoustic scene. Finally, the transducers are positioned on the slowness curve.

To overcome all these shortcomings, we developed an array of 32 unidirectional IDTs (see Fig. 3.17) with operating frequency 12 MHz, whose wavelength is adapted to each crystallographic direction and which are disposed radially around a target spot (called the "acoustic scene") on the so-called "slowness curve" (which simply corresponds to a curve with equal propagation time from the center in all directions). In order to widen the range of possible acoustic fields, every spot on the scene should be illuminated by all transducers. It is achieved by using IDTs with narrow apertures and disposing them remotely from the acoustic scene to promote diffraction. Then, each of these transducers is independently controlled with a programmable electronics. With this device and *inverse filter technique*, any prescribed wavefield compatible with the property of the substrate (such as its anisotropy) can be synthesized, e.g. plane, real focalized waves and even acoustical vortices (that we will discuss in the next section).

Inverse filter [82] is a very general technique for synthesizing complex signals that propagate through arbitrary linear media. Given a set of independent programmable sources, it finds the optimal input signal to obtain the target wavefield. This process can be decomposed into three distinct stages. First, the signal emitted by each transducer (impulse response) is measured in the acoustics scene. In practice this response is recorded in a number of control points whose distance cannot exceed $\lambda/2$ according to Shannon principle. This allows to define in the Fourier space, a transfer matrix $H_{ij}(\omega)$ (called the propagation operator) between the Fourier transform of the entrance signal emitted by transducer j, $E_j(\omega)$, and the response signal at control point

i, S_i : $S_i = H_{ij}E_j$ (with Einstein notation). For SAWs, the vibrations of the substrate at control point i (typically of the order of a few nanometers) is measured by a home made polarized Michelson interferometer whose principle is given in reference [80]. Then the targeted output signal S is defined and the transfer matrix H is inverted to compute the optimal input signal $E = H^{-1}S$. Finally the optimal signal is synthesized by each transducer. If $e_j(t)$, $s_i(t)$ and $h_{ij}(t)$ are the inverse Fourier transform of $E(\omega)$, $S(\omega)$ and $H(\omega)$, it is worth noting that the output time signal $s(t)$ is the convolution product of $h_{ij}(t)$ and $e_j(t)$:

$$s_i(t) = h_{ij}(t) * e_j(t)$$

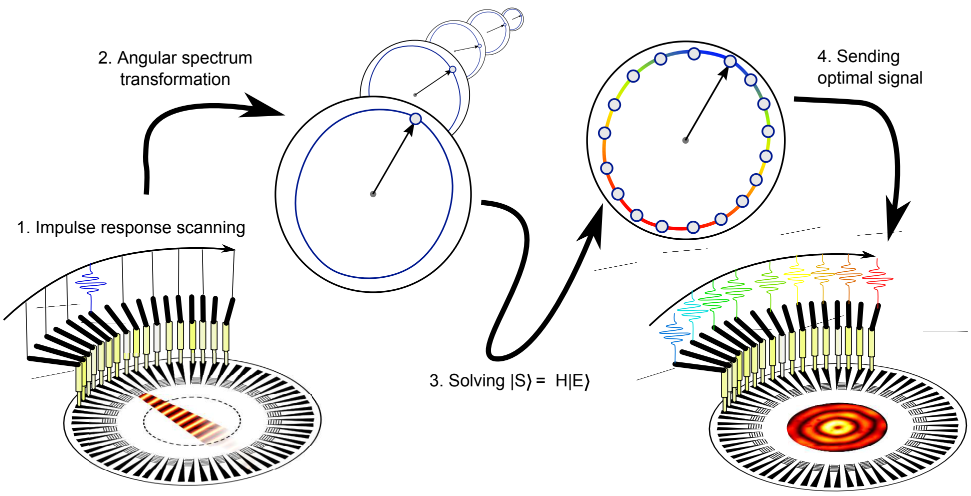

FIGURE 3.18: Inverse filter flowchart. Inverse filter happens in four steps : (1) recording of the spatial impulse response (H matrix) for all transducers. (2) Transformation of the H matrix from spatial to spectral domain, where the response is sharper. (3) Computation of the optimal input E for a desired output S by pseudo-inversion of the matrix H. (4) Generation of the signal from optimal input E.

In practice complicated, things are a bit more complicated. Indeed, the propagation operator is generally ill-conditioned since small errors in the measurements produce very large errors in the reconstructed results. Then the number of control points is not necessarily the same as the number of sources (transducers) and thus the propagation operator is not necessarily a square matrix. So the pseudo-inverse of the propagation operator is obtained through singular value decomposition. Finally, inverse filter technique had been initially developed to generate acoustical wavefields in 3D media. In this case, the target field is a surface and has a smaller dimensionality (2D) than the propagative medium (3D), whereas for SAWs the target field has the same dimensionality as the propagative medium (both 2D). So the control points are not independent and the wavefield must fulfill the dispersion relation. This requires some refinements in the method (see Fig. 3.18 and reference [80]).

3.3.2 Acoustical vortices : synthesis with swirling SAWs

Bessel beams (also called acoustical vortices in the field of acoustics) are helicoidal waves that spiral around a phase singularity (see Fig. 3.19) where their amplitude cancels resulting in concentric rings around a dark core [83, 84]. These beams are the separate variables solutions of Helmholtz equation in cylindrical coordinates (such as spherical harmonics for Helmoltz equation in spherical coordinates) and are defined by the following mathematical expression (for the pressure perturbation field p) :

$$p(r, \theta, z, t) \quad = \quad P J_l(Kr) \sin(l\theta + k_z z - \omega t) \tag{3.7}$$

with P, l, r, θ, K, k_z, ω, t and J_l respectively the amplitude of the acoustical wave, the topological charge of the Bessel beam, the radial and angular coordinates, the transverse and axial component of the wave vector, the wave angular frequency, the time and the cylindrical Bessel function of order l. Naturally, the transverse and axial components of the wave vector verify the dispersion relation of a Bessel beam : $K^2 + k_z^2 = \omega^2/c^2$, with c the sound speed. It is also important to note that, similarly to plane waves, Bessel beams are of infinite radial extent, so only truncated approximation of acoustical vortices can be synthesized in practice.

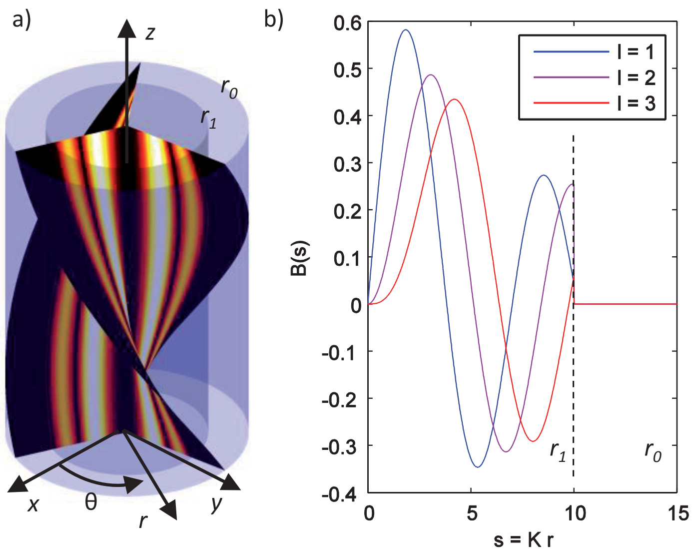

FIGURE 3.19: a. Truncated acoustical vortex with topological charge and $Kr_1 = 10$ (z-axis was dilated 10 times). Surfaces correspond to the phase $l\theta + k_z z = \pi/2$ while colors indicate the magnitude of the radial function $AJ_l(Kr)$. b. Corresponding radial function $AJ_l(Kr)$ for $l = 1$ to 3.

Acoustical vortices are of much practical interest. First, they can propagate without diffraction inside cylindrical waveguides, since they are the solutions of Helmholtz equations in cylindrical coordinates. Then the core singularity can be used to trap objects with acoustic radiation pressure. It is the cornerstone of acoustic and optical tweezers [85–90]. Furthermore, the twisting wavefront transports orbital angular momentum, which can be transmitted to absorbing media and exert a torque. This torque can be used to rotate objects [83, 91, 92] or generate controlled vortical flows [79]. Finally, these waves can also be useful for in-depth microscopy since they can self-reconstruct after being damaged by obstacles on the propagation axis [93, 94].

In previous literature [86, 92, 95, 96], acoustical vortices had only been synthesized with individual piezo-ceramic elements. Such macroscopic transducers cannot be implemented for lab-on-a-chip applications. IDTs on the other hand have the major advantage of simple integration (piezoelectric thin films such as PZT or AlN can even be deposited on non-piezoelectric substrates [97]), easily possible miniaturization and low cost fabrication with soft lithography techniques [98]. It has even been shown recently that IDTs can be integrated on flexible substrates [98, 99].

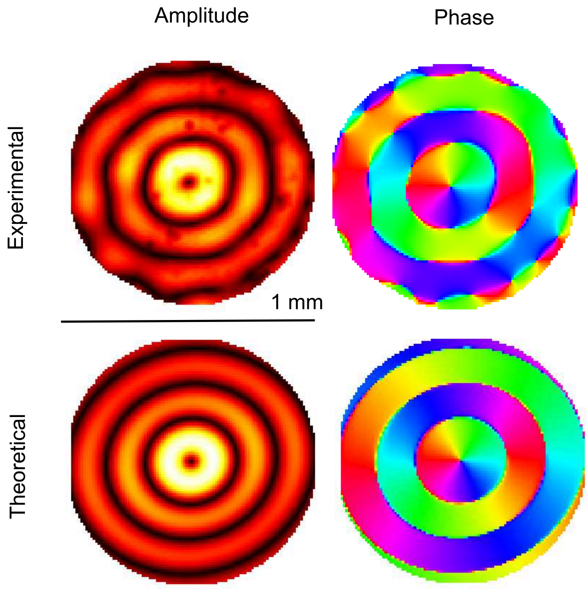

FIGURE 3.20: Experimental and theoretically predicted first order anisotropic swirling SAW ($\mathcal{W}_1^0$) wave phase and amplitude. Experimentally, the vibration of the substrate is measured with a laser interferometer. Maximum experimental displacement is 36 nm.

To synthesize acoustical vortices with surface acoustic waves, we developed the array of transducers described in the previous section and adapted the inverse filter technique for SAWs. In principle, acoustical vortices could be synthesized inside a fluid sample by a wave that we name "swirling SAW" [80] and that is simply the 2D surface acoustic wave version of acoustical vortices. Nevertheless, further complexity was added by the anisotropic nature of piezoelectric substrates. Because of this anisotropy, the sound speed (and thus the wavelength at a given frequency) differs in all directions and thus isotropic "swirling SAWs" are not compatible with anisotropic substrates. So we introduced "anisotropic swirling SAWs" that are defined (with complex notations) by the formula :

$$u_z(r,\theta,z,t) = U\mathcal{W}_l^0(r,\theta) = U\frac{1}{2\pi i^l}\int_{-\pi}^{\pi} e^{il\phi + ik_r(\phi)r\cos(\phi-\theta)}d\phi$$

where u_z is the normal displacement induced by the SAW, U its amplitude and $k_r(\phi)$ defines the substrate anisotropy. For isotropic materials, we have :

$$\mathcal{W}_l^0(r,\theta) = J_l(k_r r)e^{il\theta}$$

that is simply the 2D section of a classical acoustical vortex. These anisotropic swirling SAWs have been successfully synthesized in [80] (see Fig. 3.20).

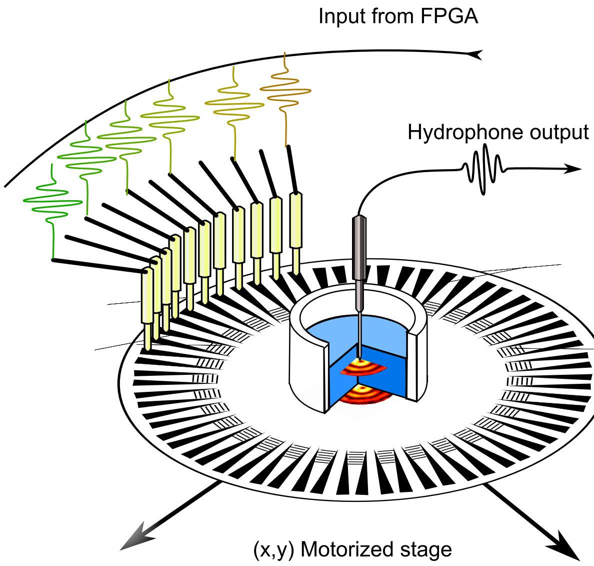

l

FIGURE 3.21: Experimental setup.)

The final challenge was to understand, predict and control the propagation of the acoustic wave generated by a swirling SAW in a liquid sample lying on the top of it. Indeed, in the same way that isotropic swirling SAWs are not compatible with anisotropic piezoelectric substrates, anisotropic acoustical vortices are not compatible with isotropic liquid. So transmission of anisotropic Bessel beams to the liquid inevitably results in degeneracy of the wavefield. But this degeneracy, instead of being detrimental to our quest of 3D single particle acoustical tweezers, leads to confined vortical waves that are in fact excellent candidates for particle trapping. Moreover the linear nature of this degeneracy allows the 3D control of this trap position by wavefront correction operated by inverse filter technique.

Details of the calculation of the transmission of an anisotropic swirling SAW to an isotropic media can be found in [81]. In the framework of moderate anisotropy (projection of the wavenumber in the substrate plane $k_i, r = k_i^0(1 + \epsilon\sin(2\phi))$, with $\epsilon << 1$), the refracted wave Ψ_l resulting from an anisotropic swirling SAW of order l can be computed with the following formula :

$$\Psi_l(r,\theta,z) \simeq t^0 e^{ik_z^0 z}\mathcal{W}_l^0(r,\theta)J_0(\frac{{k_i^0}^2\epsilon z}{k_z^0}) + t^0 e^{ik_z^0 z}\sum_{n=1}^{+\infty} J_n(\frac{{k_i^0}^2\epsilon z}{k_z^0})\left[\mathcal{W}_{l+2n}^0(r,\theta) + (-1)^n\mathcal{W}_{l-2n}^0(r,\theta)\right], \tag{3.8}$$

with k_t the wavenumber in the isotropic medium (the liquid sample), ${k_z^0}^2 = {k_t}^2 - {k_i^0}^2$ and t^0 the average transmission coefficient over all directions. In this formula, we see that the anisotropic swirling SAW $\mathcal{W}_l^0(r,\theta)$ degenerates into a combination of higher order anisotropic Bessel beams. With this formula, a coherence length Λ (characteristic length of the wave degeneracy) can be defined along with a depth of hole $\Delta_{\texttt{hole}}$ (distance required for the dark core to shrink) :

$$\Lambda \simeq 1.43\frac{k_z^0}{{k_i^0}^2\epsilon} \tag{3.9}$$

$$\Delta_{\texttt{hole}} \simeq \frac{lk_z^0\left(1 + 1.284 \times l^{-2/3}\right)}{2\epsilon {k_i^0}^2} \tag{3.10}$$

Such acoustical vortices resulting from anisotropic swirling SAWs have been synthesized inside a small liquid sample contained in a PVC cylinder of inner diameter 14 mm and height 8 mm (see a sketch of the experimental setup on Fig. 3.21). Experiments are confronted to theoretical predictions on Fig. 3.22 and Fig. 3.23, that show respectively axial and transverse cut of the vortex. The trap (dark core) can be clearly seen on the second figure.

Finally we have shown that with inverse filter the core of the vortex can be moved in the three dimensions. Fig. 3.24 illustrates the displacement of the vortex core in the acoustical scene achieved with inverse filter.

3.3.3 Acoustical twisting : toward precise vorticity control

Since we are now able to synthesize acoustical vortices from our system, the question arises of the operations that can be performed with such waves. As underlined in the previous section, acoustical vortices transport angular momentum that can be transmitted to the fluid through the attenuation of the acoustic wave and nonlinear phenomena. Thus, *acoustical vortices* can be used to generate *hydrodynamic vortices* whose topology is solely controlled by the one of the Bessel beam. In cylindrical cavities, these vortex are reminiscent of cyclones with both poloidal flow as in classic bulk streaming [7], and toroidal one due to orbital momentum transfer. Vorticity control might be of primary interest in microfluidics since it is a key point to achieve mixing at low Reynolds number [100]. In particular, precise vorticity control would help creating perfectly mixing flows. But more generally, vorticity is an essential feature in fluid mechanics

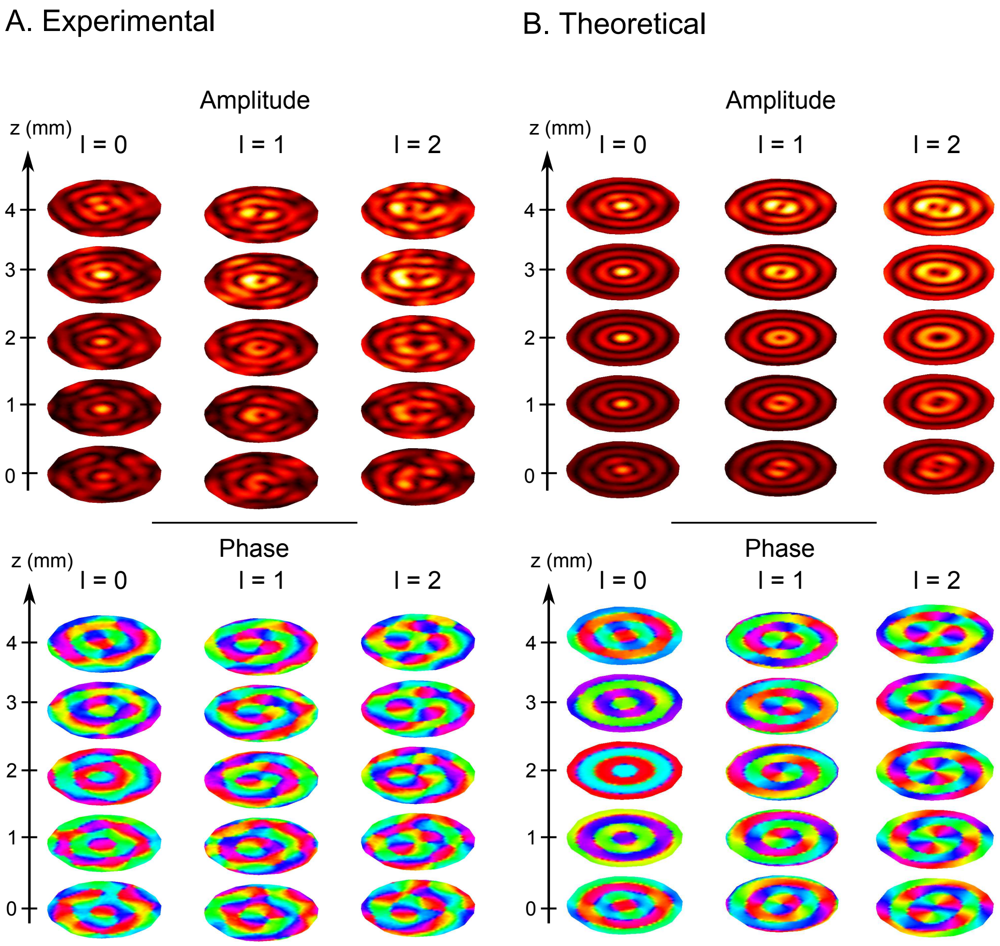

FIGURE 3.22: Anisotropic Bessel beams propagating in an isotropic fluid. The reference plane is located at $z_0 = 2$ mm. On this plane, the first bright ring radii scale linearly to the topological order and are respectively 100 and 200 μm for $l = 1$ and $l = 2$. The beams are expected to change on a characteristic distance $\Lambda \simeq 2.2$ mm and have their dark core filled after $\Delta_{hole} \simeq 1.8$ and 2.8 mm for the first and second order vortices respectively. The plotted discs have a 1 mm diameter. **A.** Experimental synthesis of confined acoustical vortices. Topological orders range from 0 to 2. Max pressure amplitudes are respectively 0.35, 0.24, and 0.26 MPa. **B.** Corresponding theoretical predictions.

and is involved in many natural and engineered systems such as fish or microorganism swimming, laminar-turbulent flow transition on plane wings, cyclones, tornadoes, ... [100–103]. Such hydrodynamics vortex generator might help a lot to investigate fundamental issues in these fields.

In 2014, we extended Eckart formulation (limited to plane waves) to investigate the acoustic streaming induced by a truncated acoustical vortex (truncation radius r_1) inside a cylinder of radius r_0. Following Eckart, the streaming is calculated by decomposing the flow into a first order compressible and irrotational flow (corresponding to the propagating acoustical wave) and a second order incompressible vortical flow (describing the bulk acoustic streaming). The

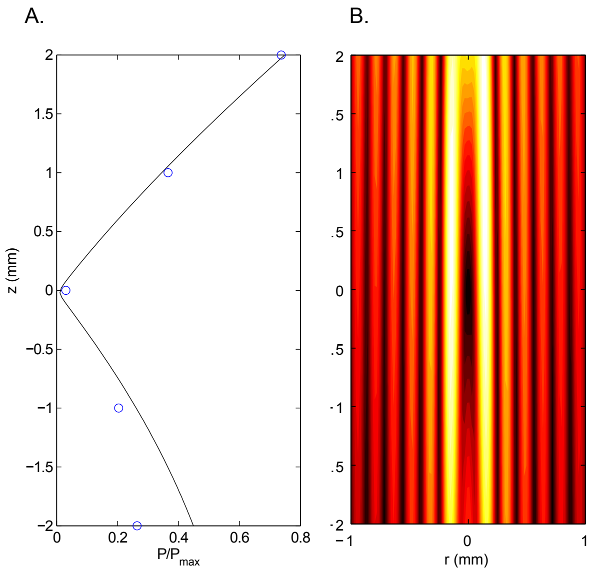

FIGURE 3.23: Anisotropic second order Bessel beam propagating in an isotropic fluid. The reference plane is located at $z_0 = 0$ mm. **A.** Pressure complex amplitude on the vortex axis for various altitudes z normalized by the maximum pressure amplitude of the first bright ring at $z = 0$. Blue circles represent experimental data points and the black solid line the corresponding theoretical amplitude. **B.** Cross-section of the complex pressure amplitude.

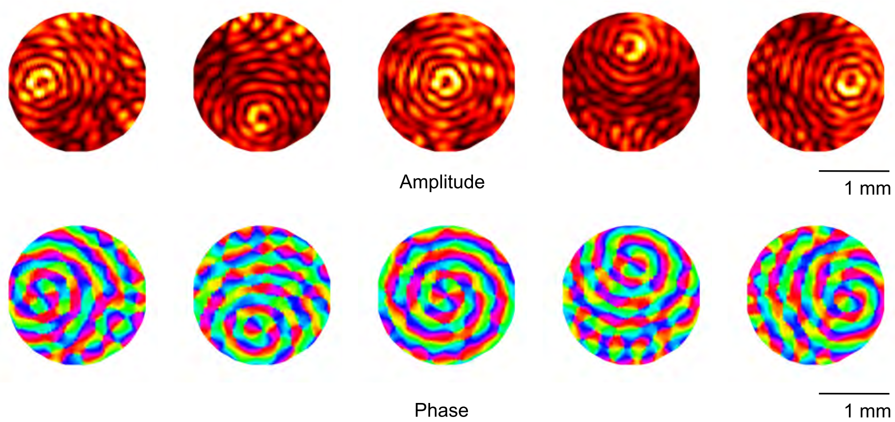

FIGURE 3.24: Synthesis of 2nd order confined acoustical vortices at different positions 2 mm above the substrate. Maximum pressure amplitude of each vortex is 0.18 MPa.

insertion of this decomposition into Navier-Stokes compressible equations yields Eckart's diffusion equation for the second order vorticity field $\vec{\Omega}_2 = \vec{\nabla} \times \vec{u}_2$, with $\vec{u}_2$ the second order velocity field. This diffusion is forced by a nonlinear combination of first order terms and simplifies at steady-state into :

$$\Delta \vec{\Omega}_2 = -\frac{b}{\rho_0^2} \vec{\nabla} \rho_1 \times \vec{\nabla} \frac{\partial \rho_1}{\partial t}, \tag{3.11}$$

with $b = 4/3 + \mu'/\mu$, μ' the bulk viscosity, μ the shear viscosity, ρ_0 the density of the fluid at rest and ρ_1 the first order density variation. Since the streaming flow is incompressible, we can introduce the vector potential $\vec{\Psi}_2$ such that $\vec{u}_2 = \vec{\nabla} \times \vec{\Psi}_2$, with Coulomb gauge fixing condition : $\vec{\nabla}.\vec{\Psi}_2 = 0$. The resolution of equation (3.11) thus amounts to the resolution of the inhomogeneous biharmonic equation : $\Delta^2 \vec{\Psi}_2 = -\frac{b}{\rho_0^2} \vec{\nabla} \rho_1 \times \vec{\nabla} \frac{\partial \rho_1}{\partial t}$. The analytical solution of this equation along with the details of the calculation are available in ref [79].

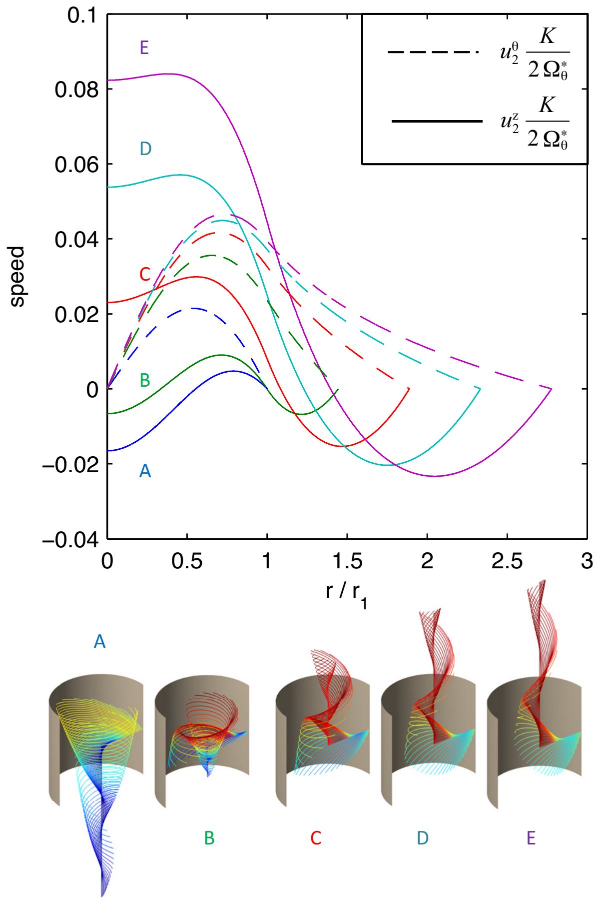

FIGURE 3.25: **Top :** Non-dimensional velocities for $l = 1$, $\tan(\alpha) = 1.21$ and $Kr_1 = 1.84$ for progressively increased cavity geometrical proportions $r_0/r_1 = [1(A) \quad 1.44(B) \quad 1.89(C) \quad 2.33(D) \quad 2.78(E)]$. Axial velocity u_2^z is represented by solid lines and the azimuthal component u_2^θ by the dashed ones. **Bottom :** Flow streamlines. Colors are indicative of the speed magnitude along u_2^z : extrema are represented by the most intense colors, red for positive and blue for negative.

An interesting point is that according to the confinement of the acoustical vortex (value of the aspect ratio r_1/r_o), either repeller or attractive vortices can be obtained (see Fig. 3.25). For repeller vortices, the fluid is pushed away from the center of the transducers and recirculate on the border of the cylinder containing the fluid. This is the situation commonly observed for streaming generated by plane waves. But for attractive vortices, the fluid recirculate at the center of the vortex in the opposite direction as the propagation of the acoustic wave. This case arises when the acoustical vortex almost entirely fills the cylinder. Indeed, generally the fluid recirculate where the wave is weaker. For a truncated wave ($r_1 < r_o$) this happens in the non-illuminated region. But if the whole cylinder is illuminated with the same intensity (e.g. with a plane wave), then the streaming body force resulting from the transfer of pseudo-momentum from the wave to the fluid is identical in the whole cylinder. As a consequence, there is no preferential direction for the fluid to flow, and thus no flow but instead an increase in the static pressure. In the case of acoustical vortices, even if the vortex completely fills the cylinder, there is less streaming body force at the center of the vortex due to the presence of the dark core. So the fluid can recirculate toward the center of the vortex (see Fig. 3.25, cases A and B).

3.3.4 3D single particle acoustical tweezers

Precise manipulation and sorting of particles and cells are key operations to design a lab on a chip and more generally in chemical and pharmaceutical engineering processes and biology.

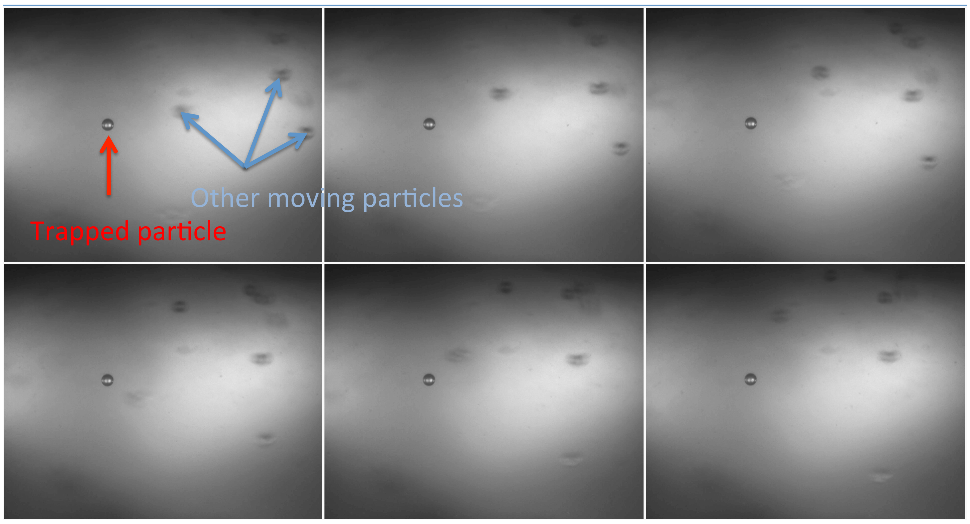

FIGURE 3.26: Polystyrene sphere of 150 μm diameter trapped with an order 2 anisotropic swirling wave of frequency 12 MHz. The trapped particle stay at the same position while other particles are moved by acoustic streaming inside the liquid shell.

As a consequence, there is an extensive literature on particle manipulations with "acoustical tweezers" based on standing surface acoustic waves (SSAW)[43–58]. In these papers, particle trapping (due to the radiation pressure) moves particles toward the nodes or antinodes of the standing wave, according to the acoustical index contrast between the surrounding medium and the particle. These tweezers are of primary interest for high throughput particle treatment such as particles sorting. Nevertheless, tweezers based on standing waves (SW-tweezers) (i) cannot select and manipulate a single particle surrounded by other particles (since every particles with the same properties will be attracted to the nodes or antinodes), (ii) cannot be used to control a few particles and modify the distance between them and (iii) are only limited to 2D particles manipulation. With acoustical tweezers based on acoustical vortices (AV-tweezers), all these limitations can be overcome, providing a tool that is more adapted for contactless selective manipulation of a restricted number of particles, and thus a complementary tool to existing ones. These AV-tweezers are the analogue of single beam acoustical tweezers in optics. Nevertheless the advantage of acoustical tweezers compared to optical tweezers ones are numerous. First, the optical and acoustical radiation forces are both proportional to the ratio of the beam power to the wave propagation speed obviously giving a major advantage to acoustics. This is one of the highest shortcomings of optical tweezers that require high light intensity (of the order of 10^7 to 10^8 W/cm^2) to obtain pN forces for micrometer size particles [86] resulting in heating of the fluid sample, which can be detrimental to the biological medium. Then, piezo-electric sources with high efficiency are available with frequencies from kHz up to a few GHz (corresponding to wavelength in liquids of the order of 1 meter to 100 nanometers) broadening the range of particles that can be trapped along with the operating distance. Finally, optical tweezers can of course be used only in transparent media.

The calculation of the acoustic radiation force exerted by a standing wave on a particle in the long wavelength regime (wavelength much larger than the particle size) was performed a long time ago by King [18], Yosika and Jawasima [19] and Gorkov [20]. On the other hand the calculation of the radiation force exerted by an acoustical vortex on a particle is more tricky since it requires the 3D computation of the scattering of the acoustical vortex by the particle. This case has been treated recently and allows to compute the force exerted by the trap on the particle [22].

In the previous section, we have shown that we are able to synthesize and displace in 3D an acoustical trap based on acoustical vortices (with operating frequency of 12 MHz). Thus we can now test it for particles trapping. As I write these lines, we performed the first successful test for particles trapping (see Fig. 3.26). We are now working on the displacement of the particle, adaptation of this technique for cells manipulation but also computation of the radiation force exerted on particles of different sizes and impedance contrast with the formula given in reference [22].

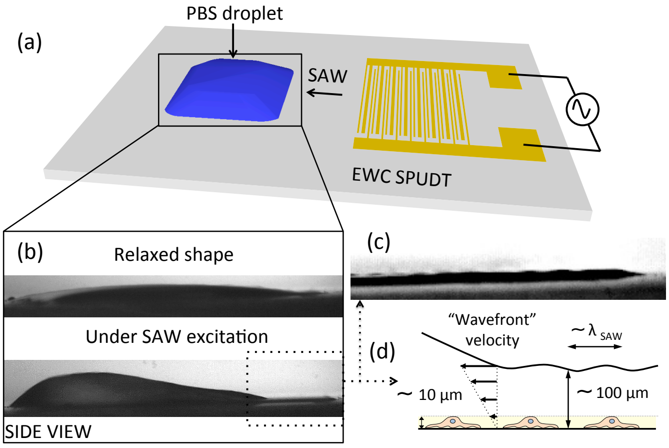

FIGURE 3.27: (a) Schematic diagram of the fluid droplet in its relaxed position spread across the 8×8 mm^2 droplet positioning zone atop the $LiNbO_3$ substrate, in relation to the SAW electrodes (EWC-SPUDT) ; (b) side-view camera images showing the two shape extrema of the droplet during one SAW excitation modulation cycle (ON : 50 ms, OFF : 150 ms). (c) Zoom on the tail section of the drop showing a standing wave pattern. (d) Flow profile in the tail section and characteristic lengths.

3.4 Applications in biology

This work has been performed in collaboration with Dr. A. Renaudin and Pr. P. Charette from UMI LN2 (Université de Sherbrooke), Dr. Y. Miron and Pr. M. Grandbois from the Pharmacology department of the University of Sherbrooke, Pr. Bou Matar from IEMN laboratory and a PhD student of our group Dr. A. Bussonière. This work is published in reference [54].

In the framework of AWESOM ANR project, we worked on a specific application of SAWs : label-free cell sorting on a droplet-based microfluidic device. Cell sorting is critical for many biological and biomedical applications such as cell biology, biomedical engineering, diagnostics and therapeutics. Indeed, numerous biological analyses are based on the separation of different cell types harvested from a raw heterogeneous sample such as whole blood. Fluorescence-activated cell-sorting (FACS)[104] and magnetic-activated cell-sorting (MACS)[105] are well established methods for cell and particle sorting known for their high-throughput and specificity. Both methods, however, require pre-processing for cell tagging with markers, an important time and cost expense for some applications.

In contrast, by making use of differences in the intrinsic physical properties of cells (size, density, adhesion strength, stiffness, electrical and optical polarizability), label-free sorting methods do not require molecular tagging. Compared to FACS and MACS, however, the specificity of label-free methods is often limited owing to insufficient contrast in physical properties, thereby restricting their widespread use. As with tagging-based systems, label-free cell-sorting methods have been implemented in microfluidic devices[106] using techniques such as deterministic lateral displacement[107], hydrodynamic filtration[108], dielectrophoresis (DEP)[109, 110], optical lattices[111, 112], stiffness separation[113, 114], acoustophoresis[115, 116] and adhesion-based sorting[117–119]. In some cases, such as for sorting based on adhesion to the substrate, performance has been improved with surface nanostructuring[118] and bio-functionalization[119] to enhance adhesion contrast between cell types.

In addition to sorting, the dynamics of cell detachment from solid surfaces is of interest in and of itself, either to harvest cells or to study the mechanisms of cell adhesion to surfaces. Cell dissociation and detachment from a solid substrate is normally achieved by cleaving bonding proteins with trypsin[120]. This process is quite aggressive as cells can be damaged if left exposed to trypsin for too long and a post-treatment rinsing step is required. In contrast, cell detachment based on microfluidic effects alone requires no external agents or rising. Cell detachment under constant fluid shear stresses has been demonstrated using spinning discs[121], flow chambers[122] and more recently using surface acoustic wave (SAW)-actuated flow[123, 124].

The miniaturization of cell-manipulation methods has led to their integration into lab-on-chip (LOC) platforms, where cell detachment and sorting have been widely investigated in flow-based microchannel formats[122, 125, 126]. Comparatively few studies[127–130], however, have explored cell separation or detachment in droplet-based microfluidics as in *digital microfluidics* (DMF)[131]. Indeed, the physics of microfluidics in droplets are completely distinct from flow-through closed-channels systems. Microfluidics properties such as bulk and surface modes of vibration, which are unique to droplet-based systems, can be exploited to great effect. In general, unlike continuous flow systems which are often optimized for high-volume cell-sorting, droplet-based systems are best suited to studies of cell properties in small populations of cells, such as cell adhesion modulation mechanisms which are highly complex and of wide-ranging interest[132, 133].

Recently[134], we presented preliminary results on the use of SAW-based fluid actuation in droplets to detach biological cells from a surface. We showed that under continuous SAW excitation, fully confluent cell layers could be detached *en masse* at sufficiently high SAW power due to acoustical streaming, whereas isolated cells were very resistant to detachment, even at power levels above the threshold for cell viability[135]. In a previous section, we showed that the acoustic power required to move or deform droplets with SAWs can be significantly reduced by using modulated rather than continuous excitation [136]. Based on this work, we have demonstrated in reference [54] that modulated SAWs can be used to viably detach cells from a surface and sort cells based on adhesion contrast, without the need for labeling. The principle of the device is presented on Fig. 3.27. Basically, two cell lines are embedded in a PBS (phosphate buffered saline solution) droplet deposited on the Niobate Lithium piezoelectric substrate used for the acoustic wave synthesis. During a fixed incubation time, the cells adhere to the surface with an adhesion strength that is characteristic of the cell line. Then modulated surface acoustic waves (of frequency 17,1 MHz) are applied to the fluid sample. Indeed, we had observed that

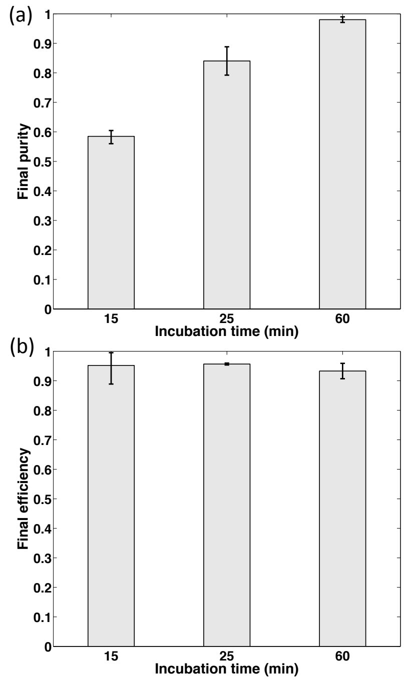

FIGURE 3.28: Cell sorting purity (a) and efficiency (b) for $LiNbO_3$ substrates prepared by incubation in a dual cell-line re-suspended solutions (A7r5 and HEK 293) for a range of incubation periods : 15, 25 and 60 min.

acoustic streaming induced by continuous excitation does not provide enough stress to detach cell from the substrate. Instead, we use the periodic sweeping of the interface induced by modulated acoustic wave to create flows with stronger gradients. Due to good wetting properties of both the Niobate Lithium substrate and the cells, a thin films always remain above the cells and protect them resulting in apoptosis rate below 5%. Finally the modulation frequency was chosen to match with interface relaxation time, so that the highest possible sweeping rate is obtained. With this device, we show that two distinct cell types (HEK 293 and A7r5) can be separated with a final purity of up to 97 % and an efficiency greater than 95 % (see Fig. 3.28). These two parameters are defined by the following formula :

$$\text{Purity} = \frac{\%\ \text{HEK 293}_{detached}}{\%\ \text{HEK 293}_{detached} + \%\ \text{A7r5}_{detached}}. \tag{3.12}$$

$$\text{Efficiency} = \%\ \text{HEK 293}_{detached}. \tag{3.13}$$

Results are achieved with characteristic processing times on the order of one minute without adversely affecting cell viability or requiring the cell layer to be fully confluent.

3.5 Conclusion

Microscale acoustofluidics is a fast developing field. Our specific approach is to take advantage of the fine nonlinear coupling between the acoustic excitation and the microfluidic response to develop original solutions that have not been investigated so far. In this quest, IEMN is a particularly well suited environment since it is possible to develop advanced microsystems with the clean room facilities, investigate the fluid response with the high speed imaging and microscopy tools available in the laboratory but also to develop theories and simulation codes with the help of the AIMAN-FILMS group, which brings together researchers with experience in acoustics, microsystems and microfluidics. Some nice challenges remain in this field, both from the physics and microsystems development points of views and our project (detailed in chapter 5) is to keep taking advantage of our specificity to differentiate our work from the abundant literature on SAWs.

Chapitre 4

Sound synthesis from two-phase micro-flows

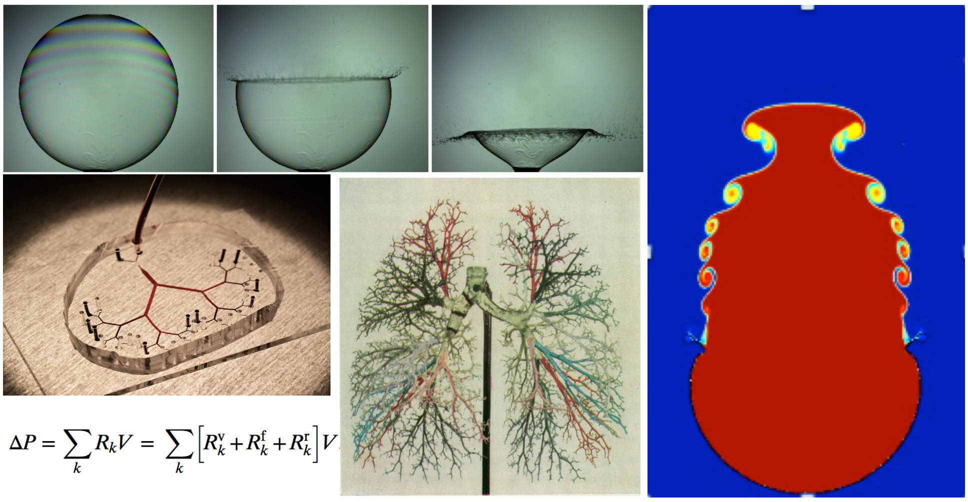

FIGURE 4.1: Stack of images illustrating some two-phase microflows leading to acoustical waves emission.

4.1 Introduction

Microfluidics flows are generally incompressible, low Reynolds and low Mach numbers. So they do not generally emit significant acoustic waves. Nevertheless, in the case of two-phase micro-flows, sound emission can be triggered by extremely rapid events such as the rupture of an interface or the impact of a drop on a rigid surface. These sounds are commonly heard when rain drops impact the ground, or when a soap bubble pops. Even the most common diagnosis tool in medicine, i.e. the stethoscope, relies on the analysis of sound produced by small scale micro-flows. Indeed, lungs are binary trees whose branches size evolve from 2 cm at the trachea down to 100 μm. In pathological conditions, the intermediate and last generations of these trees can be occluded by liquid plugs that will rupture during the breathing cycle, and produce so-called crackles sounds. The analysis of these sounds is the cornerstone of physicians daily diagnosis.

This principle could be generalized to develop micro-flows acoustical monitoring systems. Indeed, "natural" microchannels such as porous media, lung, xylem and vascular system are generally opaque and in many cases possess a complex 3D structure, which prevents the use of optical techniques to monitor the flows. As a consequence, acoustical monitoring systems would be of great use to obtain valuable information about two-phase microflows in such structures for applications ranging from oil extraction to pulmonary disease.

Nevertheless, it is necessary to reach this goal to carefully establish the link between the microfluidic flow structure and the corresponding acoustical signature. The work presented in this chapter is mostly dedicated to the study of sounds produced by liquid plugs ruptures in binary trees in connection with pulmonary obstructive disease. In the first section we study the spatio-temporal structures of airways reopening in binary networks. We show that reopening occurs through cascades of plug ruptures with specific spatio-temporal distribution. In the second section, we study the hydrodynamics of liquid plug ruptures in microchannels. Finally, in the last section we investigate the sound produced by a liquid interface rupture. This rupture is studied on the the more "academic" case of soap bubble bursting. We show that the resulting sound is very specific to the case of fluid interface rupture, and cannot be compared to the sound produced by balloons rupture, shock tubes or jets.

4.2 Airways reopening through cascade of plug ruptures in a binary network : plugs interactions and spatio-temporal distributions of the rupture events.

This work has been initiated during my postdoc at LadHyx with Pr. Charles Baroud and Dr. Paul Manneville and continued during my first years at IEMN. It was performed in collaboration with a PhD student from LadHyx, Dr. Yu Song, and has led to publications [137] and [138].

When you reach with your straw for the final drops of a milk-shake, the liquid forms a train of plugs which initially flow slowly, due to the high viscosity. They then suddenly rupture and are replaced with a rapid air flow with the characteristic slurping sound. The dynamics and rupture of trains of liquid plugs are also observed in complex geometries such as porous media during petroleum extraction [139–141], in microfluidic two-phase flows [142, 143], imbibition of paper [144, 145] or in flows in the pulmonary airway tree under pathological conditions for treatment delivery e.g. in surfactant replacement therapy [146].

The structure of the lung as a branching binary tree [147] has motivated a large number of studies on the motion of two phase flows into bifurcating channels. Many of these studies have scrutinized the flow of liquid plugs into a branching geometry [148–153], with numerical work also taking into account the elasticity of the pulmonary walls, e.g. [154].

However, nearly all of the model experiments and simulations have considered the simplest situations, either studying the motion of a single liquid plug or gas finger, or concentrating on the flow through a single bifurcation, or both. This reduces the number of independent degrees of freedom and, by the same token, the number of available states that the system can be in. These studies therefore cannot account for observations in real lungs where complex dynamics effects or even chaotic behavior are observed [155], which necessarily involve interactions over many levels in the tree.

Such interactions are primordial during the re-inflation of a collapsed lung, where the re-opening was observed to take place through avalanche events in which distinct regions were reopened in nearly singular bursts. In the experiments of Alencar *et al.* [156, 157] a degassed collapsed animal lung was re-inflated, while acoustic and pressure-volume measurements were performed at the root of the tree. They showed that the re-opening takes place in bursts, which indicates that gas invades the airways by discrete jumps. However, *in vivo* observations of the spatial behavior during re-inflation are prohibitively complex, therefore limiting the comparison between the experiments and the theoretical models [158] to measurements at the root of the tree.

Here we study the flow and rupture of liquid plugs that initially occlude microfluidic channels, as they are submitted to an imposed pressure head. Our experiments are conducted in microfluidic systems consisting of a straight channel or a branching network of channels, formed in a polydimethylsiloxane (PDMS) substrate using conventional soft lithography techniques. We show that the dynamics of a train of plugs differs from that of a single occlusion since the plugs interact together *via* both short range and long range mechanisms. The physics underlying plug interactions is first deduced from the re-opening of a single straight channel, by comparing experimental measurements with the results of a one-dimensional model. Experiments in a branching tree are then performed, showing the existence of cascades of ruptures that occur along well-defined paths through purely hydrodynamic effects.

4.2.1 Collective behavior of plugs in a straight channel

Experimental protocol

A train of liquid plugs is created inside a straight channel with rectangular cross-section of width $w = 700\,\mu$m and height $h = 55\,\mu$m, by alternately pushing liquid and air slowly through a Y-junction [151]. Perfluorodecalin is used for its good wetting properties (contact angle 23° with PDMS), consistent with those of liquid mucus in bronchial airways. Once the plugs are created and placed, a constant pressure head ΔP of 1.5 to 3.5 kPa is applied at the channel entrance. The resulting behavior is observed through a microscope equipped with a high speed camera filming at 1000 frames per second.

Single plug behavior

When a single plug of length L_0 is pushed at constant pressure, it rapidly reaches a velocity V_0 which depends on its initial resistance to flow. In its wake, it leaves a liquid film which remains at rest on the channel wall. This implies a shortening of the plug which ruptures when the length $L(t)$ reaches zero. The airway is then opened in the sense that the flow rate (of air) becomes only limited by the viscous resistance of the gas. An example of such behavior is shown in Fig. 4.2 (see also the accompanying movie), which displays snapshots of the experiment, taken at constant time intervals. The positions of the rear and front interfaces in each frame are located and interpolated to form two curves whose horizontal distance gives the length $L(t)$ of the plug. The velocity $V(t)$ is given by the slope of the curve for the rear interface. In this experiment, the velocity of the plug varies from 30 mm/s when the pressure head is applied to 280 mm/s when the plug ruptures. This acceleration generates an increase in the thickness of the liquid film left behind the plug and a subsequent rapid decrease in its length leading to rupture after 24 ms.

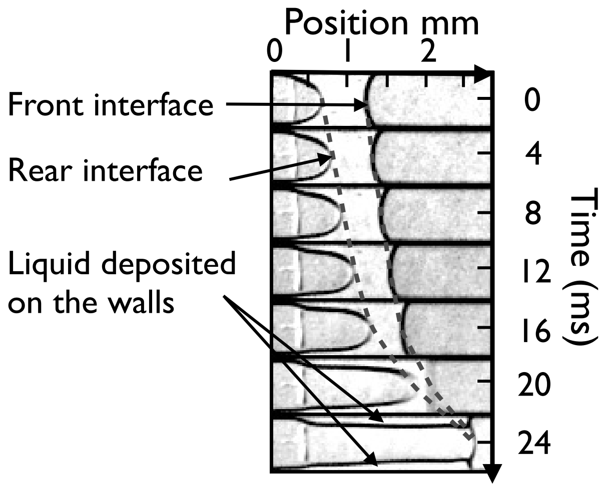

FIGURE 4.2: Spatiotemporal evolution of a single plug of initial length $L_0 = 740\,\mu$m pushed at constant pressure head 2 kPa. The montage is produced by stacking snapshots of the channel taken every 4 ms on top of each other. The liquid appears bright and the air dark. The dashed lines show the positions of the front and rear interfaces as functions of time.

The dynamics of this plug can be understood by introducing an Ohm-like law for the pressure *vs.* velocity [151, 159], $\Delta P = RV$, where ΔP is the pressure head. The velocity V of the rear interface is a measure of the flow rate and R is the resistance due to the presence of the liquid in the channel. This resistance is the sum of capillary contributions R^{f} and R^{r} of the front ('f') and rear ('r') interfaces, and a bulk viscous resistance R^{v}. Resistances R^{f} and R^{r} are due to the deformation of the two interfaces from their rest shape, in response to the large velocity gradients in the corners of the moving liquid bridge, and depend nonlinearly on V. At low capillary number $\mathrm{Ca} = \mu V/\sigma$, where μ is the viscosity of the liquid and σ its surface tension, one gets $R^{\mathrm{f,r}} = F^{\mathrm{f,r}}(h,w)\,\mathrm{Ca}^{-1/3}$. The explicit expressions of F^{f} and F^{r} are respectively obtained from the Hoffman–Tanner law [160, 161] and the Bretherton law [162] adapted to rectangular channels [163]. In turn, the bulk resistance of a long enough plug can be estimated by modeling the flow inside it as a Poiseuille flow in a rectangular channel : $R^{\mathrm{v}} \approx 12\mu L/h^2$ for large aspect ratio w/h [164].

The model describing the plug dynamics is closed with an equation for $L(t)$ that accounts for the liquid left in the stationary films on the sidewalls. Bretherton's law [162] provides a way to estimate this thickness for flow at small Ca in circular tubes. The empirical law proposed by Aussillous & Quéré [165] for circular tubes as extended to channels of rectangular cross-section and larger Ca by de Lózar *et al.* [166] is our corner-stone, which we introduce in the mass balance equation for the liquid phase : Let $S = wh$ be the area of the channel's section, S^{r} and S^{f} the areas of the lumens open to air behind the plug and ahead of it, respectively. During a time interval $\mathrm{d}t$, the volume of the fluid taken up at its front by the plug moving at speed V is $(S - S^{\mathrm{f}})V\mathrm{d}t$, the volume left behind is $(S - S^{\mathrm{r}})V\mathrm{d}t$, and the variation of the plug's volume

$S\,\mathrm{d}L$, so that the balance reads $S\frac{\mathrm{d}}{\mathrm{d}t}L = \left[S^{\mathrm{r}} - S^{\mathrm{f}}\right]V$. Whereas S^{r} is a function of V as recalled above, S^{f} solely reflects the thickness of the film present ahead of the plug at the considered time. In particular, $S^{\mathrm{f}} \equiv S$ when the plug is moving along a dry channel. Details on the model, its derivation, and its numerical simulation are given in SI of reference [137].

The dynamics of a single plug can therefore be understood with the model ingredients described above : When the pressure ΔP is applied, the plug starts moving at a velocity fixed by its initial length and physical parameters. The length then progressively decreases due to liquid deposition, thus lowering the viscous resistance R^{v}, so that the plug accelerates. Scaling as $V^{-1/3}$, the interfacial resistance also decreases, which further contributes to the velocity increase. Finally, when the length of the plug approaches zero, it ruptures. A similar behavior has been observed by Fujioka *et al.* [167] in direct numerical simulations of the flow inside a moving plug.

Multiple plug behavior

The evolution of a set of $N = 5$ plugs, forced at constant pressure head 2 kPa, is depicted in the spatiotemporal graph of Fig. 4.3a (see also accompanying movie). The plugs are initially distributed as shown in the top image and start advancing when the pressure head is applied at $t = 0$. Plugs are numbered from right to left, beginning with the most advanced one. The distance d_k between the front interface of Plug k and the rear interface of Plug $k-1$ remains nearly constant, since the air compressibility is negligible at these pressures. As a consequence, all plugs move at the same velocity $V(t)$ and the behavior of the plug train can be characterized by a single capillary number, which is plotted in Fig. 4.3a, right. We observe that Ca stays constant up until $t \simeq 180$ ms, next increases up to the time when plug 1 ruptures at $t \simeq 400$ ms, then more irregularly until $t \simeq 630$ ms (rupture of plug 2), and finally diverges around $t \simeq 800$ ms when plugs 3–5 break nearly simultaneously.

Examination of this cascade leads us to identify two plug interaction mechanisms : *Long range* effects arise from the addition of resistances within the plug train, while *short range* interactions take place between nearest neighbors via the wetting film. Indeed, plug k gains some fluid left behind by plug $k-1$ and leaves some fluid which is taken up by plug $k+1$. Since the film thickness depends on the instantaneous capillary number, the balance between the liquid intake and deposition generates plug length variations when the two layers have different thicknesses. When the train of plugs is forced at a constant velocity, for example by using a syringe pump, the thickness of the liquid films between the plugs remains constant, so that the plugs (except plug 1) always lose as much liquid as they gain and thus keep their initial length. When the plugs are pushed at constant pressure, as in Fig. 4.3, their velocity changes, which leads to variations in the film thickness. These couple back with the resistance to flow and velocities in two ways, as discussed below.

First, the resistance associated with the displacement of the front interface R^{f} decreases as the thickness of the precursor film increases. This has been demonstrated experimentally [159] and justified theoretically [168] for a single plug in a pre-wetted channel. In our experiment, the thickness of the film left behind a plug can display large changes, as seen in Fig. 4.2, which generates resistance variations for the following plug. In a train of plugs, the capillary number of a plug affects the next one with a delay equal to the time required to cover the distance that separates them. So when plug k arrives at the position initially occupied by plug $k+1$, it encounters a thicker film that decreases the resistance of its front interface and leads to an increase in velocity. This sudden acceleration is observed at $t \simeq 180\,\mathrm{ms}$ in Fig. 4.3a, which is marked by the dotted horizontal line. The second way in which neighboring plugs interact is *via* the mass balance. Like the lubrication effect, this also takes place with a delay due to plugs traveling at finite speed. Liquid exchange tends to lengthen the cascade duration since the fluid that is taken up by a plug tends to increases its length. The two short range effects are therefore antagonistic.

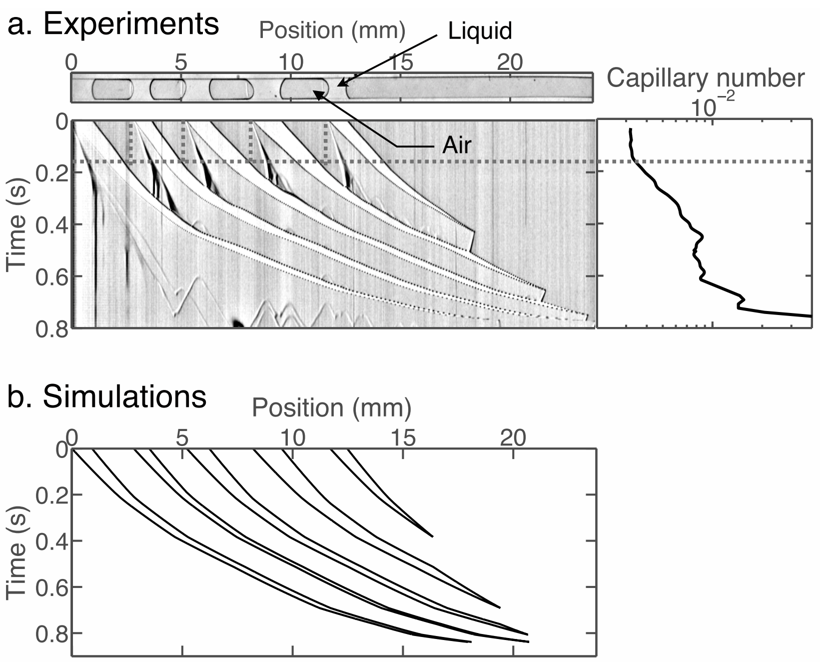

FIGURE 4.3: Dynamics of a set of equally-spaced monodisperse plugs. The initial length of the plugs is $L_{k,0} = 780\,\mu\mathrm{m}$ and the distance separating two adjacent plugs is $d_k \simeq 2\,\mathrm{mm}$. The whole train is pushed at constant pressure head $2.0\,\mathrm{kPa}$. Part a corresponds to the experiment. Top image : initial plug configuration ; liquid (air) appears light (dark) gray. Underneath : spatiotemporal diagram displaying the gray values along the center line of the channel as a function of time. Velocities and lengths of the plugs are respectively obtained from the slopes of the boundaries and the distances between them. The grey dashed line indicates the moment when each plug reaches the initial position of the previous one. On the right : Capillary number of the plug train as a function of time. Part b shows the spatiotemporal diagram obtained numerically from the model for the same conditions as part a.

Using an analogy with electrical circuits, the train of plugs submitted to a constant pressure head ΔP can be viewed as a series of resistors and the total resistance as the sum of the individual resistances. So, rupture of plug k implies *long range* effects because it corresponds to a sudden drop to zero of the corresponding resistance. Consequently the speed of the remaining plugs suddenly increases, which further hastens the deposition of the wetting film and induces new ruptures. This catastrophic speeding-up is at the origin of the cascade observed in our experiments. It is easier to observe when the initial distribution of plugs is irregular and their size polydisperse. An example is shown in Fig. 4.4, where a train of ten plugs is pushed at constant pressure head (see also accompanying movie). The evolution of the train is mainly dominated by short range interactions until $t = 300\,\text{ms}$ (dotted line), when three plugs break nearly simultaneously. The velocity of the remaining plugs then displays a large increase and the subsequent ruptures take place within shorter and shorter time intervals, all the remaining plugs being broken between $t \simeq 320\,\text{ms}$ and $t \simeq 370\,\text{ms}$. The rapid variation of the velocity points to the finite-time singularity nature of the cascade. Whereas the short range interactions act, as said, with a delay, the long range effects are instantaneous, owing to the immediate re-adjustment of the pressure field and velocities.

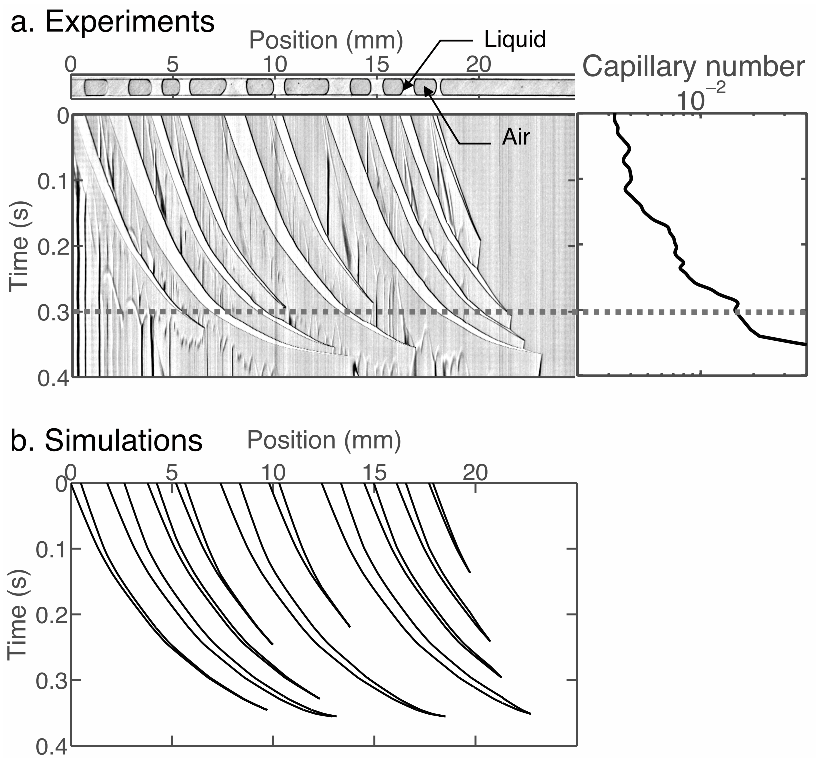

FIGURE 4.4: Dynamics of a set of polydisperse plugs pushed at constant pressure head 4.8 kPa. Panel a and b display the plug positions as functions of time, experimental and simulated, respectively. The variation of the capillary number with time is given to the right of Panel a where the grey dashed line indicates the time when several plugs break almost simultaneously.

Model and simulations

Since at a given time all plugs move at the same speed, interactions between plugs can be treated by generalizing the equation for a single plug to a series of plugs : $\Delta P = \sum_{k=1}^{N} R_k V$, where R_k is the resistance ascribed to plug k. The lubricating role of the wetting film thickness is taken into account by expressing the front interface resistance R_k^{f} as a function of the surface $S(x,t)$ of the lumen open to air ahead of plug k at position x and time t. Let x_k denote the position of the rear interface of plug k, since the front interface is at $x_k + L_k$ the surface to be considered is $S(x_k + L_k, t)$, itself determined by the history of the previous plugs, $k-1$, $k-2$, $\dots$ while ahead of plug 1, the surface is just $S(x > x_1 + L_1) = wh$. The configuration of the channel can then be computed as a function of time once the conservation of liquid is expressed. For each plug we thus get : $\frac{\mathrm{d}}{\mathrm{d}t} L_k = -\left[1 - S(x_k)/S(x_k + L_k)\right] V$. The surface $S(x_k)$ of the lumen behind plug k then serves as an input in the computation for plug $k+1$. Plug rupture takes place when $L_k = 0$ and is accounted for by setting $R_k = 0$. The positions of the plugs can be obtained by integrating the velocity V. A detailed derivation of the model and the numerical scheme are given in SI of reference [137].

The results of the model are shown in the bottom panels of Fig. 4.3 (monodisperse) and Fig. 4.4 (polydisperse), which show that the motion of the plugs and the order of plug ruptures are correctly reproduced. Quantitative predictions from the model were compared with results from experiments with trains made of one to seven plugs. Two quantities were measured : (i) the time t_c required for complete reopening of the airway (all plugs have ruptured), called *cascade duration*, and (ii) the *penetration length* L_c, which is the distance between the initial position of plug 1 and its position when it breaks, also indicating how long the channel has to be for a cascade to be observed. Results are presented in Fig. 4.5, where each square marks a single run.

The dashed line corresponds to the predictions obtained with the full model which takes into account all the processes described above. In contrast, the dashed-dotted lines, in panels a and b, show the predictions when short range effects are neglected, i.e. when the resistance of all plugs are just summed as if each of them were alone in the channel : $\Delta P = N\, R_s\, V$, with N the total number of plugs and R_s the resistance of an isolated plug. When the interactions are neglected, the cascade duration and the penetration length are grossly underestimated and the discrepancy increases with the number of plugs, stressing the role of liquid exchange between plugs. This shows that the interactions play a dominant role in the dynamics of the train, increasing the quantities of interest by a large factor. The experiments were repeated in order to measure the cascade duration and penetration length as functions of the imposed pressure head and the results are shown in Fig. 4.5 c,d. The model agrees quantitatively with the experiments at low pressures but discrepancies appear above 2.5 kPa. This departure is attributed to the fact that the theoretical expressions used for interface resistances are only valid at low capillary numbers. Although individual resistances are not sufficiently well estimated during the fastest part of

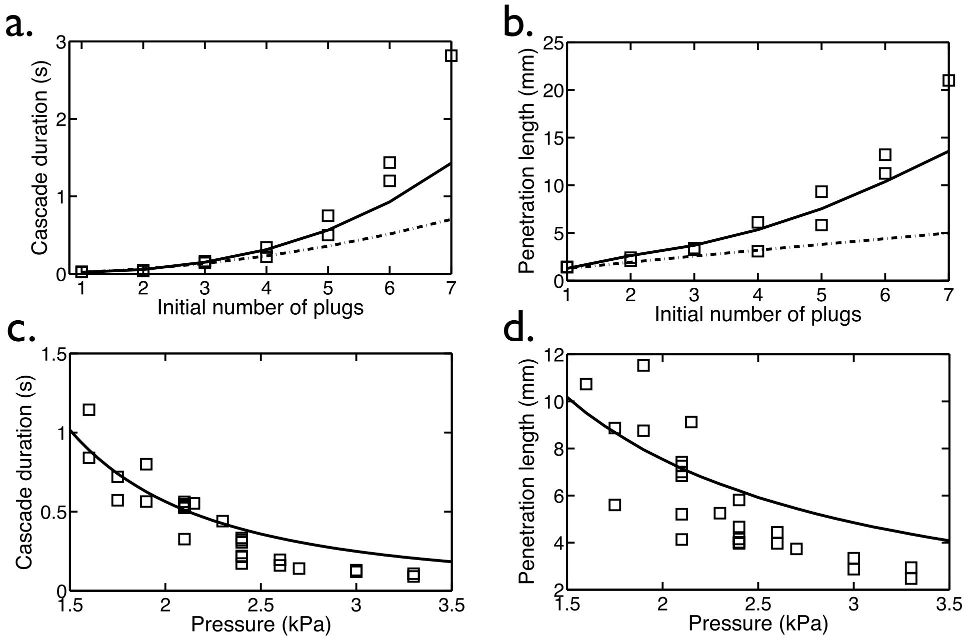

FIGURE 4.5: Evolution of the cascade duration (a,c) and the penetration length (b,d) as functions of the number of plugs (a,b) and applied pressure (c,d) for a set of monodisperse plugs of length 0.78 mm separated by 2.1 mm. In (a,b) the pressure head is 2.0 kPa. Squares correspond to experiments, dashed-dotted curves to predictions from the model without plug interactions, and continuous curves to predictions of the model taking short and long range interactions into account.

the cascade, the model can still serve as a good basis for predicting the cascade duration and penetration lengths in straight rectangular channels.

4.2.2 Cascade of plug ruptures in a bifurcating network

When considering an initially occluded tree structure, such as the pulmonary airway, the processes described above must be adapted to account for geometry effects : the division of plugs at bifurcations and the interactions across different regions in the network [152]. This has been studied in a series of re-opening experiments performed by replacing the straight channel with a six-generation tree network, as shown in Fig. 4.6. The widths of channels making two successive generations are chosen according to the diameter ratio in Weibel's symmetrical model of the human lung [147], i.e. $w_{i+1}/w_i = 2^{-1/3}$, where w_i is the width of channels in generation i and $w_1 = 720\,\mu$m. The height of channels is $45\,\mu$m everywhere.

The same protocol as for the straight channels is used. The experiment begins by alternately injecting liquid and air into the root channel to form seven successive plugs that split and distribute in the tree. The sequence of pressures during the injection procedure is computer controlled and kept unchanged for all runs. As plugs advance into the tree, they divides into two daughters when reaching a bifurcation. Slight perturbations may affect plug divisions at each run, so that the initial distributions differ slightly from one experiment to the next in spite of the network symmetry.

A typical experiment is shown in Fig. 4.6 (see also accompanying movie). Once the initial plug distribution is installed (Fig. 4.6a), after waiting sufficient time to make sure that the system is at rest, a high pressure difference (3.5 to 5.5 kPa) is applied between the root and the exits of the network kept at atmospheric pressure. The flow rate in each path is determined by the pressure difference, which is equilibrated by the sum of the resistances through each branch of the path. Small differences in the initial distribution of plugs lead to variations in flow rates among paths, which are then amplified as the liquid plugs make their way in the network. Ultimately, one path reopens through a cascade of plug ruptures (Fig. 4.6b).

This first cascade is followed by several others, each opening a different path (Fig. 4.6c, numbers indicate the order in which cascades occur). The spatial distribution of the cascades is irregular ; they can either take place in adjacent paths (e.g. 3 and 4) or in well separated paths (e.g. 4 and 5). Cascades break the network into independent subnetworks, each with its own dynamics.

The pressure driving each subnetwork can be inferred by considering the air flow in the reopened path. Since the pressures P_{in} at the root and P_{out} at the exit are fixed, the flow of air that takes place in the reopened path determines the intermediate values of the pressure along the path. A typical situation is shown in Fig. 4.7 (left), where the last five generations of the network are displayed before and just after re-opening of path A. The whole subnetwork is thus initially driven at the common pressure P_{in}. But, once the cascade takes place along path A, the tree gets separated into three subnetworks N1, N2, N3 driven at three intermediate values of the pressure P_1, P_2, P_2. The smaller the subnetwork, the lower the pressure head driving it. On the other hand, the smaller the subnetwork, the fewer plugs it contains, and hence the lower resistance to flow. It is therefore *a priori* not obvious which path will be taken by the next cascade.

The readjustment of the driving pressure after each cascade leads to a spacing out of successive cascades in time. This is shown in Fig. 4.8a where a histogram of individual plug ruptures is plotted as a function of time. Ruptures appear to be clustered in groups, which are labeled using the same numbering scheme as in Fig. 4.6. The first cascades develop when a large part of the network is still occluded and involve many simultaneous plug ruptures. In contrast, later cascades involve fewer plugs and affect shorter paths of the tree. The time separating successive cascades, initially short, gradually increases in all experiments.

The spatial distribution of re-openings is measured by introducing a quantity $\xi(N)$ which measures the cumulated number of branches, between the root and generation 4, that are reopened by cascades 1 to N (Fig. 4.8b). The first cascade always corresponds to $\xi(1) = 4$, since all four generations are occluded. However, the evolution of ξ between successive cascades depends on

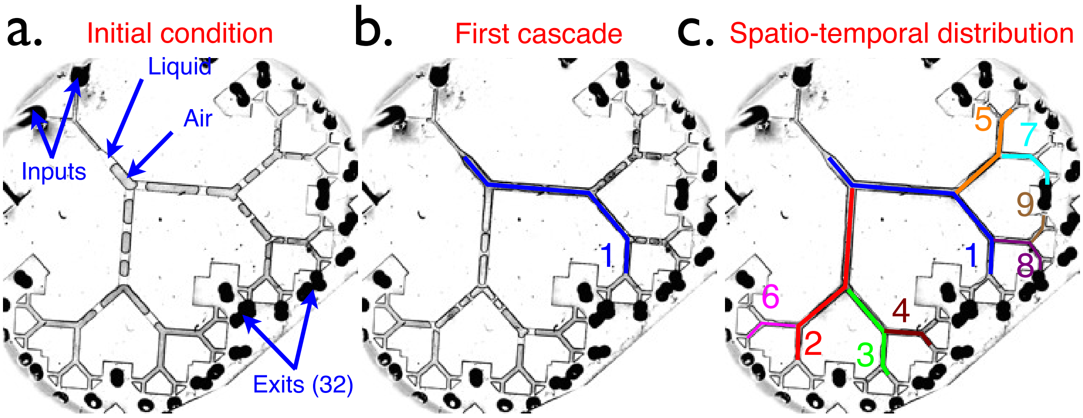

FIGURE 4.6: Initial distribution of plugs and spatial distribution of successive airways re-openings obtained by pushing an initial set of liquid plugs by $\Delta P = 3.5\,\mathrm{kPa}$ in a six-generation network. A given path is 'open' when the plugs obstructing the air flow from entrance to exit all along that path have ruptured. Paths are numbered according to the re-opening order.

the size of the reopened sub-network and thus on the spatial distribution of successive reopenings. The minimum and maximum values of $\xi(N)$ are plotted in Fig. 4.8. They are obtained by examining all the possible scenarios in the network. Alternatively, $\xi(N)$ for a random distribution of reopenings is obtained numerically by repeating the simulation a number of times and taking the mean value of $\xi(N)$ for a large number of realizations.

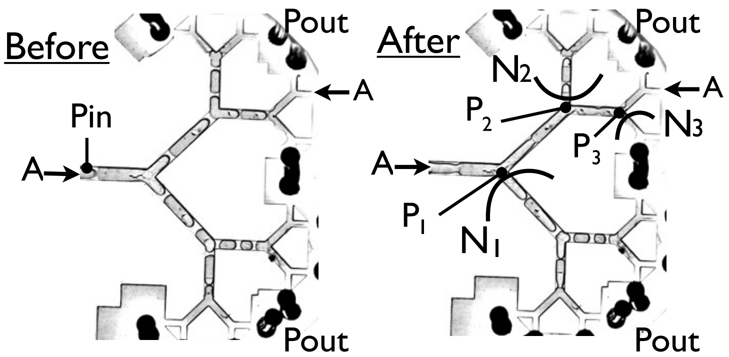

FIGURE 4.7: Snapshots taken before and after the re-opening of the path corresponding to the first cascade. The opened path is A. Its ends are marked with arrows. P_{in} and P_{out} are the pressures at the entrance and exit of the relevant network branch, P_1, P_2, and P_3 the intermediate pressures at the first, second, and third node after re-opening.

Measurements of ξ were performed for three different driving pressures, 4.0, 4.5 and 5.0 kPa by repeating each experiment eight times. The average value of $\xi(N)$ for the eight realizations is indistinguishable from the random prediction, as shown by the black symbols in Fig. 4.8b . The results for a particular experiment however tend to fall on either the minimum or maximum value, as shown by the light-grey symbols. This behavior is due to the complex fluid redistribution when a plug divides at a bifurcation, which depends on the large-scale organization of plugs everywhere in the network. This redistribution can lead to paths being suddenly strengthened or weakened, as more or less liquid enters into the branches that make them up during a plug division. The redistributions of liquid was found to display extreme sensitivity to the initial conditions, making the prediction of the direction in which the plug will divide impossible. On average, Fig. 4.8 shows that the behavior is indistinguishable from a random distribution.

4.2.3 Discussion

Two important differences must be noted between cascades in straight channels and cascades in a bifurcating tree. First, the plug divisions add a strong random component to the dynamics in the network, as described above, which reduces the ability to predict the cascade duration or direction. And second, the forcing applied to each branch is different and depends on the distribution of the plugs in the whole network.

This work constitutes a first step toward the comprehension of liquid plug flows in complex structures such as the pulmonary tree. Nevertheless, it will be necessary in the future to study these flows in more realistic geometries and forcing conditions to reach quantitative prediction of the flow in obstructed pulmonary airways.

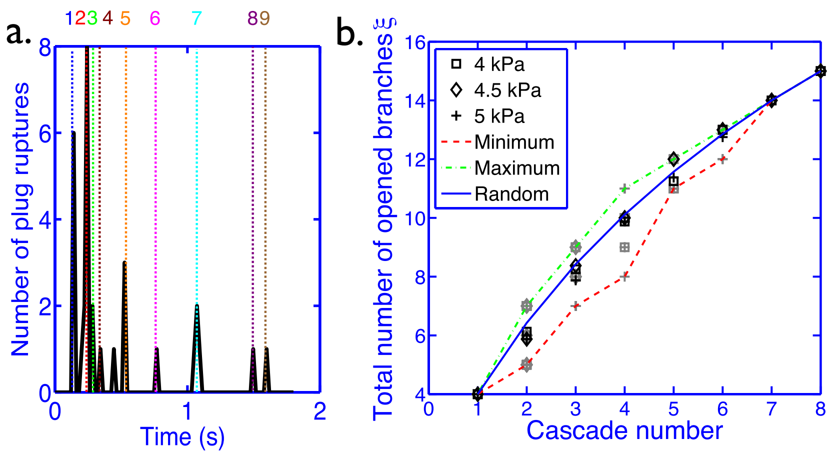

FIGURE 4.8: a. Histogram of the number of plug ruptures as a function of time. The dotted lines indicate re-opening times of each cascade. b. Total number ξ of opened branches (in which air can flow freely) measured after each cascade. The black symbols show the variations of ξ obtained experimentally for the driving pressures shown in the legend by averaging results over 8 experiments for each pressure. The grey symbols correspond to a typical experiment. The curves connect maximum (dashed-dotted green) and minimum (dashed red) values of ξ observed and the average predicted value for supposedly random openings.

4.3 Study of the hydrodynamics of a liquid plug rupture.

This work is currently underway in collaboration with Pr. Farzam Zoueshtiagh from IEMN laboratory and Juan Carmelo Magniez, a PhD student from our group and benefited from discussions with Dr. Stéphane Popinet on numerical aspects.

Recently, we started to investigate both numerically and experimentally the last moments of plug ruptures in capillary tubes for different driving pressures and capillary tube sections. This study is crucial to understand how sound is produced by plugs ruptures as we shall see in the next section but also to get further insight of the production of aerosols during cough [169]. Our preliminary results show that the rupture of the liquid plug strongly differs upon the Capillary and Reynolds numbers (or equivalently Weber and Reynolds numbers) and that interestingly, the plug rupture produces well calibrated droplets in a specific range of these dimensionless numbers.

4.3.1 Experimental results

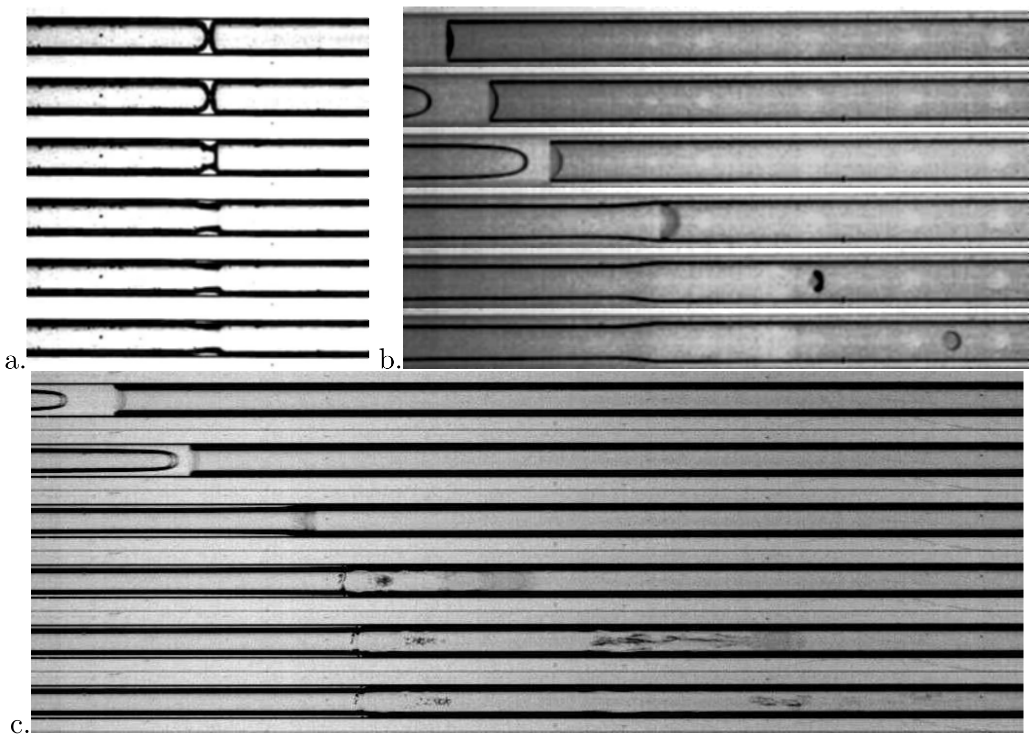

FIGURE 4.9: Rupture of a liquid plug of 7 μl recorded with a high speed camera at 15000 frames per second. a. Pressure head : 1 mbar / Time elapsed between two successive images : 0.6 ms / Capillary number just before the plug rupture : $Ca = 9 \times 10^{-3}$. b. Pressure head : 5 mbar / Time elapsed between two successive images 4 ms / Capillary number just before the plug rupture : $Ca = 0.5$. c. Pressure head : 40 mbar / Time elapsed between two successive images 0.6 ms / Capillary number just before the plug rupture : $Ca = 1.4$.

Experimental protocol

A glass capillary tube of radius $R = 0.5$ mm is prewetted by a thin layer ($h/R \approx 1\%$) of a wetting liquid (Perfluorodecalin) by pushing a first liquid plug at constant flow rate inside the channel. This liquid plug is created by pushing alternatively some liquid and some air at a T-junction. Then, a second liquid plug is inserted inside the tube and a constant pressure head of 1 to 40 mbar is applied at its entrance with a MFCS Fluigent controller. The evolution of the liquid plug is recorded at 15 000 to 20 000 frames per second by a Photron SA3 high speed camera mounted on a Z16 Leica macroscope working with a high intensity light. Finally, images are treated with ImageJ software.

Results

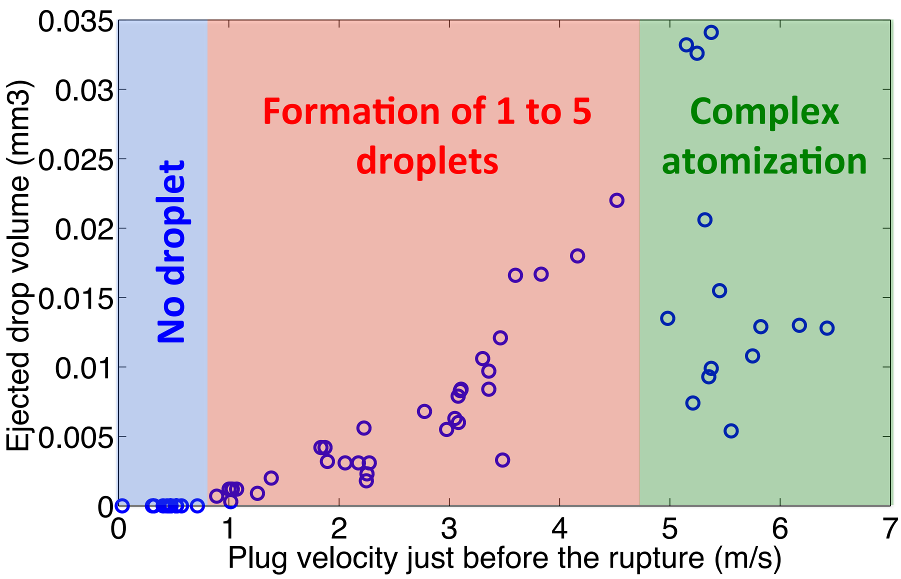

FIGURE 4.10: Volume of the ejected drops as a function of the terminal velocity of the plug before its rupture. Blue region : no ejection. Red region : ejection of 1 to 5 droplets. Green region : complex atomization

Fig. 4.9 shows the last moment of a 7 μl liquid plug rupture for different pressure heads. At small capillary numbers, the curvature of the front and rear interface are only slightly deformed compared to their static values and thus rupture happens at the center of the channel. After the rupture, the liquid contained in the caps spreads on the walls. This situation is well described by the model developed in the previous section. At larger capillary numbers, stresses in the liquid are sufficient to inverse the curvature of the front interface, leading to the detachment of a liquid film that collapses into a droplet of well defined size. Finally, at the largest capillary numbers, the liquid film is atomized into tiny droplets. After the rupture of the film, the increase in the flow rate associated with the sudden decrease in the flow resistance lead to destabilization and then atomization of the liquid film covering the walls.

Since the intermediate regime leads to the formation of droplets at the center of the channel (which might be interesting for many applications) ,we wanted to further investigate it. We thus studied the volume of the ejected drops as a function of the plug velocity just before its rupture (see Fig. 4.10). The terminal plug velocity is directly correlated to the pressure head applied with the controller but since we were using a 0-345 mbar MFCS pressure controller, uncertainties in the applied pressure lead to high variability in the size of the droplets, while excellent correlation is found with the ultimate plug velocity. This figure shows that plug rupture is an extremely simple way of creating well calibrated droplets without the need of piezoelectric systems. Different regimes are observed experimentally : for low pressures there is no droplet formation. Then a well defined number of droplets is formed through retraction of the liquid film after its detachment from the wall. Finally, atomization of the liquid film occurs. To achieve better precision, new experiments are underway with a 0-25 mbar controller that has a lower response time and better pressure resolution.

4.3.2 Numerical simulations

The behavior described in the previous section is well reproduced with Gerris, a finite volume software with VOF (Volume of Fluid) interface tracking method, and quad-tree square spatial discretization allowing mesh refinement. Fig. 4.11 shows that we are indeed able to simulate the different regimes observed experimentally. Nevertheless, direct comparison with experiments is complicated due to a numerical artifact. Indeed, the pressure equilibrium is reached extremely rapidly in the experiments due to compressibility effects once the pressure head is applied. However, since Gerris is an incompressible software, more time is required for this equilibrium to be reached. Since the liquid plug is continuously accelerating (as seen in the previous section) when a pressure head is applied, it is not possible to reach the same evolution numerically and experimentally. More precise comparison between experiments and numerics is underway by performing experiments at constant driving flow rate. We are also trying to find some analytical models that will help predict the size of the emitted droplet as a function of the driving pressure.

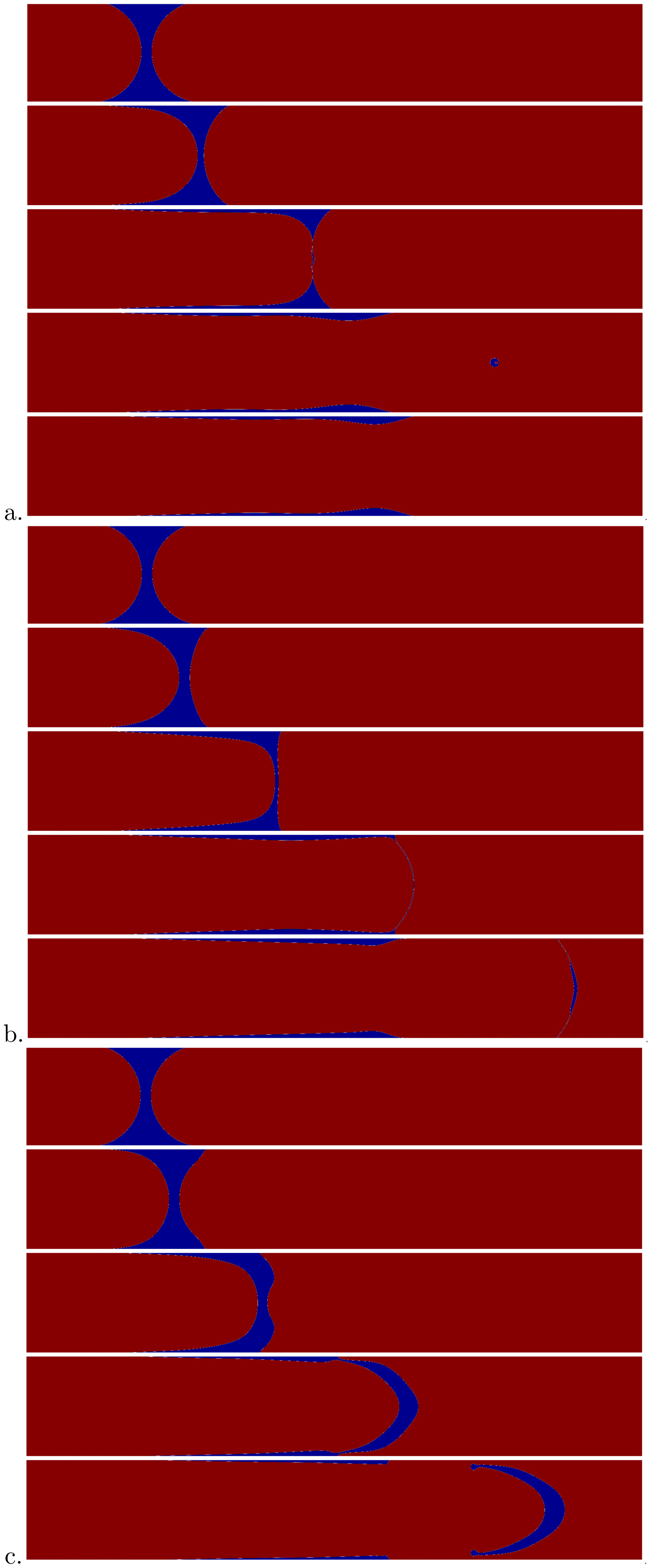

FIGURE 4.11: Evolution of a liquid plug of a 7 μl pushed at constant pressure in a tube of radius $R = 0.5$ mm simulated with Gerris. For Fig. a., b. and c. the driving pressures are respectively 1, 10 and 100 mbar.

4.4 Sound emitted by liquid films rupture : the case of soap bubble bursting

This work is currently underway in collaboration with Dr. Arnaud Antkowiak, Dr. François Olivier and Pr. R. Wunenburger from Institut Jean le Rond d'Alembert and Dr. Adrien Bussonière, who is currently doing a postdoc in this laboratory in collaboration with IEMN.

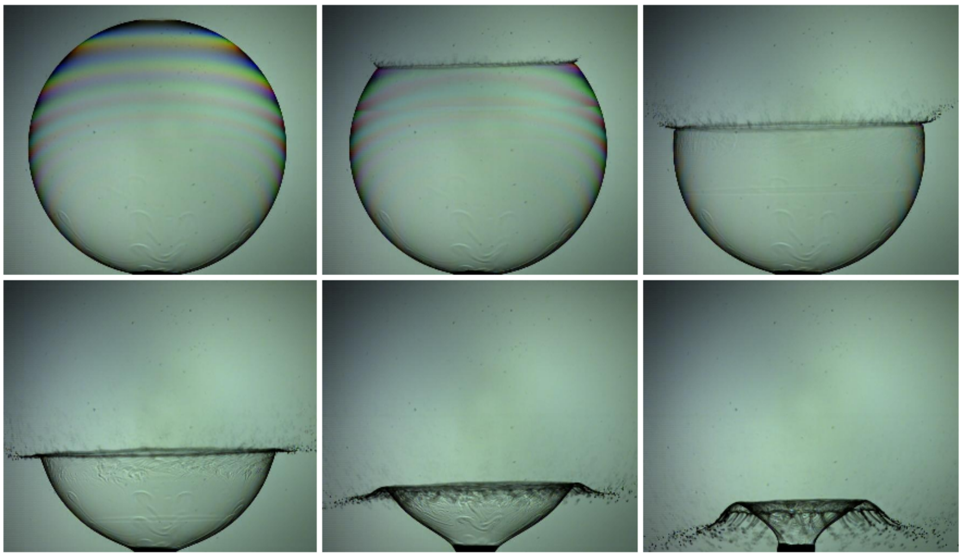

FIGURE 4.12: Bursting of a 4 mm radius soap bubble captured with a high speed camera.

The rupture of thin liquid films has been studied extensively for over a century since it is involved in a wide range of processes in physics, chemistry, geology and engineering [170–172]. The initial observations of soap film rupture dates back to the work of Dupré in 1867 [173] and Rayleigh in 1891 [174]. Their studies motivated the experimental work by Ranz (1950) [175], who measured the retraction speed of the liquid sheet and showed that this velocity remains constant. From a theoretical point of view, Dupré and Rayleigh were the first to propose an estimation of the retraction speed of the film based on a simple energy balance assuming that all the capillary surface energy lost from the retraction of the film is purely turned into kinetic energy. This approximation led nevertheless to significant discrepancies compared to the experiments of Ranz. Later on, Taylor (1959) [176] and Culick (1960) [177] independently corrected Dupré's calculation by taking into consideration the mass variation of the rim in the momentum balance. Nevertheless they assumed that the velocity of the rim is constant to determine its value, without further justification. Savvy and Bush [178] showed that while viscous dissipation is not directly considered in this calculation, it still holds for viscous sheet retraction, as first suggested by Culik. They also showed from rigorous calculation why the velocity is uniform. Finally, it was shown both experimentally and theoretically that different rupture regimes can be observed depending on the value of the Ohnesorge number $Oh = \frac{\mu}{\sqrt{2h_o\rho\sigma}}$ (with μ the liquid viscosity,

h_o the thickness of the film, ρ the liquid density and σ the surface tension) that compares the driving mechanisms (inertia and surface tension) to the dissipation ones (viscous dissipation). At low Ohnesorge numbers, the capillary wave disturbances are generated ahead of the retracting rim. At intermediate Ohnesorge numbers, the capillary waves disappear and the rim diffuses in towards the bulk of the sheet. Finally, at high Ohnesorge numbers, no rim forms and the thickness of the film is uniform.

On the other hand, few studies have been devoted to the popping sounds resulting from the bursting of soap bubbles. Most of them are dedicated either to the sound produced by the bursting of a bubble located at the surface of a liquid pool [179, 180] or a soap film initially closing an over-pressurized cavity [181] [182]. The first case is observed in air-sea interactions or champaign bubble bursting while the second case is relevant to the sound produced by volcanoes. But the physics in these two cases strongly differs from the behavior of a free soap bubble since the bubble is then surrounded by either a liquid or a solid wall that are almost perfectly reflecting acoustic waves and thus create acoustical cavities. Consequently, bubble bursting at the surface of a liquid produces sounds that are very similar to the one produced by Helmholtz resonators.

In the case of soap bubbles, there is also an overpressure inside the bubble, but the bubble surface is almost transparent to acoustical waves. Indeed, since its thickness is about $h_o = 1\mu$m it can only perturb acoustic waves of frequencies of the order of $c/h_o \approx 340$ MHz, far above the sound emitted by the bubble rupture. The only measurement of the sound produced by a single soap bubble rupture has been performed by Ding et al. [183] but there is no analysis of the spatio-temporal waveform of the signal and no attempt to correlate it with the bubble rupture dynamics.

In this work we show that the sound produced in such a case is very specific and cannot be described by existing theories developed for the rupture of balloons, the sound emitted by jets or shock tubes. In particular, we show that the finite speed of liquid film retraction during the bubble opening must be considered to properly model the sound source.

4.4.1 Experimental procol

A bubble of water and SDS surfactant (Sodium Dodecyl Sulfate) at CMC (Critical Micelle Concentration) is produced by depositing a droplet of 0.3 to 2 microliters at the extremity of a capillary tube and pushing a prescribed volume of air of 0.1 to 3 milliliters with a syringe pump to reach different bubbles sizes and thicknesses. Then, bubble rupture is either achieved *naturally* by the drainage of the liquid from the top of the bubble to its root induced by gravity or *forced* with a needle. Finally, the dynamics of rupture of the bubble is recorded with a high speed camera Photron SA3 and the sound is recorded by a combination of a large band microphone (bandwidth of 100 kHz), a high sensitivity microphone (bandwidth of 10 kHz) and a MEMS

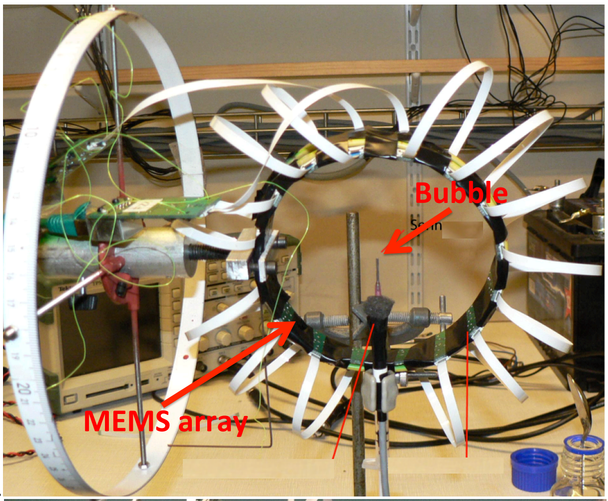

a.

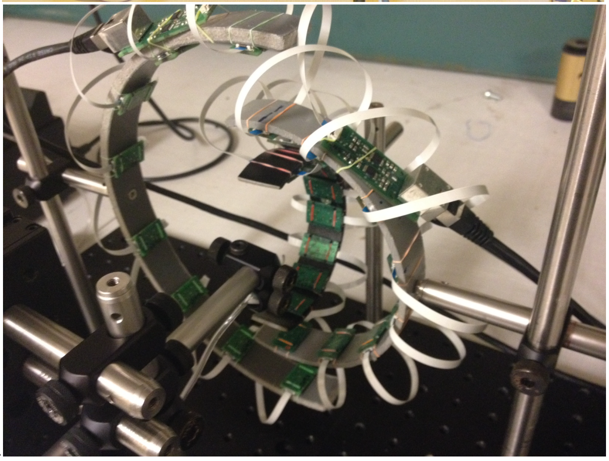

b.

FIGURE 4.13: MEMS array used to measure the spatio-temporal form of the wave. a. First version with a single array b. Second version for measurement in two orthogonal planes

array with smaller sensitivity and bandwidth (10 kHz) disposed around the bubble that allows a spatio-temporal measurement of the wavefield (see Fig. 4.13).

4.4.2 Analysis of the wavefield

Introduction : On the sound produced by an "instantaneous" bubble rupture

In his book [184], Whitham develops an analytical model that predicts the acoustic wave emitted by the rupture of a spherical balloon. To obtain the equations, he assumes that the rupture of the balloon produces a pressure discontinuity at the former location of the shell that will then propagate in the air. This amounts to supposing that the characteristic speed of the shell rupture is more rapid than the sound speed.

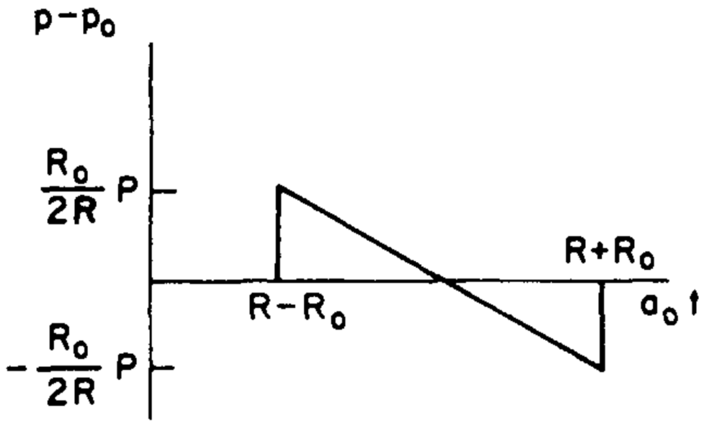

FIGURE 4.14: N-type monopolar shock wave predicted by Whitham for the sound produced by a balloon rupture.

The acoustic wave is computed by solving Helmholtz equation in spherical coordinates :

$$\frac{1}{c^2}\frac{\partial^2 \varphi}{\partial t^2} = \frac{\partial^2 \varphi}{\partial r^2} + \frac{2}{r}\frac{\partial \varphi}{\partial r}$$

whose solution is the sum of a convergent and divergent spherical wave : $\varphi = \left(f(r-ct) + g(r+ct)\right)/r$, with r the radius, φ the velocity potential, t the time and c the sound speed. Then the following initial condition is considered at $t = 0$:

$$\varphi = 0, \quad \frac{\partial \varphi}{\partial t} = \begin{cases} -\frac{P}{\rho_g}, & r < R_o \\ 0, & r > R_o \end{cases}$$

with R_o the radius of the bubble prior to bursting, and P the overpressure in the bubble due to the presence of the shell.

These equations predict the emission of a N-type monopolar shock wave, whose wavelength is equal to twice the initial radius of the balloon R_o and whose period is equal to $2R_o/c$, with c the sound speed in the air (see Fig. 4.14). In the following, we will show that the sound produced by bubble bursting is quadripolar and that the period of the wave emitted is not compatible with Whitham theory.

Analysis of the temporal signature of the signal

The sound produced by a soap bubble rupture can be seen on Fig. 4.15 (Fig. a corresponds to the temporal signature measured in the near field 5 mm away from the top of the bubble and Fig. b. to the temporal signature in the far field 75 mm away from the bubble). We can see on this graph that the period of the signal T_{exp} is typically of the order of 1.5 ms for a bubble of radius 4 mm and walls thickness of approximatively 1 μm.

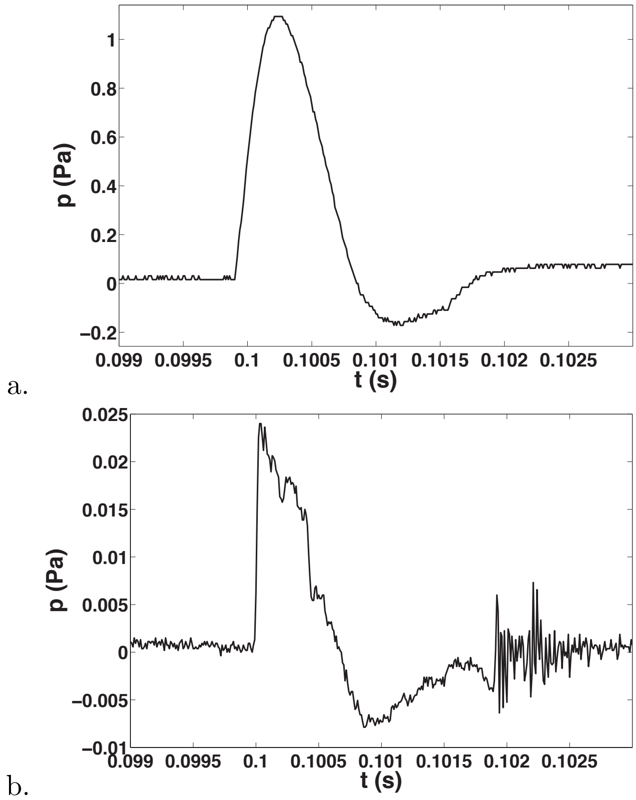

FIGURE 4.15: Pressure wave emitted by the bursting of a bubble. a. Near field (5 mm from the top of the bubble). b. Far field (75 mm from the top of the bubble). p is the pressure in Pascal and t the time in second.

Different phenomena could be at the origin of this acoustical wave : (i) the radiation of an initial pressure discontinuity as predicted by Whitham, (ii) the production of acoustic sources by the progressive opening of the bubble and (iii) the sound produced by the jet of air expelled from the bubble. The characteristic time T_{nw} associated with the first phenomenon (N-wave) can be directly determined from Whitham's theory : $T_{nw} = 2R_o/c$. Then, if we consider that the bubble opens due to the retraction of the liquid film at the so-called Taylor-Click velocity $v_{tc} = \sqrt{\frac{2\sigma}{\rho_l h_o}}$ [176, 177], the characteristic time T_{tc} associated with the bubble opening is $T_{tc} = 2\pi R_o/v_{tc} = \pi\sqrt{\frac{2R_o^2\rho_l h_o}{\sigma}}$, with h_o the thickness of the liquid film surrounding the bubble. Finally, the characteristic time associated with the air jet T_{jet} can be estimated from the following analysis : The jet is driven by the Laplace overpressure resulting from the presence of the interface : $\Delta p = \frac{4\sigma}{R_o}$. Then, Bernoulli's equation gives a jet velocity equal to $v_{jet} = \sqrt{\frac{2\Delta p}{\rho_g}} = \sqrt{\frac{8\sigma}{\rho_g R_o}}$. As a consequence, the characteristic time associated with the jet is $T_{jet} = 2R_o/v_{jet} = \sqrt{\frac{\rho_g R_o^3}{2\sigma}}$.

In our experiments, the radius of the bubble R_o is typically of the order of ~ 4 mm, the surface tension $\sigma \sim 20 \times 10^{-3}$ mN m^{-1}, the film thickness $h_o \sim 1$ μm, the density of the liquid $\rho_l \sim 1000$ kg m $^{-3}$, the density of air $\rho_g = 1.2$ kg m^{-3} and $c = 340$ m s^{-1}.

So, with these parameters, we obtain the following orders of magnitude of the three characteristic times :

$$T_{nw} = 2R_o/c \approx 23\ \mu s, \quad T_{tc} = \pi R_o \sqrt{\frac{2\rho_l h_o}{\sigma}} \approx 4ms, \quad T_{jet} = \sqrt{\frac{\rho_g R_o^3}{\sigma}} \approx 1ms.$$

This dimensional analysis shows that T_{nw} is two orders of magnitude smaller than T_{exp} underlying that Whitham analysis does not apply here. The reason is simple : the characteristic speed of the bubble opening (Taylor-Culick velocity) is not high compared to the speed of sound and thus there is no initial pressure discontinuity as considered by Whitham but rather a progressive opening of the bubble. We shall see in the next section that the spatial waveform also does not match with Whitham theory. However, the two other characteristic times T_{tc} and T_{jet} are compatible with the period of the emitted wave and thus the two associated phenomena remain good candidates to explain the origin of the sound.

Spherical harmonics decomposition of the signal

Fig. 4.16 shows the wavefront of the acoustical signal measured experimentally with the MEMs array (Fig. a.) and the contribution of each spherical harmonic to the energy of the wave (Fig. B.) obtained after spherical harmonic decomposition of the signal. A classical result in acoustics (see e.g. Morse and Ingard [185]) is that sound resulting from forces applied on fluids are dipolar, while sound resulting from incompressible mass flows are quadripolar. Finally sound produced by an initial pressure discontinuity around a sphere is expected to be monopolar (see Whitham [184]). Fig. 4.16 shows clearly that the sound produced by the bubble popping is essentially dipolar. This suggests that (i) Whitham theory does not apply, (ii) the sound is not produced by the air jet and (iii) that consequently the sound is essentially produced by the progressive reopening the bubble and associated interfacial forces. If this hypothesis is correct, the period of the emitted wave should simply be the bubble bursting time, what we indeed observe experimentally.

4.4.3 Hydrodynamics of the bubble opening

We wanted to further analyze the hydrodynamics of bubble bursting. The previous dimensional analysis suggests that different hydrodynamic regimes may occur depending on the ratio $T_{jet}/T_{tc} \sim \sqrt{\frac{\rho_g}{\rho_l}\frac{R_o}{h_o}}$. These regimes have been explored numerically with Gerris, a finite volume

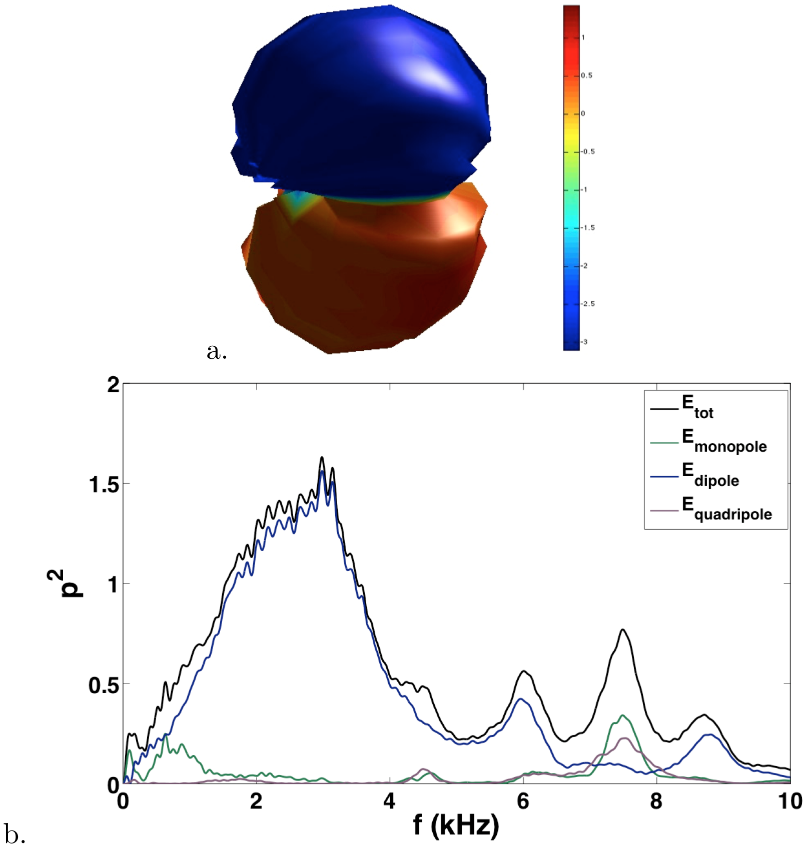

FIGURE 4.16: a.Wavefront of the acoustic wave. b. Spherical harmonic decomposition. Energy (square of the measure pressure field) associated with each harmonic as a function of the frequency (in kHz)

software with VOF (Volume of Fluid) interface tracking method, and quad-tree square spatial discretization allowing mesh refinement. The simulations are incompressible and axisymmetric. Thus, neither the emission of the acoustic wave nor the azimuthal instability of the bubble rim leading to droplet atomization can be observed.

Results obtained in the different regimes are shown on Fig. 4.17. When $T_{jet}/T_{tc} << 1$ (corresponding to small bubbles), the bubble evolution is mainly driven by the air jet that empties the bubble. So the evolution of the bubble is mainly radial and leads to the production of an air jet. When $T_{jet}/T_{tc} >> 1$ the bubble opens due to the retraction of the liquid film at Taylor-Culick velocity and the bubble radius remains essentially constant. Finally, in the intermediate regime the bubble interface evolves both *radially* due to the jet of air that empties the bubble and *tangentially* according to polar angle θ due to the retraction of the liquid film at Taylor-Culick speed.

Previous dimensional analysis has shown that our experiments are located in the intermediate regime $T_{jet} \sim T_{TC}$ and thus the evolution of the bubble rim is expected to be both radial and tangential. This is indeed observed on Fig. 4.18.

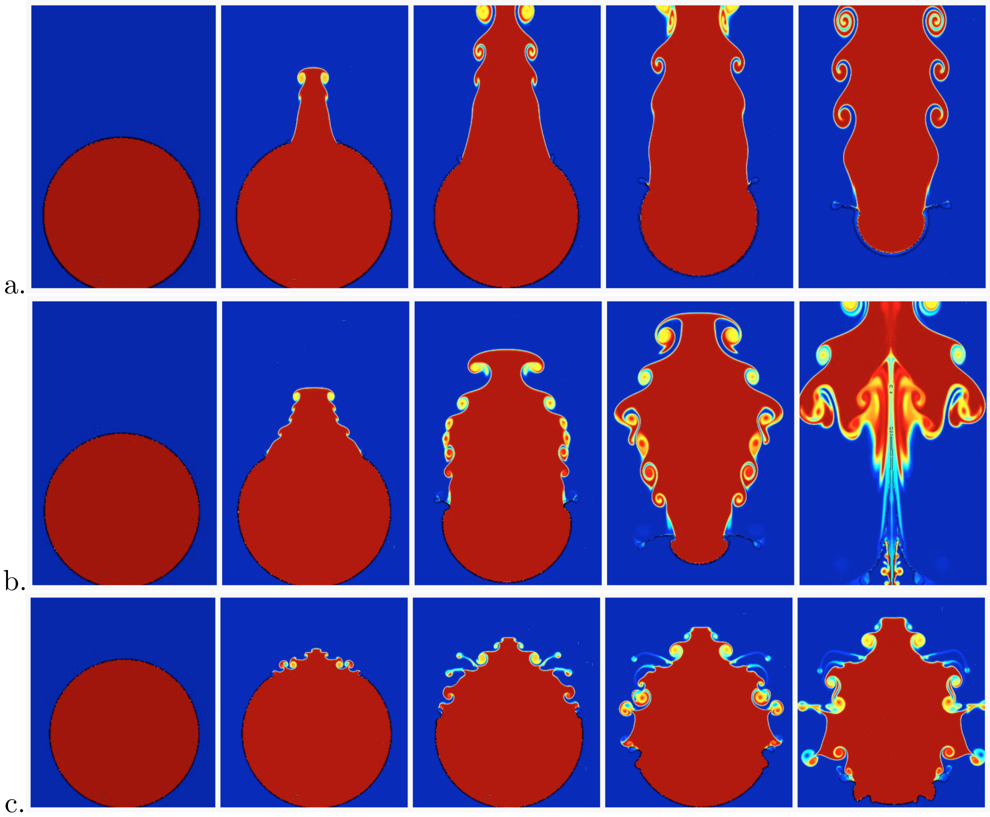

FIGURE 4.17: Reopening of a soap bubbles in three regime : a. $T_{jet}/T_{tc} << 1$. b. $T_{jet}/T_{tc} \approx 1$. c.$T_{jet}/T_{tc} >> 1$

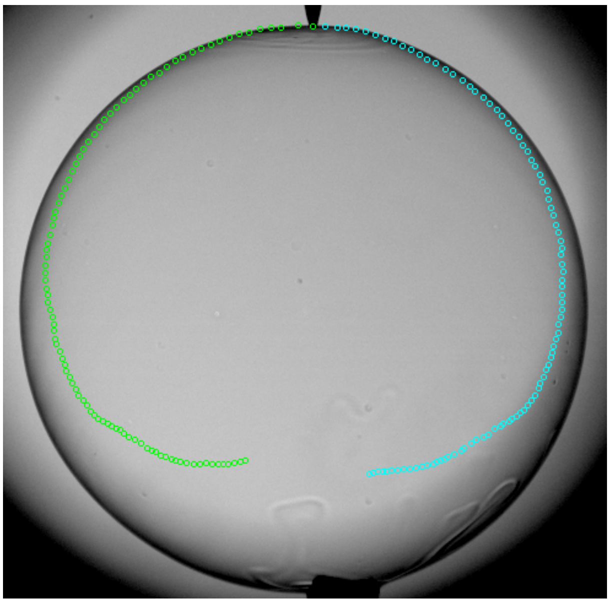

FIGURE 4.18: Opening of a bubble of radius 4 mm forced by a needle (before drainage takes place). Green and blue points correspond to the successive locations of the rim.

Simple model

In this regime, the evolution of the bubble is not solely described by the retraction of the liquid film at Taylor and Culik speed : the radial evolution of the bubble due to the air jet must be considered and we will see that both phenomena are strongly coupled. We developed a simple analytical model that allows to predict qualitatively the evolution of the bubble in this case.

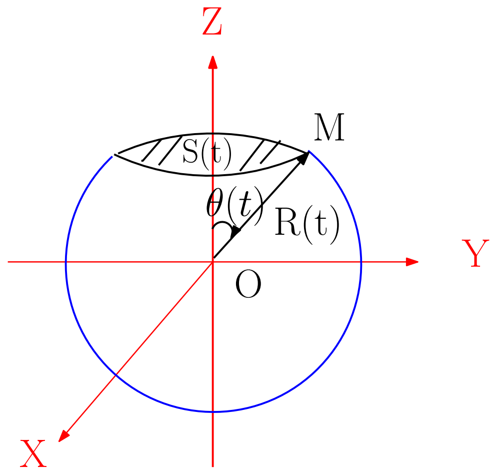

FIGURE 4.19: Scheme of the bubble to study its opening.

Let's $\theta(t)$ and $R(t)$ be the spherical coordinates of a point M located on the bubble rim and O be the center of the frame of reference $\mathcal{R}$ (see Fig. 4.19). The speed of the bubble rim is $\overrightarrow{u_M}(t) = \frac{d_{\mathcal{R}}\overrightarrow{OM}}{dt} = u_r\vec{e_r} + u_\theta\vec{e_\theta} = \frac{dR(t)}{dt}\vec{e_r} + R(t)\frac{d\theta}{dt}\vec{e_\theta}$, with u_r and u_θ the radial and tangential speed respectively. It we suppose that the retraction of the liquid film still occurs at Taylor-Culick velocity (although the thickness of the liquid film $h(t)$ is evolving), we have $u_\theta = \sqrt{\frac{2\sigma}{\rho_l h(t)}}$ with σ the surface tension and ρ_l the liquid density. Since $u_\theta = R(t)\frac{d\theta}{dt}$ we obtain the differential equation for θ angle :

$$\frac{d\theta}{dt} = \frac{1}{R(t)}\sqrt{\frac{2\sigma}{\rho_l h(t)}} \tag{4.1}$$

Then, we need to predict the evolution of the radius $R(t)$. It we suppose that the bubble is emptied by the air jet flowing at a speed v_{jet}, a simple mass balance gives :

$$\frac{dV(t)}{dt} = \frac{d}{dt}\left(\frac{4}{3}\pi R^3(t)\right) = 4\pi R^2(t)\frac{dR(t)}{dt} = -v_{jet}S(t)$$

with S the open section of the bubble. Then, the jet velocity v_{jet} can be estimated from the overpressure induced by Laplace law inside the bubble $\Delta p = \frac{4\sigma}{R(t)}$ and Bernoulli's formula : $v_{jet} = \sqrt{\frac{2\Delta p}{\rho_g}} = \sqrt{\frac{8\sigma}{\rho_g R(t)}}$, with ρ_g the gas density (here as a first approximation, the steady Bernoulli formulation is considered). Finally, we have to estimate the opened section S(t). Geometrical considerations give : $S(t) = \pi R^2(t)\sin^2\theta(t)$. If we combine these equations, we get :

$$\frac{dR(t)}{dt} = -\sqrt{\frac{\sigma}{2\rho_a R(t)}}\sin^2\theta(t) \tag{4.2}$$

Now, we need to determine the evolution of the thickness of the liquid film $h(t)$ as a function of the radius $R(t)$. Mass balance for the liquid contained in the film gives (if we suppose that the film is thin $h(t) \ll R(t)$) :

$$R^2(t)\sin\theta d\theta d\varphi\, h(t) = R_o^2\sin\theta d\theta d\varphi\, h_o \Rightarrow h(t) = h_o\frac{R_o^2}{R(t)^2} \tag{4.3}$$

An interesting point is that since $h(t) \propto R(t)^{-2}$, the angular velocity $d\theta/dt$ is constant :

$$\frac{d\theta}{dt} = \sqrt{\frac{2\sigma}{\rho_l h_o R_o^2}} = \omega_o \tag{4.4}$$

Thus only one first-order nonlinear differential equation needs to be solved to determine the evolution of the rim :

$$\boxed{\frac{dR(t)}{dt} = -K\sqrt{\frac{1}{R(t)}}\sin^2(\omega_o t)} \tag{4.5}$$

with $K = \sqrt{\frac{\sigma}{2\rho_a}}$ and the initial condition $R(t=0) = R_o$. This equation has the analytical solution :

$$R(t) = \left[R_o^{3/2} - \frac{3}{4}Kt + \frac{3}{8}\frac{K}{\omega_o}\sin(2\omega_o t)\right]^{2/3}$$

Results obtained with this simple model for a bubble of initial radius $R_o = 4$ mm and wall thickness $h_o = 1\mu$m (typically in the range of our experiments) are shown on Fig. 4.20.

This model predicts a decrease in the rim velocity (see Fig. 4.20) due to (i) the decrease in the radius $R(t)$ and (ii) the increase in the film thickness $h(t)$ resulting from the radial evolution of the bubble (also observed numerically on Fig. 4.17 a. and b. when the radial evolution of the bubble is significant). The decrease in the rim speed is indeed observed experimentally and the magnitude of the evolution is coherent with our prediction (see Fig. 4.21).

Of course this model is extremely simplified since Taylor-Culick formula might not apply when the velocity of the liquid film is not constant and unsteady effects might play a role in Bernoulli formulation. The examination of the validity of these different approximations along with more precise comparison with the experiments is still underway.

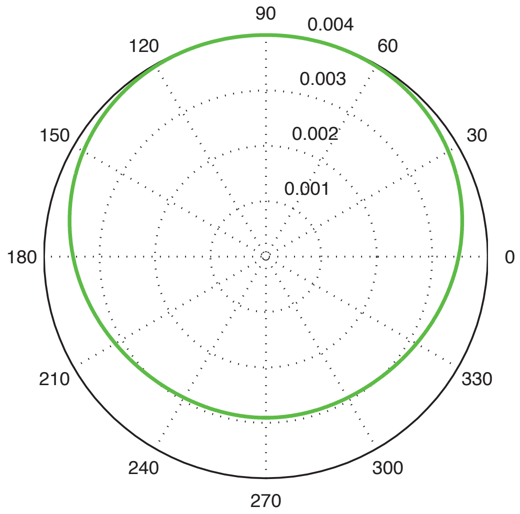

a.

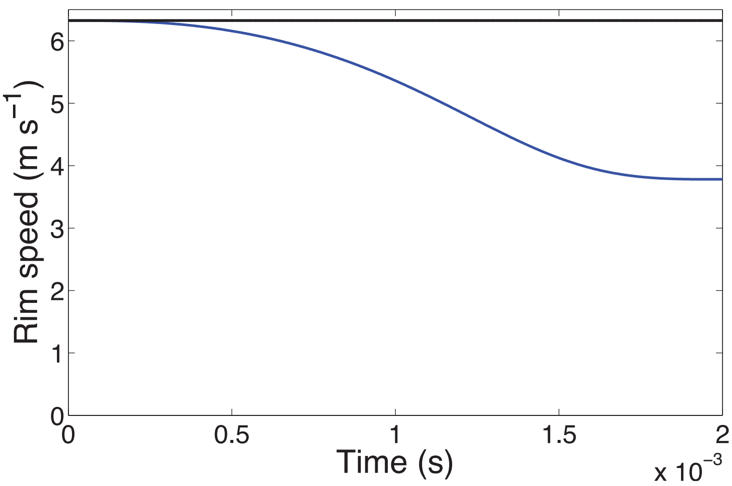

b.

FIGURE 4.20: Bubble evolution predicted by Eq. 4.5 and 4.4. a. Black line : initial shape of the bubble. Green line : Evolution of the bubble rim. b. Black line : Taylor Culick velocity. Blue line : Velocity of the bubble rim predicted by Eq. 4.5 and 4.4.

4.4.4 Acoustic wave produced by the bubble bursting

The final step is to predict the signal emitted by the progressive reopening of the bubble. Following Morse and Ingard [185], the pressure wave can be estimated from the following formula (in the Fourier space)

$$p_a(\vec{r},\omega) = \iiint_{V_o} -div_o\left(\vec{F_\omega}(\vec{r_o})\right)\mathcal{G}_\omega(\vec{r},\vec{r_o})dV_o$$

where $\vec{F_\omega}$ is the Fourier Transform of the force applied on the fluid (here the Laplace pressure exerted on the air), $\mathcal{G}(\vec{r},\vec{r_o})$ is the Green function associated with Helmholtz equation in 3D

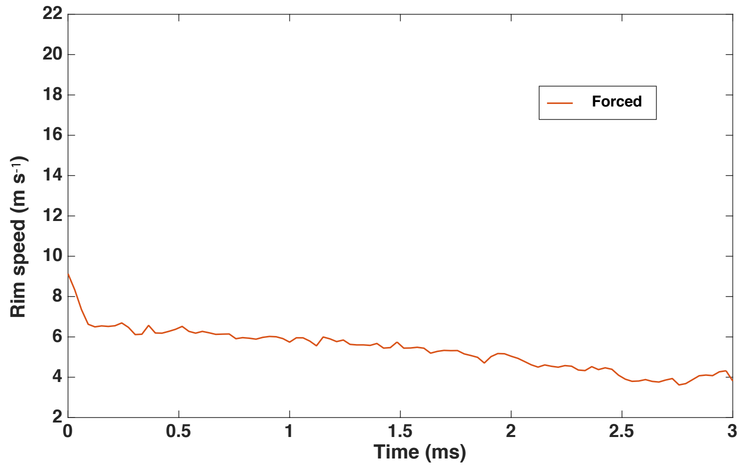

FIGURE 4.21: Rim speed of a bubble of 4 mm radius measured experimentally.

and propagating the signal from $\vec{r_o}$ to $\vec{r}$, and V_o is a reference volume surrounding the sound source. As long as no source crosses the surface S_o surrounding V_o, $\vec{F_\omega} = 0$ on S_o and thus :

$$\iiint_{V_o} div_o \left(\vec{F_\omega}(\vec{r_o}) \mathcal{G}(\vec{r}, \vec{r_o}) \right) dV_o = \iint_{S_o} \mathcal{G}(\vec{r}, \vec{r_o}) \vec{F_\omega}(\vec{r_o}).\vec{n_o} dS_o = 0$$

with $\vec{n_o}$ the unit vector normal to surface S_o. As a consequence, we have :

$$p_a(\vec{r}) = \iiint_{V_o} \vec{F_\omega}(\vec{r_o}).\vec{\nabla}_o \mathcal{G}(\vec{r}, \vec{r_o}) dV_o. \tag{4.6}$$

The force resulting from Laplace pressure is $\vec{F_\omega}(\vec{r_o}) = \frac{-4\sigma}{R} h_\omega(\theta_o) \delta(\vec{r_o}, R\vec{e_{r_o}}) \vec{e_{r_o}}$ with ($\vec{e_{r_o}}$, $\vec{e_{\theta_o}}$, $\vec{e_{z_o}}$) the unit vectors in spherical coodinates, (r_o, θ_o, z_o) the spherical coordinates and $h_\omega(\theta_o)$ is a function that describes the spatial evolution of the bubble in the Fourier space :

$$h_\omega = \delta(\omega) - e^{-i\omega\tau} \left(\frac{1}{i\omega} + \frac{1}{2} \delta\omega \right)$$

with $\tau = \frac{R}{V_{tc}} \theta_o$ if we neglect the radial evolution of the bubble.

Results obtained with this formula are shown on Fig. 4.22. Qualitative agreement of both the spatial and temporal waveform of the signal is achieved. Quantitative comparison between theory and experiments is still underway.

4.5 Conclusion

In this chapter, we studied the dynamics and spatio-temporal distribution of plug ruptures in a network mimicking the lung, the hydrodynamics of the the rupture last moments and finally the sound resulting from a liquid film rupture when there is a pressure difference on both sides of

a. 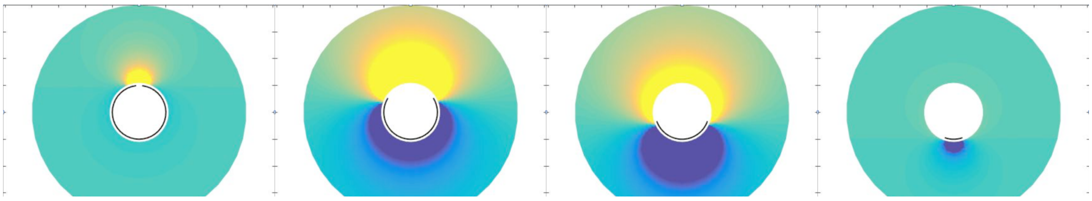

FIGURE 4.22: a. Wavefield emitted by the bubble opening predicted by equation 4.6. The white region at the center corresponds to the bubble location. The black line materializes the liquid film b. Temporal signal emitted by the bubble

the interface. To reach quantitative and realistic models of lungs sound produced in pathological conditions, the next steps will be (i) to characterize the acoustical signature of a liquid plug rupture, (ii) to develop propagators of these sounds in the human body and (iii) to investigate more realistic tree geometries. These considerations are developed in the project section.

Chapitre 5

Project

Our project is to keep taking advantage of the leading edge environment at IEMN to solve very challenging scientific issues that either require or will help creating some advanced microsystems. We also feel that research at the interface between acoustics and microfluidics (what is now commonly called microscale acoustofluidics) is still at its infancy and that this field offers many perspectives for interesting research. The community is growing fast [186–188] but we still are one of the only group worldwide that is not only able to develop advanced microsystems but also to address theoretical and numerical issues on both microfluidic and acoustics problems and especially their coupling. Of course, we will continue collaborating with high quality groups worldwide (Canada, Denmark, England, France, Russia, United states) with either complementary skills or common interest in solving specific issues.

As described all along this manuscript, there are mainly three types of interactions between acoustics and microfluidics : either microfluidics flow can modify the propagation of acoustic waves, or microfluidic two-phase flows can create acoustic waves, or reversely acoustics can be used to control microfluidic flow. I plan to keep working on all these aspects in the next 10 years. I also wish to achieve in the near future some scientific advances that will really help addressing some practical issues. So our two main research axes will be :
(i) To develop a synthetic and a virtual lung that will help understanding and predicting flows and associated breathing sounds in pathological conditions. This might not only provide some new tools for physicians to improve the diagnosis of pulmonary obstructive diseases with new modern stethoscopes but also to find new efficient ways of treating these diseases.
(ii) To develop on-chip, 3D selective acoustical tweezers and high precision hydrodynamic vortices generators based on swirling SAWs (a) to explore cells mechanotransduction, (b) to study the ability of these tweezers to assemble microsystems in aqueous phase and (c) to improve our understanding of hydrodynamic vortices interactions.

Of course, we will also keep exploring some new paths, such as the potential of armored bubbles for medical imaging and drug delivery or try to solve some fundamental problems such as the multiple scattering of acoustic waves by "concentrated" suspensions of bubbles. Because, sometimes that is also where you expect them less, that the most interesting applications appear...

5.1 Synthetic and virtual lung for the study of flows and associated breathing sounds in pathological conditions

5.1.1 Introduction

Context

The main function of the human lung is to ensure efficient gas exchanges between the atmosphere and the bloodstream. For this purpose, nature has adopted a binary tree structure, leading to complex flows with drastically different properties in upper and distal airways and complex interactions between them. Obstructive lung diseases can dramatically alter the distribution of air inside the bronchial tree. Airways obstruction can result from a change in the airways sections or in the walls rigidity (in bronchiectasis or asthma) and/or the accumulation of mucus (in cystic fibrosis and bronchitis). When too much mucus accumulates in the bronchial tree, the mucus lining can even become unstable leading to the formation of liquid plugs and resultantly severe obstruction of the corresponding paths. Obstructed airways may reopen either naturally during the breathing cycle or when coughing or may require some clinical intervention. Airway reopening is accompanied by respiratory sounds used by physicians for the diagnosis of obstructive lung diseases with the help of a stethoscope. But a precise understanding of their link to the pathophysiology of these diseases (required to propose an accurate diagnosis along with a more personalized, targeted and efficient treatment of these pathologies) is still missing. From the standpoint of fluid mechanics, the problem of mucus-air two-phase flows in lungs and associated breathing sounds is highly complex owing to the multiplicity of length and time scales and their numerous interactions. In particular, the following issues of upmost interest need to be solved to achieve a good description of these systems : the unsteady dynamics of liquid plugs, their division and long range interaction in networks, hysteretic effects appearing when they undergo periodic motion and the acoustic wave emission associated with interface rupture. To understand the complex two-phase flows and associated breathing sounds in physiologically relevant conditions, this project aims at developing a synthetic lung reproducing precisely the geometry of both upper and distal airways and approaching its mechanical properties. Experimental studies will be accompanied by intensive numerical simulations and theoretical modeling leading to the development of a virtual lung reproducing the main features of these pathological flows. The derived knowledge will be used (i) to provide the necessary elements toward the development of new modern electronic stethoscopes optimized for the analysis of breathing sounds, (ii) to improve these diseases treatments with vibrational and acoustical therapy and (iii) to determine the optimal mechanical ventilators modes for people with obstructed airways according to their pathology.

State of the art

In the literature, a significant gap remains between medical, physiological and physical studies of obstructive pulmonary diseases. This gap is detrimental to the development of modern diagnosis, monitoring and treatments of these diseases. Most medical studies are dedicated to the understanding of biological mechanisms at the origin of obstructive lung diseases, the prevalence of risk factors and statistics on the efficiency of different treatments (see e.g. [189–191]). These studies do not provide any description of the physical mechanisms of airways clearance and only highly speculative hypotheses on the origin of breathing sounds. Physiological ex-vivo observations of obstructive lung diseases are prohibitively complex due to the opaque 3D and fractal nature of the bronchial tree. The data are most often limited to measurements performed at the root of the tree or statistical analysis of breathing sounds (see e.g. [192, 193]). From a physical perspective, pulmonary obstructive diseases have motivated many studies on the motion of gas / liquid flows into straight and bifurcating channels [194–199]. However, nearly all the model experiments and simulations have considered the simplest situations, either studying the motion of a single liquid plug or concentrating on the flow through a single bifurcation, or both. This reduces the number of independent degrees of freedom and, by the same token, the range of behaviors those models can explore. These studies therefore cannot account for complex interactions that involve many levels in the tree, which play a fundamental role on airways clearance (see e.g. Alencar et al. [200]). These interactions have been investigated in simplified geometries in recent publications of our group [137, 138]. This work enlightens the fundamental role played by the geometry and the forcing conditions on the spatio-temporal distribution of airways reopening, and thus emphasizes the need to treat more physiologically relevant structures and address the complexity of breathing cycles.

5.1.2 Project

The primary aim of this project is to bridge the gap between physicians and physicists on the problem of lung flows in pathological conditions in order to bring physical answers to medical issues. In particular, we want to address 3 fundamental questions : (i) What is the physical origin of crackles sounds and what information on the physiopathology of associated diseases can be learnt from the precise analysis of the sounds recorded by a stethoscope ? (ii) How do vibrational therapy (mechanical vibrations applied on the chest around 10 Hz) and acoustical therapy (lung flute) help mucus clearance and how can they be optimized for the treatment of patients ? (iii) What are the optimal breathing modes of mechanical ventilator for people with bronchial congestions ? For this purpose this project targets two major objectives : (i) Developing synthetic lungs replicating precisely the geometry of upper and distal airways to study two-phase flows and associated sounds in physiologically relevant conditions. (ii) Developing a virtual lung based on theoretical and numerical models predicting mucus flows in the bronchial tree. These objectives require the resolution of complex underlying issues in fluid mechanics : the unsteady dynamics of liquid plugs, their division and long range interaction in networks, hysteretic effects appearing when they undergo periodic motion and the acoustic wave emission associated with interface rupture. The following sections describe them in more details.

Study of avalanches of plug ruptures in a synthetic network reproducing the lung geometry

The first objective of this project is to study the reopening of airways initially obstructed by liquid plugs in physiologically relevant conditions. For this purpose, these two-phase flows will be studied in artificial networks reproducing precisely the geometry of pig and human lungs.

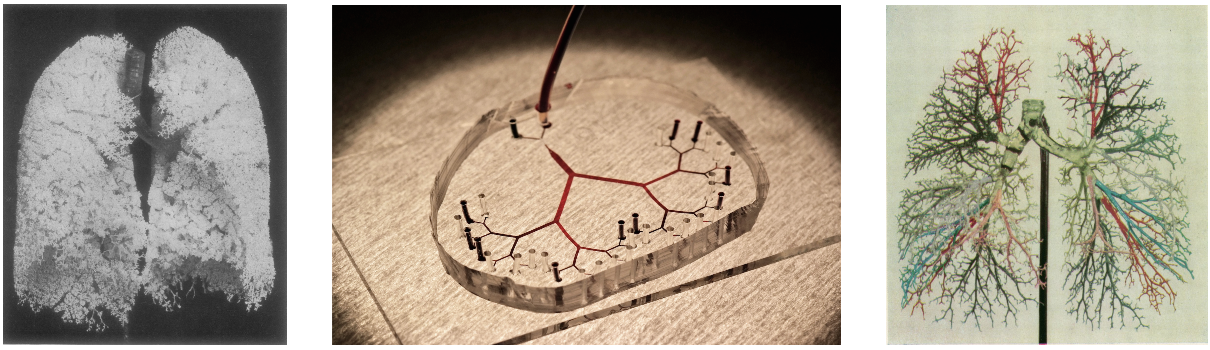

FIGURE 5.1: Left and Right : Bronchopulmonary cast of a human lung (respectively before and after pruning) obtained by resin injection inside lung airways (Source : [16]). Center : Synthetic network in PDMS used of the study of interactions between branches in the dynamics of liquid plugs in hierarchical networks. (Source : [137]

Two methods will be considered to design realistic synthetic lungs : In the first method, positive resin cast of post-mortem lung will be obtained by resin injection in the lung [201] (see Fig. 1 left and right) and tissues dissolution with sodium hydroxide. Then, the negative compliant hollow cast will be obtained by extending the method proposed by Phalen et al. [202**?**] with the use of dissolvable resins. With this method, we plan to design synthetic lung reproducing typically 8 to 10 generations at a time. The second method relies on high-resolution 3D stereolithographic printer combined with the data of the Visible Human Project to reconstruct human lung airways (see e.g. [203]. At first, these synthetic lungs will be used to characterize realistic flow properties in normal breathing conditions in the different parts of the lung by using Particle Image Velocimetry (PIV) measurements. Then, trains of liquid plugs will be injected in different parts of the network to study their dynamics and compare their behavior in intermediate and distal airways where characteristic dimensionless numbers are extremely different. In particular, we will characterize the spatio-temporal distribution of plug ruptures and analyze the complex interactions between the branches of this synthetic tree with statistical methods. The role of the forcing conditions will also be investigated in details by applying simple and then realistic forcing conditions. This work will be supported by the models developed in the second part of this project.

Development of a virtual lung modeling the dynamics of liquid plugs in complex networks

The second objective of this project is to develop and validate step by step a simplified physical model reproducing liquid plugs two-phase flows in the lung geometry. To ensure a thorough understanding of the studied phenomena, each theoretical and numerical ingredient of our virtual lung will be validated by comparison with model experiments and direct numerical simulations. Then the global model will be validated by comparison with the experimental database obtained with our synthetic lung and physiological data available in the literature.

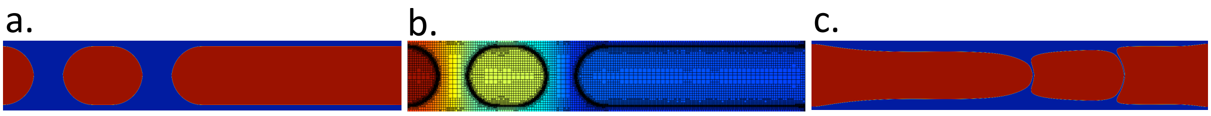

FIGURE 5.2: Figure 2 : Numerical axisymmetric simulations of the dynamics of two liquid plugs obstructing a cylindrical channel. These simulations were performed with Gerris open source software. A. Initial state with two liquid plugs in blue and air bubbles in red. B. Pressure field (colours) and view of the mesh. C. Evolution of the system just before the plugs rupture

.

In ref. [137], our team has developed a 1D simplified model reproducing quantitatively the airways reopening through cascade of plug ruptures in a straight channel. In this project we want to extend this model to complex physiologically relevant networks, realistic forcing conditions and realistic mucus rheological properties. For this purpose, the following studies will be conducted : Study 1 : Plugs dynamics and division at bifurcations. When liquid plugs move in a network, they regularly reach some bifurcations where they divide depending on the geometry of the daughter branches and the pressure distribution. To determine the division laws and the pressure required to cross a bifurcation, we will perform experiments on bifurcating microfluidic channels and direct simulations with the octree-based Volume-Of-Fluid numerical code Gerris. Then these laws will be incorporated into our simplified model. Study 2 : Extension of the straight channel 1D model to networks. Once the division laws established, the extension of straight channel model to networks requires the modeling of the multilevel interactions between the tree branches. For this purpose, the pressure at each node of the tree must be determined through the resolution of an inverse problem. Then an event-driven code will be developed to treat the plugs evolution in the network, the event being the division of plugs at bifurcations. Study 3 : Study of the role of complex cycles on the plugs dynamics. According to preliminary studies by our group, hysteretic effects appear when plugs are driven by cyclic conditions due to plugs interactions through their trailing film. This effect will be studied experimentally on model experiments and numerically with Gerris flow software, which enables unsteady forcing. Study 4 : Influence of the rheological properties of mucus plugs on their dynamics. Finally, mucus has non-Newtonian properties that might play a fundamental role on the plugs dynamics. We will investigate this effect experimentally by using liquids with properties similar to the mucus and then numerically with Gerris by implementing the required non-Newtonian laws into the code.

Study of medical issues based on our synthetic and virtual lungs

This part of the project will be conducted in collaboration with the Division of Respiratory Diseases from Lille ?s Regional Hospital Center. In this project we target three medical issues. First medical issue : Investigation of crackles sounds associated with airways reopening and determination of the missing link between the sounds recorded with stethoscopes and the physiopathology of obstructive lung diseases. For this purpose, the sound produced by the rupture events will be recorded on the synthetic lung with a laser vibrometer, analyzed, and correlated with the plugs dynamics registered with the high-speed camera. This acoustic signature will then be compared to crackles sounds registered on real lungs in order to provide, for the first time, a clear explanation of the origin of these sounds. Second medical issue : Investigation the role of vibrations (applied with mechanical vibrators on the chest of patients or with the use of a lung flute) on mucus clearance. Indeed, several studies have proved the efficiency of vibrational therapy to help mucus clearance. Nevertheless, there is up to date no clear physical understanding of the role played by the vibrations. Our hypothesis is that the vibrations might influence the mucus properties due to their non-Newtonian properties. To study it, the synthetic lung initially obstructed with non-Newtonian liquid plugs will be vibrated with a shaker or with a lung flute during breathing cycles and the plugs dynamics will be carefully analyzed to determine the role of vibrations on mucus clearance. Then we will determine the optimal signal required for an efficient treatment. Third medical issue : Determination of the optimal breathing cycles enforced by a mechanical ventilator to improve airways clearance according to the nature of the airways obstruction. For this purpose we will use our virtual lung numerical model along with optimization methods to determine the best strategies. These strategies will then be tested on our synthetic lung.

5.1.3 Conclusion

Obstructive lung diseases affect more than 350 millions people in the world. They are extremely incapacitating and their treatment requires frequent medical clinic visits and hospitalizations. From an applied perspective this work might extend significantly our understanding of these

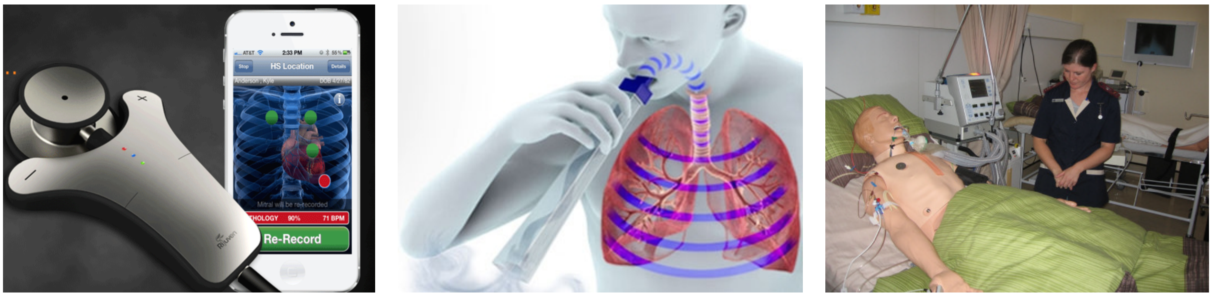

FIGURE 5.3: Left : Stethophone CardioSleeve developed by the American company Riiuven to record, display and analyze heart sounds. Center : Lung Flute producing low frequency acoustic waves to help mucus clearance for patients with obstructive lung disease. Right : Mechanical ventilator for patients with acute distress respiratory syndrome.

diseases, and in the future help enhancing their diagnosis with the precise analysis of respiratory sounds and improving their treatment with vibrational therapy or in emergency situations with mechanical ventilator.

Moreover, the potential of the experimental, theoretical and numerical tools developed in this work far exceeds the scope of this project. In particular (i) the development of synthetic compliant lungs reproducing precisely the geometry of the lung might be useful for many other studies of pulmonary flows and (ii) the numerical and theoretical tools describing plugs flows in networks have applications in other fields such as microfluidics, oil and water extraction from porous media, imbibition of paper, ...

5.2 Swirling SAWs for on-chip 3D selective contactless acoustical tweezers and twisters

5.2.1 Context

Swirling SAWs allow for the first time on-chip 3D contactless manipulations of particles and synthesis of hydrodynamic vortices with controlled topology. These two basic tools may lead to a paradigm shift in the study of cells mechanotransduction, microsystems assembly or vortex dynamics.

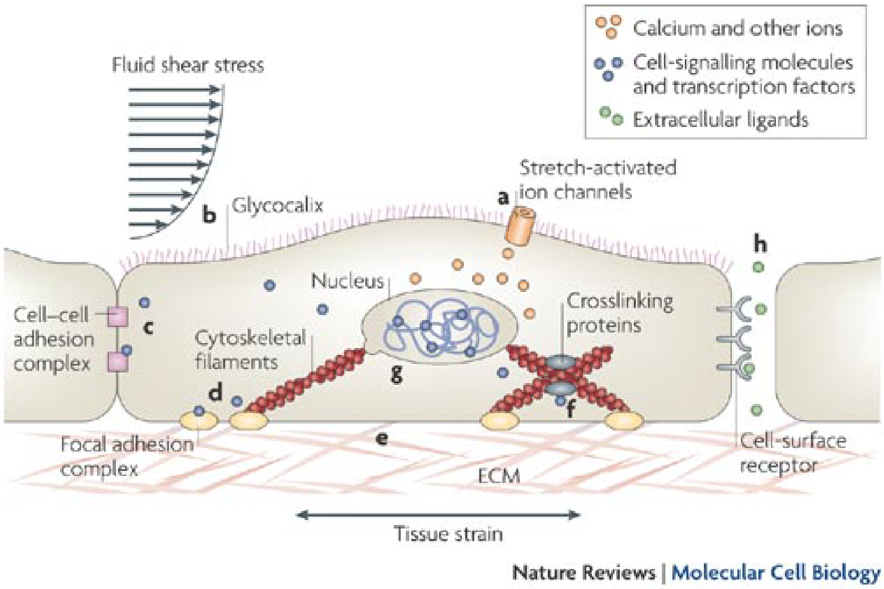

FIGURE 5.4: Sketch illustrating different mechanosensors at the surface of a representative cell. (Source : [204])

Cellular *mechanotransduction* [204–207] is any of the various mechanisms leading to conversion of external mechanical stimuli to changes in intracellular biochemistry. These processes are critical to control cell growth, migration, differentiation and apoptosis during organogenesis, wound repair or cancer growth. But they are also central for a number of senses including touch, balance and hearing. Analysis of how cells sense and respond to mechanical stresses is so far greatly limited by the availability of techniques that can apply controlled mechanical forces to living cells while simultaneously measuring changes in cells and molecular distortion, as well as alterations of intracellular biochemistry. Labs-on- chips based on swirling SAWs might provide the missing platform to manipulate cells, apply control stresses at their surface, monitor their deformation with a microscope and study their electromechanical activity with integrated sensors. Such platform might lead to tremendous progress in this field.

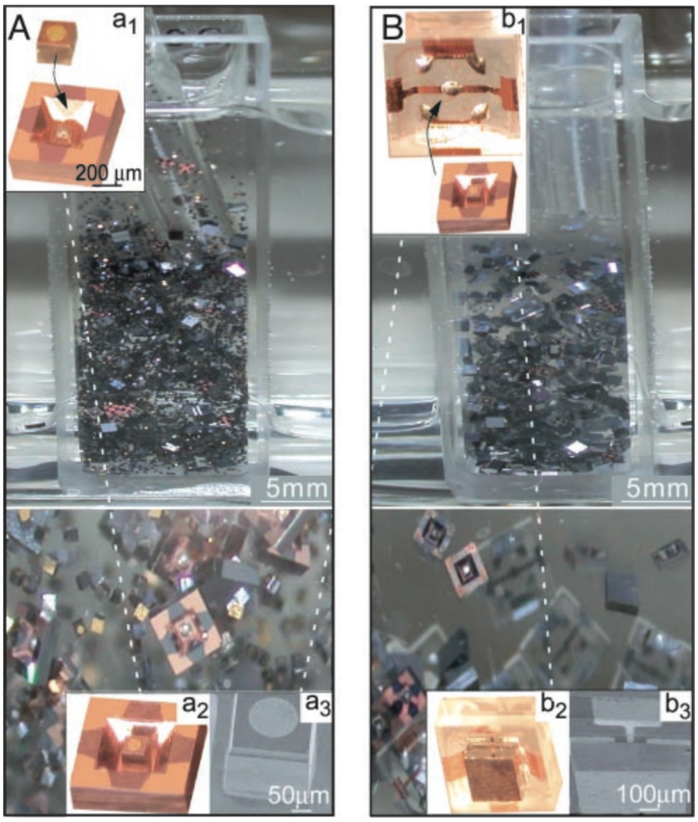

FIGURE 5.5: Experimental realization of LED chips assembled and packages with self-assembly method. (Source : [208])

A second issue which could be adressed with these tweezers is the cost-effective *assembly of microsystems*. As components become smaller, following the trend in miniaturization, conventional robotic methods and assembly lines fail because of the difficulty in building machines that can economically manipulate components in three dimensions that are only micrometers in size [209, 210]. The challenges for such assembly is not only to move and position the different pieces but also to grasp them without damage. Some new technics such as fluidic self-assembly [208, 211–216] or assembly by MEMS [217] are under investigation to overcome these shortcomings. Nevertheless, while self-assembly is cheaper than conventional technics, and might be of primary interest in some cases, this technic is also less versatile than conventional technics and thus remains limited to specific operations. Labs-on-chips based on swirling SAWs would enable the contactless manipulation of microsystems with a precision that mainly depends on the frequency used, but also the monitoring of the assembly with different integrated sensors. Since the displacement of the acoustical trap is achieved by inverse filter method, no moving part is required to perform these operations, hence significantly reducing the costs.

These first examples use the ability of acoustical vortices to manipulate objects. Another possibility is to use acoustical vortices to synthesize hydrodynamic vortices with a controlled topology

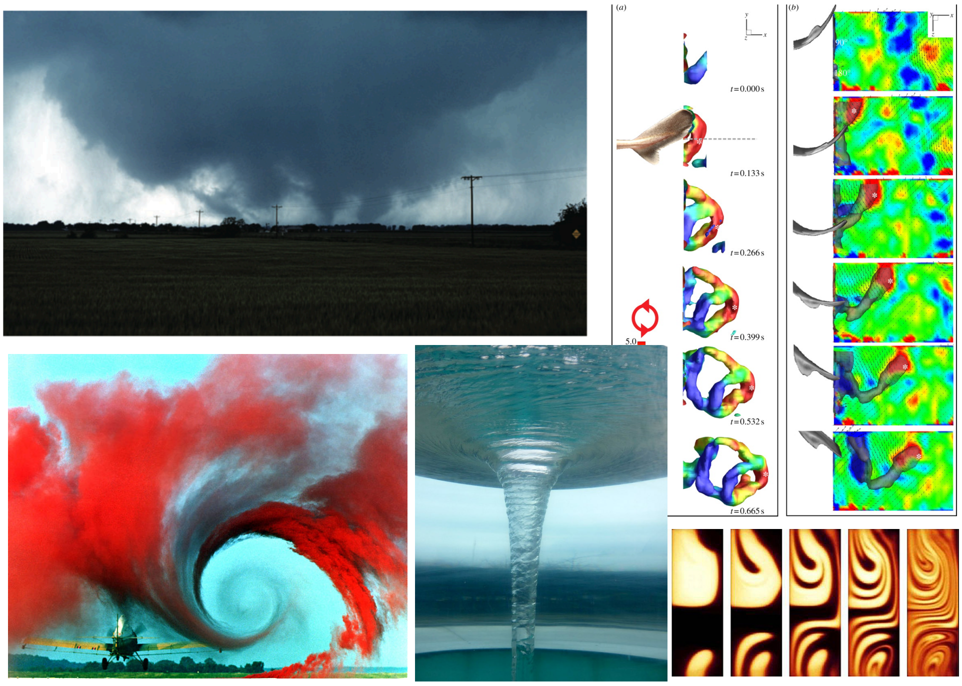

FIGURE 5.6: Stack of images showing different natural and engineered systems where hydrodynamics vortex play a fundamental role (Sources : [218–220])

that mainly relies on the one of their acoustical counterpart. Vortices are ubiquitous in fluid mechanics, both in natural and engineered system. They are involved in fish, microorganism and bird locomotion [221–224], tornadoes [220] and cyclones dynamics [225], turbulent flows [219, 226–228], fluid mixing [100], lift forces that allow plane to flight [229],... to name but a few. In particular, low Reynolds flows are intrinsically vortical. The control of vorticity is thus the cornerstone of mixing [218] at micrometric scales or locomotion of micro-swimmers. From a more fundamental perspective, understanding vortex dynamics and interactions is essential to reach a good comprehension of complex flow such as turbulent flows. Nevertheless, there is up to date no experimental system allowing the synthesis of 3D hydrodynamic vortices filaments with controlled topology. Thus acoustical twisters might open new perspectives to study the dynamics, stability and interactions of hydrodynamics vortices.

Before delving into these tremendous applications, a few challenges need to be addressed.

5.2.2 The next challenges

Radiation pressure vs streaming

The first challenge it the comparison of radiation forces and streaming forces applied on particles. Indeed, we have up to now studied separately the acoustic streaming and radiation pressure induced by acoustical vortices. However, these two phenomena can interact since streaming flows can also induce forces on particles and prevent particles trapping at the core of the acoustical vortex. For standing waves, the comparison between these two forces has been addressed in a nice piece of work by Bruus and coworkers [230, 231]. We need to perform an equivalent dimensional and quantitative analysis to determine the frequencies, vortex topologies and cavity sizes where trapping is possible. For this purpose, we already developed a code that is able to simulate the acoustic streaming and radiation pressure induced by acoustical vortices in a cavity and experiments will be performed with our system with different particles sizes.

Miniaturization

The system that we developed has been optimized to work at 12 MHz, which corresponds to an acoustical wavelength in water of about 125 microns. While it is not required that an object has the same size as the wavelength to be trapped, the manipulation is enhanced for larger particles. One reason is that the traps that we conceive with our systems are not perfect, partly due to spurious reflections at the walls of the fluidic cavity (even if PDMS is an excellent absorber) or other experimental artifacts. Thus, small particles can be trapped in local minima instead of the center of the acoustical vortex. Since, cells are typically of the orders of 10 microns, it would be interesting to increase the working frequency to properly manipulate these objects. If we did not consider these higher frequencies in AWESOM ANR project, it is mainly due the exponential increase of programmable electronics costs as a function of the driving frequency, which is hardly compatible with the decrease of ANR budgets. Moreover, the experiments we performed in the project are scalable and we did not need higher frequencies to prove the concepts. Nevertheless the proper manipulation of cells would require such frequency shift. The same problem arises if we want to work in microfluidics or even nanofluidics channels. Indeed, micro channels typically range from 10 microns to 100 microns and wavelength comparable to the channel depth would also lead to spurious effects (existence of standing waves).

Such costs increase could be envisioned for confidential fundamental study, but the mass development of acoustical tweezers would require a paradigm shift to overcome this limitation. While high frequency programmable electronics are expensive, the production of IDTs with soft lithography techniques weakly depends on the complexity of the design. With appropriate design, there is not doubt that it is possible to generate swirling SAWs at the surface of piezoelectric substrate with only the requirement of a single function generator and amplifier, dramatically reducing the cost of the system. Of course, this cost reduction is at the price of the flexibility. Indeed, inverse filter allows to generate a prescribed wavefield in the fluidic chamber. Once this wavefield optimized, the same wavefield can be reproduced with appropriate IDTs design. But the inverse filter technique also allows to modify and displace this wavefield e.g. to move particles without the requirements of robotic displacement of the tweezer. Nevertheless, we can argue that most advanced microscopes already have a displacement system and thus that they could be used to move the sample instead of moving the tweezer. So depending on the application, both systems are interesting and we will thus investigate both solutions in the future.

Advanced manipulation : multiple vortices and rotation handling

To perform advanced tasks, it is necessary (i) to be able to independently and simultaneously handle several objects and (ii) to master both their rotation and translation. To address the first issue, the basic idea is to superpose several localized acoustical vortices at different locations. While the principle might appear simple, acoustical vortices will interact during their propagation and it is necessary to understand these interactions in the specific case of acoustical vortices generated by swirling SAWs. Concerning the second issue, the rotation of particles enlightened by a Bessel beam might result from both radiation pressure and acoustic streaming. Indeed, acoustic streaming is in essence a vortical flow, which will exert shear on particles and thus induce their rotation. In the same way, radiation pressure will exert a torque on particles leading to their rotation. It is necessary to quantify these two effects and identify the resulting dynamics of particles that will not only rely on the properties of the incident field, but also on the one of the particles (size, acoustical contrast, shape, ...).

5.2.3 Conclusion

There are numerous theoretical, numerical and experimental challenges to address before achieving real mastering of on-chip 3D particles manipulation and control of flow structures with swirling SAWs. Nevertheless, each of them is of primary scientific interest and if we succeed to overcome them, we will obtain a system that might deeply modify our way of manipulating cells, assembling microsystems, or studying mechanotransduction and vortex interactions...

Bibliographie

[1] F. Zoueshtiagh, M. Baudoin, and D. Guerrin. Capillary tube wetting induced by particles : toward armoured bubbles tailoring. *Soft Matter*, 10(47) :9403–9412, 2014.

[2] R.T. Beyer. *Nonlinear acoustics*. Acoustical Society of America through the American Institute of Physics, 1974.

[3] N. Riley. Steady streaming. *Ann. Rev. Fluid Mech.*, 33 :43–65, 2001.

[4] M.F. Hamilton. Acoustic streaming generated by standing waves in two-dimensional channels of arbitratry width. *J. Acoust. Soc. Am.*, 113(1) :153–160, 2003.

[5] H. Schlichting. Berechnung ebener periodischer grenzschichtstromungen. *Phys. Zeitung*, 33 :327–335, 1932.

[6] L. Rayleigh. On the circuclation of air observed in Kundt's tubes, ans some allied acoustical problems. *Ph. Trans. Roy Soc. London*, 175 :1–21, 1884.

[7] C. Eckart. Vortices and streams caused by sound waves. *Phys. Rev.*, 73 :68–76, 1948.

[8] J.E. Piercy and J. Lamb. Acoustic streaming in liquids. *Proc. Roy. Soc. London. A*, 226(1164) :43–50, 1954.

[9] Masanori Sato and Toshitaka Fujii. Quantum mechanical representation of acoustic streaming and acoustic radiation pressure. *Phys. Rev. E*, 64 :026311, 2001.

[10] B.-T. Chu and R.E. Apfel. Acoustic radiation pressure produced by a beam of sound. *J. Acoust. Soc. Am.*, 72, 1982.

[11] C.P. Lee and T.G. Wang. Acoustic radiation pressure. *J. Acoust. Soc. Am.*, 94 :1099–1109, 1993.

[12] Brillouin L. *Ann. Phys. Paris 4*, 1925.

[13] R.T. Beyer. Radiation pressure, the history of a mislabeled tensor. *J. Acoust. Soc. Am.*, 63(4) :1025–1030, 1978.

[14] P. Biquard. *Rev. Acoust.*, pages 93–109, 1932.

[15] B. Issenmann, A. Nicolas, R. Wunenburger, S. Manneville, and J.-P. Delville. Deformation of acoustically transparent fluid interfaces by the acoustic radiation pressure. *EPL*, 83 :34002, 2008.

[16] B. Issenmann, R. Wunenburger, H. Chraibi, M. Gandil, and J.-P. Delville. Unsteady deformation of a free liquid surface caused by radiation pressure. *J. Fluid Mech.*, 682 :460–490, 2011.

[17] N. Bertin, H. ChraÃ¯bi, R. Wunenburger, J.-P. Delville, and E. Brasselet. Universal morphologies of fluid interfaces deformed by the radiation pressure of acoustic or electromagnetic waves. *Phys. Rev. Lett.*, 109 :244304, 2012.

[18] L. V. King. On the acoustic radiation pressure on spheres. *Phys. R. Soc. London A Mat*, 1934.

[19] K. Yosika and Y. Kawasima. Acoustic radiation pressure on bubbles and their logarithmic decrement. *Acustica*, 1955.

[20] L.P. Gorkov. On the forces acting on a small particle in an acoustic field in an ideal fluid. *Sov. Phys. Dokl.*, 1962.

[21] M. Settnes and H. Bruus. Forces acting on a small particle in an acoustical field in a viscous fluid. *Phys. Rev. E*, 85 :016327, 2012.

[22] Baresch D., J.L. Thomas, and R. Marchiano. Three-dimensional acoustic radiation force on an arbitrarily located elastic sphere. *J. Acoust. Soc. Am.*, 133(1) :25–36, 2013.

[23] S.M. Hagsater, A. Lenshof, P. Skafte-Pedersen, J.P. Kutter, R. Laurell, and H.) Bruus. Acoustic resonances in straight micro channels : Beyond the 1d-approximation. *Lab Chip*, 8 :1178–1184, 2008.

[24] P.B. Muller, M. Rossi, A.G. Marin, R. Barnkob, P. Augustsson, R. Laurell, C.J. Kahler, and H. Bruus. Ultrasound acoustophoretic motion of microparticles in three dimensions. *Phys. Rev. E*, 88 :023006, 2013.

[25] P.B. Muller and H. Bruus. Numerical study of thermoviscous effects in ultrasound-induced acoustic streaming in microchannels. *Phys. Rev. E*, page 043016, 2014.

[26] M. Anfolk, P.B. Muller, P. Augustsson, H. Bruus, and T. Laurell. Focusing of submicrometer particles and bacteria enablesd by two-dimensional acoustophoresis. *Lab Chip*, 14 :2791, 2014.

[27] A. Wixforth, C. Strobl, C. Gauer, A. Toegl, J. Scriba, and Z. Guttenberg. Acoustic manipulation of small droplets. *Anal. Bioanal. Chem.*, 379(982), 2004.

[28] A. Renaudin, P. Tabourier, V. Zang, J.C. Camart, and C. Druon. Saw nanopump for handling droplets in view of biological applications. *Sensors and Actuators B*, 113 :389–397, 2006.

[29] P. Brunet, M. Baudoin, O.B. Matar, and F. Zoueshtiagh. Droplet displacement and oscillations induced by ultrasonic surface acoustic waves : a quantitative study. *Phys. Rev. E*, 81 :036315, 2010.

[30] S. Collignon, J. Friend, and L. Yeo. Planar microfluidic drop slitting and merging. *Lab on a chip*, 15 :1942–1951, 2015.

[31] Y.A. Babetta and L. Marrone. Droplet translocation by focused surface acoustic waves. *Mocrofluid. Nanofluid.*, 13 :715–722, 2012.

[32] S. Shiokawa, Y. Matsui, and T. Ueda. Liquid streaming and droplet formation caused by leaky rayleigh waves. *IEEE Ultrasonic symposium*, 1 :643–646, 1989.

[33] S. Shiokawa, Y. Matsui, and T. Ueda. Study on SAW streaming and its application to fluid device. *Jpn. J. Appl. Phys.*, 29(Sup. 29-1) :137–139, 1990.

[34] K. Chono, N. Shimizu, Y. Matsui, J. Kondoh, and S. Shiokawa. Devlopment of novel atomization system based on saw streaming. *JapÂ· J. Appl. Phys*, 43(5B) :2987–2991, 2004.

[35] A. Qi, L.Y. Yeo, and J.R. Driend. Interfacial destabilization and aomization driven by surface acoustic waves. *Phys. Fluids*, 20(073103), 2008.

[36] D.J. Collins, O. Manor, A. Winkler, H. Schmidt, J.R. Friend, and L.Y. Yeo. Atomization off thin water films generated by high-frequency substrate wave vibrations. *Phys. Rev. E*, 86 :056312, 2012.

[37] T. Frommelt, M. Kostur, M.and Wenzel-Schäfer, P. Talkner, P. Hänggi, and A. Wixforth. Microfluidic mixing via acoustically driven chaotic advection. *Phys. Rev. Lett.*, 100 :034502, 2008.

[38] S. Girardo, M. Cecchini, F. Bletram, R. Cingolani, and D. Pisignano. Polydimethylsiloxane-libno3 surface acoustic waves micropumps for fluid control into microchannels. *Lab Chip*, 8 :1557–1563, 2008.

[39] M. Cecchini, S. Giardo, D. Psignano, R. Cingolani, and F. Beltram. Acoustic-counterflow microfluidics by surface acoustic waves. *Appl. Phys. Lett.*, 92 :104103, 2008.

[40] W.-K. Tseng, J.-L. Lin, W.-C. Sung, S.-H. Chen, and G.-B. Lee. Active micr-mixers using surface acoustic waves on y-cut 128Â° linbo3. *J. Micromech. Microeng.*, 16 :539–548, 2006.

[41] M.K. Tan, L.Y. Yeo, and J.R. Driend. Rapid fluid flow and mixing induced in micrhcannels using surface acoustic waves. *EPL*, page 47003, 2009.

[42] M. B. Dentry, J.R. Friend, and L.Y. Yeo. Continuous flow actuation beyween external reservoirs in small-scale devices driven by surface acoustic waves. *Lab Chip*, 14 :750, 2014.

[43] R. Shilton, M.K. Tan, and J.R. Yeo, L. an Friend. Particle concentration and mixing in microdrops driven by focused surface acoustic waves. *J. Appl. Phys.*, page 014910, 2008.

[44] J. Shi, X. Mao, D. Ahmed, a. Colletti, and T.J. Huang. Focusing microparticles in a microfluidic channel with standing surface acoustic waves (ssaw). *Lab Chip*, pages 221–223, 2008.

[45] J. Shi, D. Ahmed, X. Mao, S.-C. S. Lin, and T.J. Huang. Acoustic tweezers : patterning cells and microparticles using standing surfac acoustic waves (ssaw). *Lab Chip*, 9 :2890–2895, 2009.

[46] R.V. Raghavan, J.R. Friend, and L.Y. Yeo. Particle concentration via acoustically-microcentrifugation. *Microfluid. Nanofluid.*, 8 :73–84, 2010.

[47] S.B.Q. Tran, P. Marmottant, and P. Thibault. Fast acoustic tweezers for the two-dimensional manipulation of individual particles in microfluidic channels. *App. Phys. Lett.*, 101 :114103, 2012.

[48] X. Ding, S.-C. S. Lin, B. Kiraly, H. Yue, S. Li, J. Shi, S.J. Benkovic, and T.J. Huang. On-chip manipulation of single microparticles, cells and orgnisms using surface acoustic waves. *Proc. Nat. Ac. Sci.*, 109 :11105–11109, 2012.

[49] J. Guo, J.L.W. Li, Y. Chen, L.Y. Yeo, and J.R. Friend. Rf-activated standing surface acoustic wave for on-chip particle manipulation. *IEEE Trans. Microwave Theor. Techn*, 2014.

[50] D.J. Collins, T. Alan, and A. Neild. The particle valve : on demand particle trapping, filtering, and release from microfabricated polydimethylsiloxane membrane using surface acoustic waves. *Appl. Phys. Lett.*, 105 :033509, 2014.

[51] J. Shi, D. Ahmed, X. Mao, A. S.-C. S. Lin, Lawit, and T.J. Huang. Acoustic tweezers : pattening cells and microparticles using standing surface acoustic waves (ssaw). *Lab Chip*, 2009.

[52] T. Franke, S. Braunmuller, L. Schmid, A. Wixforth, and D.A. Weitz. Surface acoustic wave actuated cell sorting (sawacs). *Lab Chip*, 10 :789–794, 2010.

[53] A. Hartmann, M. Stamp, R. Kmeth, S. Buchegger, S. Bernd, B. Saldamli, R. Bugkart, M.F. Schnieder, and A. Wixforth. A novel tool for dynamics cell adhesion studies) the de-adhesion number investigator dani. *Lab Chip*, 14 :542, 2014.

[54] A. Bussoniere, Y. Miron, M. Baudoin, O. Bou Matar, M. Grandbois, P. Charette, and Renaudin A. Cell detachment and label-free cell-sorting using modulated surfae acoustic waves (saws) in droplet-based microfluidics. *Lab Chip*, 14 :3556, 2014.

[55] N. Sivanantha, C. Ma, D.J. Collins, M. Sesen, J. Brenker, R.L. Coppel, A. Neild, and T. Alan. Characterization of adhesive properties of red blood cells using surface acoustic wave induced flows for rapid diagnostics. *Appl. Phys. Lett.*, page 103704, 2014.

[56] X. Ding, Z. Peng, S.-C. S. Lin, M. Geri, S. Li, P. Li, Y. Chen, M. Dao, S. Suresh, and T.J. Huang. Cell seperation using tilted-angle standing surface acoustic waves. *Proc. Nat. Ac. Sci.*, 111 :12992–12997, 2014.

[57] P. Li, Z. Mao, Z. Peng, L. Zhou, Y. Chen, P-H. Huang, C. Truica, J.J. Drbick, W. El-Deiry, M. Dao, S. Suresh, and T.J. Huang. Acoustic separation of circulating tumor cells. *Proc. Nat. Ac. Sci*, 112 :4970–4975, 2015.

[58] F. Guo, P. Li, J.B. French, Z. Mao, H. Zhao, S. Li, N. Nama, J.R. Fick, S.J. Benkovic, and T.J. Huang. Controlling cell-cell interactions using surface acoustic waves. *Proc. Nat. Ac. Sci.*, 2015.

[59] M. Baudoin, P. Brunet, O.B. Matar, and E. Herth. Low energy droplet actuation via modulated surface acoustic waves. *Appl. Phys. Lett.*, 100 :154102, 2012.

[60] A. Bussoniere, M. Baudoin, P. Brunet, and O.B. Matar. Dynamics of sessile and pendant drop excited by surface acoustic waves : gravity effect and correlation between oscillatory and translational motions. *Submitted to Phys. Fluids*, 2015.

[61] D. Beyssen, L.L. Brizoual, and O.E. Alnot. Microfluidic device based on surface acoustic wave. *Sensors and Actuators B*, 118 :280–285, 2006.

[62] J.W.S. Rayleigh. On the capillary phenomena of jets. *Proc. R. Soc. Lond.*, 29 :71–97, 1879.

[63] H. Lamb. *Hydrodynamics*. Cambridge University Press, England, 1932.

[64] C.A. Miller and L.E. Scriven. The oscillations of a fluid droplet immersed in another fluid. *J. Fluid. Mech.*, 32(3) :417, 1968.

[65] A. Prosperetti. Normal-mode analysis for the oscillations of a viscous-liquid drop in an immiscible liquid. *J. de Mécanique*, 19(1) :149–182, 1980.

[66] G.G. Foote. *A theoretical investigation of the dynamics of liquid drops*. PhD thesis, University of Arizona, 1971.

[67] R. Tsamopoulos and R. Brown. Nonlinear oscillations of inviscid drops and bubbles. *J. Fluid Mech.*, 127 :519–537, 1983.

[68] W.R. Smith. Modulations equations for strongly nonlinear oscillations of an incompressible viscous drop. *J. Fluid Mech.*, 654 :141–159, 2010.

[69] M. Strani and F. Sabetta. Free vibrations of a drop in partial contact with a solid support. *J. Fluid Mech.*, 141 :233–247, 1984.

[70] X. Noblin, A. Buguin, and F. Brochard-Wyart. Vibrated sessile frops : Transition between pinned and mobile c ontact line oscillations. *Eur. Phys. J. E.*, 14 :395–404, 2004.

[71] X. Zhou, C. Majidi, and O'Reilly O. Energy efficiency in friction-based locomotion mechanisms for soft and hard robots : slower can be faster. *Nonlinear Dyn.*, 78 :2811–2821, 2014.

[72] B. Issenmann, R. Wunenburger, S. Manneville, and J.P. Delville. Bistability of a compliant cavity induced by acoustic radiation pressure. *Phys. Rev. Lett.*, 97 :074502, 2006.

[73] M. Perez, L. Salvo, M. Suéry, Y. Bréchet, and M. Papoular. Contactless measurement of measurement by oscillations of gas-levitated drops. *Phys. Rev. E*, 61(3) :2669–2675, 2000.

[74] K. Miyamoto, S. Nagamoto, Y. Matsui, and S. Shiokawa. Nonlinear vibration of liquid droplet by surface acoustic wave excitation. *Jpn. J. Appl. Phys.*, 41 :3465–3468, 2002.

[75] D. Bonn, J. Eggers, J. Indekeu, J. Meunier, and E. Rolley. Wetting and spreading. *Rev. Mod. Phys.*, 81 :739–805, 2009.

[76] M. Faraday. On a peculiar class of acoustical figures, and on certain forms assumed by groups of particles upon vibrating elastic surfaces. *Phil. Trans. R. Soc.*, 121 :299–340, 1831.

[77] L.D. Landau and Lifshitz. *Course of theoretical Physics, Mechanics.* Pergamon Press, New York, 1959.

[78] M.R. Schroeder. The schroeder frequency revisited. *J. Acoust. Soc. Am.*, 99(5) :3240–3241, 1996.

[79] A Riaud, M. Baudoin, J.L. Thomas, and O.B. Bou Matar. Cyclones and attractive streaming generated by acoustical vortices. *Phys. Rev. E*, page 013008, 2014.

[80] A. Riaud, J.-L. Thomas, E. Charron, A. BussoniÃ¨re, O.B. Matar, and M. Baudoin. Anisotropic swirling surface acoustic waves synthesis by inverse filter for on-chip generation of acoustical vortices. *accepted for publication in Phys. Rev. Appl.*, 2015.

[81] A. Riaud, J.-L. Thomas, M. Baudoin, and O.B. Matar. Taming the degeneracy of bessel beams at anisotropic-isotropic interface : toward 3d control of confined vortical waves. *Submitted to Phys. Rev. X*, 2015.

[82] M. Tanter, J.-L. Thomas, and M. Fink. Time reversal and the inverse filter. *J. Acoust. Soc. Am.*, 108 :223–234, 2000.

[83] L. Allen, M.W. Beijersbergen, R.J.C. Spreeuw, and J.P. Woerdman. Orbital angular momentum of light and the transformation of laguerre-gaussian laser modes. *Phys. Rev. A*, 45 :8185–8189, 1992.

[84] B.T. Hefner and P.L. Marston. An acoustical helicoidal wave transducer with applications for the alignment of ultrasonic and underwater systems. *J. Acoust. Soc. Am.*, 106 :3313–3316, 1999.

[85] Philip L. Marston. Axial radiation force of a bessel beam on a sphere and direction reversal of the force. *J. Acoust. Soc. Am*, 120(6) :3518–3524, 2006.

[86] D. Baresch, J.L. Thomas, and R. Marchiano. Observation of a single-beam gradient force acoustical trap for elastic particles : acoustical tweezers. *ArXiv*, page 1411.1912, 2014.

[87] D. G. Grier. A revolution in optical manipulation. *Nature*, 424 :810 – 816, 2003.

[88] A.T. O'Neil and M.J. Padgett. Three-dimensional optical confinement of micron-sized metal particles and the decoupling of the spin and orbital angular momentum within an optical spanner. *Optics Communications*, 185 :139–143, 2000.

[89] H. Rubinsztein-Dunlop, T.A. Nieminen, M.E.J. Friese, and N.R. Heckenberg. Optical trapping of absorbing particles. *Adv. Quantum Chem.*, 30 :469 – 492, 1998.

[90] J. Arlt and M. J. Padgett. Generation of a beam with a dark focus surrounded by regions of higher intensity : the optical bottle beam. *Opt. Lett.*, 25(4) :191–193, Feb 2000.

[91] H. He, M.E.J. Friese, N.R. Heckenberg, and H. Rubinsztein-Dunlop. Direct observation of transfer of angular momentum to absorptive particles from a laser beam with a phase singularity. *Phys. Rev. Lett.*, 75 :826–829, 1995.

[92] J.L. Thomas and R. Marchiano. Pseudo angular momentum and topologicla charge conservation for nonlinear acoustical vortices. *Phys. Rev. Lett.*, 91(24) :244302, 2003.

[93] Z. Bouchal, J. Wagner, and M. Chlup. Self-reconstruction of a distorted nondiffracting beam. *Optics Communications*, pages 207–211, 1998.

[94] F. O. Fahrbach and A. Rohrbach. Propagation stability of self-reconstructing bessel beams enables contrast-enhanced imaging in thick media. *Nature Com.*, page 632, 2011.

[95] A. Ginenko, P.D. Wilcox, C.R.P. Courtney, and B.W. Drinkwater. Proof of principle study of ultrasonic particle manipulation by a circular array device. *Proc. Roy. Soc. A*, 468 :3571–3586, 2012.

[96] C.R.P. Courteny, B.W. Drinkwater, C.E.M. Demore, S. Cochran, A. Grenienko, and P.D. Wilcox. Dexterous manipulation of microparticles using bessel-dunction acoustic pressure fields. *2013*, page 123508, Appl. Phys. Lett.

[97] J. Zhou, M. DeMiguel-Ramos, L. Garcia-Gancedo, E. Iborra, J. Olivares, H. Kin, J.K. Luo, A.S. Elhady, S.R. Dong, D.M. Wang, and Y.Q. Fu. Characterisation of aluminium nitride films and surface acoustic wave devices for microfluidic applications. *Sensors and Actuators B*, pages 948–992, 2014.

[98] J. Hao, J. Zhou, X. He, W. Wang, H. Guo, S. Dong, D. Wang, Y. Xu, J. Geng, J.K. Luo, and W.I. Milne. Flexible surface acoustic wave resonators build on disposable plastic film for electronics and lab-on-a-chip applications. *Scientific reports*, 3 :2140, 2013.

[99] Y. Liu, Y. Li, A.M. El-Hady, C. Zhao, J.F. Du, Y. Liu, and Y.Q. Fu. Flexible and bendable acoustofluidcs based on zno film coated aluminium foil. *Sensors and Actuators B*, pages 230–235, 2015.

[100] J.M. Ottino. *The kinematics of mixing : stretching, chaos, and transport.* Cambridge Texts in Applied Mathematics, 1989.

[101] A.J. Chorin. *Vorticity and turbulence*, volume 103. Springer, 1994.

[102] C. Gmelin and U. Rist. Active control of laminar-turbulent transition using instantaneous vorticity signals at the walls. *Phys. Fluids*, 13, 2001.

[103] Q. Zhu, M.J. Wolfgang, D.K.P. Yue, and M.S. Triantafyllou. Three-dimensional flow structures and vorticity control in fish-like swimming. *J. Fluid Mech.*, 468 :1–28, 2002.

[104] L. A. Herzenberg, R. G. Sweet, and L. A. Herenberg. Fluorescence-actived Cell Sorting. *Scientific American*, 234 :108–117, 1976.

[105] S Miltenyi, W Müller, W Weichel, and a Radbruch. High gradient magnetic cell separation with MACS. *Cytometry*, 11(2) :231–8, January 1990.

[106] Daniel R Gossett, Westbrook M Weaver, Albert J Mach, Soojung Claire Hur, Henry Tat Kwong Tse, Wonhee Lee, Hamed Amini, and Dino Di Carlo. Label-free cell separation and sorting in microfluidic systems. *Analytical and bioanalytical chemistry*, 397(8) :3249–67, August 2010.

[107] Lotien Richard Huang, Edward C Cox, Robert H Austin, and James C Sturm. Continuous particle separation through deterministic lateral displacement. *Science*, 304(5673) :987–90, May 2004.

[108] Masumi Yamada and Minoru Seki. Hydrodynamic filtration for on-chip particle concentration and classification utilizing microfluidics. *Lab on a chip*, 5(11) :1233–9, November 2005.

[109] F F Becker, X B Wang, Y Huang, R Pethig, J Vykoukal, and P R Gascoyne. Separation of human breast cancer cells from blood by differential dielectric affinity. *Proceedings of the National Academy of Sciences of the United States of America*, 92(3) :860–4, January 1995.

[110] M D Vahey and J Voldman. An equilibrium method for continuous-flow cell sorting using dielectrophoresis. *Analytical chemistry*, 80(9) :3135–43, May 2008.

[111] K. Dholakia1 MM. P. MacDonald, G. C. Spalding. Microfluidic sorting in an optical lattice. *Nature Biotechnology*, 426(1) :421–424, 2003.

[112] Alexandr Jonás and Pavel Zemánek. Light at work : the use of optical forces for particle manipulation, sorting, and analysis. *Electrophoresis*, 29(24) :4813–51, December 2008.

[113] Robert Carlson, Christopher Gabel, Shirley Chan, Robert Austin, James Brody, and James Winkelman. Self-Sorting of White Blood Cells in a Lattice. *Physical Review Letters*, 79(11) :2149–2152, September 1997.

[114] Gonghao Wang, Wenbin Mao, Rebecca Byler, Krishna Patel, Caitlin Henegar, Alexander Alexeev, and Todd Sulchek. Stiffness Dependent Separation of Cells in a Microfluidic Device. *PLoS ONE*, 8(10) :e75901, October 2013.

[115] Thomas Laurell, Filip Petersson, and Andreas Nilsson. Chip integrated strategies for acoustic separation and manipulation of cells and particles. *Chemical Society reviews*, 36(3) :492–506, March 2007.

[116] Ye Ai, Claire K Sanders, and Babetta L Marrone. Separation of Escherichia coli Bacteria from Peripheral Blood Mononuclear Cells Using Standing Surface Acoustic Waves. *Analytical chemistry*, 85(19) :9126–9134, October 2013.

[117] Aaron Sin, Shashi K Murthy, Alexander Revzin, Ronald G Tompkins, and Mehmet Toner. Enrichment using antibody-coated microfluidic chambers in shear flow : model mixtures of human lymphocytes. *Biotechnology and bioengineering*, 91(7) :816–26, September 2005.

[118] Keon Woo Kwon, Sung Sik Choi, Sang Ho Lee, Byungkyu Kim, Se Na Lee, Min Cheol Park, Pilnam Kim, Se Yon Hwang, and Kahp Y Suh. Label-free, microfluidic separation and enrichment of human breast cancer cells by adhesion difference. *Lab on a chip*, 7(11) :1461–8, November 2007.

[119] Tohid Fatanat Didar and Maryam Tabrizian. Adhesion based detection, sorting and enrichment of cells in microfluidic Lab-on-Chip devices. *Lab on a chip*, 10(22) :3043–53, November 2010.

[120] W Kühne. Uber das Trypsin (Enzym des Pankreas). *Verhandlungen des naturhistorisch-medicinischen Vereins zu Heidelberg, new series*, 1(3) :194–198, 1877.

[121] Leonard Weiss. The measurement of cell adhesion. *Experimental Cell Research*, 8(0) :141 – 153, 1961. Cell Movement and Cell Contact.

[122] S Usami, H H Chen, Y Zhao, S Chien, and R Skalak. Design and construction of a linear shear stress flow chamber. *Annals of biomedical engineering*, 21(1) :77–83, January 1993.

[123] Matthias F Schneider, Zeno Guttenberg, Stefan W Schneider, Kumudesh Sritharan, Vanessa M Myles, Umut Pamukci, and Achim Wixforth. An acoustically driven microliter flow chamber on a chip (muFCC) for cell-cell and cell-surface interaction studies. *Chemphyschem : a European journal of chemical physics and physical chemistry*, 9(4) :641–5, March 2008.

[124] Andreas Hartmann, Melanie Stamp, Ralf Kmeth, Sascha Buchegger, Bernd Stritzker, Belma Saldamli, Rainer Burgkart, Matthias F Schneider, and Achim Wixforth. A novel tool for dynamic cell adhesion studies - the De-Adhesion Number Investigator DANI. *Lab on a chip*, 14(3) :542–6, December 2013.

[125] Hang Lu, Lily Y Koo, Wechung M Wang, Douglas A Lauffenburger, Linda G Griffith, and Klavs F Jensen. Microfluidic Shear Devices for Quantitative Analysis of Cell Adhesion. *Analytical Chemistry*, 76(18) :5257–5264, 2004.

[126] Andreas Lenshof and Thomas Laurell. Continuous separation of cells and particles in microfluidic systems. *Chemical Society reviews*, 39(3) :1203–17, March 2010.

[127] Shih-Kang Fan, Po-Wen Huang, Tsu-Te Wang, and Yu-Hao Peng. Cross-scale electric manipulations of cells and droplets by frequency-modulated dielectrophoresis and electrowetting. *Lab on a chip*, 8(8) :1325–31, August 2008.

[128] Gaurav J Shah, Aaron T Ohta, Eric P-Y Chiou, Ming C Wu, and Chang-Jin C J Kim. EWOD-driven droplet microfluidic device integrated with optoelectronic tweezers as an automated platform for cellular isolation and analysis. *Lab on a chip*, 9(12) :1732–9, June 2009.

[129] Gaurav J Shah, Jeffrey L Veale, Yael Korin, Elaine F Reed, H Albin Gritsch, and Chang-Jin Cj Kim. Specific binding and magnetic concentration of CD8+ T-lymphocytes on electrowetting-on-dielectric platform. *Biomicrofluidics*, 4(4) :44106, January 2010.

[130] Jean-Christophe Baret, Oliver J Miller, Valerie Taly, Michaël Ryckelynck, Abdeslam El-Harrak, Lucas Frenz, Christian Rick, Michael L Samuels, J Brian Hutchison, Jeremy J Agresti, Darren R Link, David a Weitz, and Andrew D Griffiths. Fluorescence-activated droplet sorting (FADS) : efficient microfluidic cell sorting based on enzymatic activity. *Lab on a chip*, 9(13) :1850–8, July 2009.

[131] Jean Berthier. *Microdrops and Digital Microfluidics*. William Andrews Publications, 1st editio edition, 2013.

[132] J Thomas Parsons, Alan Rick Horwitz, and Martin A Schwartz. Cell adhesion : integrating cytoskeletal dynamics and cellular tension. *Nature reviews Molecular cell biology*, 11(9) :633–643, 2010.

[133] SA Safran, N Gov, A Nicolas, US Schwarz, and T Tlusty. Physics of cell elasticity, shape and adhesion. *Physica A : Statistical Mechanics and its Applications*, 352(1) :171–201, 2005.

[134] Adrien Bussonnière, Alan Renaudin, Yannick Miron, Michel Grandbois, Michael Baudoin, and Paul Charette. Removal of living cells from biosensing surfaces in droplet-based microfluidics using surface acoustic waves. *Proceedings of Meetings on Acoustics*, 19(1), 2013.

[135] Haiyan Li, James Friend, Leslie Yeo, Ayan Dasvarma, and Kathy Traianedes. Effect of surface acoustic waves on the viability, proliferation and differentiation of primary osteoblast-like cells. *Biomicrofluidics*, 3(3) :34102, January 2009.

[136] Michael Baudoin, Philippe Brunet, Olivier Bou Matar, and Etienne Herth. Low power sessile droplets actuation via modulated surface acoustic waves. *Applied Physics Letters*, 100(15) :154102, 2012.

[137] M. Baudoin, Y. Song, P. Manneville, and C.N. Baroud. Airways reopening through catastrophic events in a hierachical newtork. *Proc. Nat. Ac. Sci.*, 110(3) :859–864, 2013.

[138] Y. Song, M. Baudoin, P. Manneville, and C.N. Baroud. The air-liquid flow in a microfluidic airway tree. *Med. Eng. Phys.*, 33(7) :849–856, 2011.

[139] R. Lenormand, C. Zarcone, and A. Sarr. Mechanisms of the displacement of one fluid by another in a network of capillary ducts. *J. Fluid Mech.*, 135 :337–353, 1983.

[140] M.M. Dias and A.C. Payatakes. Network models for two-phase flow in porous media Part 1. Immiscible microdisplacement of non-wetting fluids. *J. Fluid Mech.*, 164 :305–336, 1986.

[141] J. Stark and M. Manga. The motion of long bubbles in a network of tubes. *Transport in Porous Media*, 40 :201–218, 2000.

[142] W. Engl, M. Roche, A. Colin, P. Panizza, and A. Ajdari. Droplet Traffic at a Simple Junction at Low Capillary Numbers. *Phys. Rev. Lett.*, 95 :208304, 2005.

[143] Nicolas Champagne, Romain Vasseur, Adrien Montourcy, and Denis Bartolo. Traffic jams and intermittent flows in microfluidic networks. *Phys. Rev. Lett.*, 105 :044502, 2010.

[144] S.H. Davis and L.M. Hocking. Spreading and imbibition of viscous liquid on a porous base. *Phys. fluids*, 11 :48–57, 1999.

[145] Martin Rost, Lasse Laurson, Martin Dube, and Mikko Alava. Fluctuations in fluid invasion into disordered media. *Phys. Rev. Lett.*, 98 :054502, 2007.

[146] William A. Engle and the Committee on Fetus & Newborn. Surfactant-Replacement Therapy for Respiratory Distress in the Preterm and Term Neonate. *Pediatrics*, 121 :419–432, 2008.

[147] E. R. Weibel. *The pathway for oxygen.* Harvard U. press, Cambridge, MA., USA, 1984.

[148] F.F. Espinosa and R.D. Kamm. Bolus dispersal through the lungs in surfactant replacement therapy. *J. Appl. Physiol.*, 86 :391–410, 1999.

[149] K.J. Cassidy, N. Gavriely, and J.B. Grotberg. Liquid plug flow in straight and bifurcating tubes. *J. Biomech. Eng.*, 123 :580–589, 2001.

[150] Y. Zheng, J.C. Anderson, V. Suresh, and J.B. Grotberg. Effect of gravity on liquid plug transport through an airway bifurcation model. *J. Biomech. Eng., Transactions ASME*, 127 :798–806, 2005.

[151] C.P. Ody, C.N. Baroud, and E. de Langre. Transport of wetting liquid plugs in bifurcating microfluidic channels. *J. Colloid Interface Sci.*, 308(1) :231–238, 2007.

[152] Y. Song, P. Manneville, and C.N. Baroud. Local interactions and the global organization of a two-phase flow in a branching tree. *Phys. Rev. Lett.*, 105 :134501, 2010.

[153] Y. Song, M. Baudoin, P. Manneville, and C.N. Baroud. The air-liquid flow in a microfluidic airway tree. *Medical Eng. and Phys.*, 2011.

[154] J.B. Grotberg and O.E. Jensen. Biofluid mechanics in flexible tubes. *Annu. Rev. Fluid Mech.*, 36 :121–147, 2004.

[155] M. Wysocki, M.N. Fiamma, C. Straus, C.S. Poon, and T. Similowski. Chaotic dynamics of resting ventilatory flow in humans assessed through noise titration. *Respiratory physiology & neurobiology*, 153 :54–65, 2006.

[156] A.M. Alencar, S.V. Buldyrev, A. Majumdar, H.E. Stanley, and B. Suki. Avalanche Dynamics of Crackle Sound in the Lung. *Phys. Rev. Lett.*, 87 :88101, 2001.

[157] A.M. Alencar, S.P. Arold, S.V. Buldyrev, A. Majumdar, D. Stamenović, H.E. Stanley, and B. Suki. Dynamic instabilities in the inflating lung. *Nature*, 417 :809–811, 2002.

[158] A. Majumdar, A.M. Alencar, S.V. Buldyrev, Z. Hantos, H.E. Stanley, and B. Suki. Fluid transport in branched structures with temporary closures : A model for quasistatic lung inflation. *Phys. Rev. E*, 67 :031912, 2003.

[159] J. Bico and D. Quéré. Falling slugs. *J. Colloid Interface Sci.*, pages 262–264, 2001.

[160] R.L. Hoffman. Study of advancing interface. a. interface shape in liquid-gas systems. *J. Colloid Interface Sci.*, 50(2) :228–241, 1975.

[161] L.H. Tanner. Spreading of silicone oil drops on horizontal surfaces. *J. Phys. D*, 12(9) :1473, 1979.

[162] F.P. Bretherton. The motion of long bubbles in tubes. *J. Fluid Mech.*, 10(2) :166–188, 1961.

[163] A.L. Hazel and M. Heil. The steady propagation of a semi-infinite bubble into a tube of elliptical or rectangular cross-section. *J. Fluid Mech.*, 470 :91–114, 2002.

[164] F.M. White. *Viscous Fluid Flow, 2nd edition.* Mc Graw-Hill Science, 1991.

[165] P. Aussillous and D. Quéré. Quick deposition of a fluid on the wall of a tube. *Phys. Fluids*, 12(10) :2367–2371, 2000.

[166] A. de Lózar, A.L. Hazel, and A. Juel. Scaling properties of coating flows in rectangular channels. *Phys. Rev. Lett.*, 99(23), 2007.

[167] H. Fujioka, S. Takayama, and J.B. Grotberg. Unsteady propagation of a liquid plug in a liquid-lined straight tube. *Phys. Fluids*, 20 :062104, 2008.

[168] R. Chebbi. Deformation of advancing gas-liquid interfaces in capillary tubes. *J. Colloid Interface Sci.*, 265(1) :166–173, 2003.

[169] L. Barouiba, E. Dehandschoewercker, and J.W.M. Bush. Violent expiratory events : on coughing and sneezing. *J. Fluid Mech.*, 745 :537–563, 2014.

[170] C. Isenberg. *The science of soap films and soap bubbles.* Dover Publications, 1978.

[171] J. Egger and E. Villermaux. Rep. prog. phys. *Physics of liquid jets*, 1978.

[172] P.G. de Gennes, F. Brochard-Wyart, and D. Quéré. *Capillarity and Wetting Phenomena.* Springer, 2004.

[173] M. A. DuprÃ©. SixiÃ¨me mÃ©moire sur la thÃ©orie mÃ©canique de la chaleur. *Ann. Chim. Phys.*, 4(11) :194–220.

[174] Lord Rayleigh. Some applications of photography. *Nature*, (44) :249–254, 1891.

[175] W.E. Ranz. Some experiments on the dynamics of liquid films. *J. Appl. Phys.*, 30 :1950–1955, 1950.

[176] G.I. Taylor. The dynamcs of thin sheets of fluid. iii. disintegration of fluid sheets. *Proc. Roy. Soc. Lond. Ser. A*, 253 :313–321, 1959.

[177] F.E.C. Culick. Comments on a ruptures soap film. *J. Appl. Phys.*, 31 :1128–1129, 1960.

[178] N. Savva and J.W.M. Bush. Viscous sheet retractation. *J. Fluid Mech.*, 626 :211–240, 2009.

[179] Donald E. Spiel. Acoustical Measurements of Air Bubbles Bursting at a Water Surface : Bursting Bubbles as Helmholtz Resonators. *Journal of Geophysical Research*, 97 :11443–11452, 1992.

[180] Grant B Deane. Determining the bubble cap film thickness of bursting bubbles from their acoustic emissions. *The Journal of the Acoustical Society of America*, 133(February 2013) :EL69–75, 2013.

[181] V. Vidal, J.-C. Géminard, T. Divoux, and F. Melo. Acoustic signal associated with the bursting of a soap film which initially closes an overpressurized cavity. *The European Physical Journal B*, 54(3) :321–339, December 2006.

[182] V. Vidal, M. Ripepe, T. Divoux, D. Legrand, J. C. Géminard, and F. Melo. Dynamics of soap bubble bursting and its implications to volcano acoustics. *Geophysical Research Letters*, 37(7), 2010.

[183] Junqi Ding, Felicia W. Tsaur, Alex Lips, and Adnan Akay. Acoustical observation of bubble oscillations induced by bubble popping. *Physical Review E - Statistical, Nonlinear, and Soft Matter Physics*, 75(4) :1–7, 2007.

[184] G.B. Whitham. *Linear and nonlinear waves.* Wiley (New York), 1974.

[185] P.M.and Ingard K.U. Morse. *Theoretical acoustics.* Princeton Univsersity Press, 1986.

[186] J.R. Friend and L.Y. Yeo. Microscale acoustofluidics : Microfluidics driven via acoustics and ultrasonics. *Rev. Mod. Phys.*, 83 :647–704, 2011.

[187] S.-C. Steven Lin, X. Mao, and T.J. Huang. Surface acoustic wave saw acoustophoresis : now and beyond. *Lab Chip*, 12 :2766–2770, 2012.

[188] L.Y. Yeo and J.R. Friend. Surface acoustic wave microfluidics. *Ann. Rev. Fluid Mech.*, 46 :379–406, 2014.

[189] K.F. Rabe, S. Hurd, A. Anzueto, P.J. Barnes, S.A. Buist, P. Calverley, Y. Fukuchi, C. Jenkins, R. Rodriguez-Roisin, . Van Weel, and J. Zielinski. Global strategy for the diagnosis, management and prevention of chronic obstructive pulmonary disease. *Am. J. Resp. and Crit. Care Med.*, 176(6) :532–555, 2007.

[190] J.C. Hogg, F. Chu, S. Utokaparch, R. Wood, W.M. Elliott, L. Buzatu, M. Ruben, R.M. Cherniack, R.M. Rogers, M.D. Sciurba, F.C. abd Harvey, O. Coxson, and P.D. ParÃ©.

The nature of small-airway obstruction in chronic obstructive pulmonary disease. *N. Engl. J. Med.*, 350 :2645–2653, 2004.

[191] J. Anthonisen, N.R. abd Manfreda, C.P.W. Warren, E.S. Hershfield, G.K.M. Harding, and N.A. Nelson. Antibiotic therapy in exacerbations of chronic obstructive pulmonary disease. *Ann. Intern. Med.*, 106(2) :196–204, 1987.

[192] Z. Hantos, T.J. Asztalos, A. Adamicza, A.M. Alencar, and A.S.B. Majumdar. Acoustic evidence of airway opening during recruitment in excised dog lungs. *J. Appl. Physiol.*, 97 :592–598, 2004.

[193] A. Majumdar, A.M. Alencar, S.V. Budyrev, B.Z. Hantos, H.E. Stanley, and B. Suki. Characterization of the branching structure of the lung from macsotropic pressure-volume measurements. *Phys. Rev. Lett.*, 87 :058102, 2001.

[194] F.F. Espinosa and R.D. Kamm. Bolus dispersal through the lungs in surfactant replacement therapy. *J. Appl. Phys.*, 86(1) :391–410, 1999.

[195] K.J. Cassidy, N. Gavriely, and J.B. Grotberg. Liquid plug flow in straight and bifurcating tubes. *J. Biomech. Eng.*, 123(6) :580–589, 1001.

[196] Y. Zheng, J.C. Anderson, V. Suresh, and J.B. Grotberg. Effect of gravity on liquid plug transport through an airway bifurcation model. *J. Biomech. Eng.*, 127(5) :798–806, 2005.

[197] J.B. Grotberg and O.E. Jensen. Biofluid mechanics in flexible tubes. *J. Fluid Mech.*, 36 :121–147, 2000.

[198] P.D. Howell, Waters; S.L., and J.B. Grotber. The propagation of a liquid bolus along a liquid-lined flexible tube. *J. Fluid. Mech.*, 406 :339–335, 2000.

[199] J.B. Grotber and O.E. Jensen. Biofluid mechanics in flexible tubes. *Ann. Rev. Fluid Mech.*, 36 :121–147, 2004.

[200] A.M. Alencar, S.P. Arold, S.V. Buldyrev, A. Majumdar, D. Stamenovic, H.E. Stanley, and B. Suki. Physiology : Dyanmic instabilities in the inflating lung. *Nature*, 417 :809–811, 2002.

[201] D.H. Tompsett. A new method for the preparation of bronchopulmonary casts. *Thorax*, 7 :78, 1952.

[202] R.F. Phalen and M.J. Oldham. Tracheobronchial airway structure as revealed by casting techniques. *Am. Rev. Resp. Disease*, 128 :S1–S4, 1983.

[203] R.S. Robinson and J. Russo. 3d airway reconstruction using visible human data set and human casts with comparison to morphometric data. *Anatomical Record*, 292(7) :1028–1044, 2009.

[204] D.E. Jaalouk and J. Lammerding. Mechanotransduction gone awry. *Nat. Rev. Mol. Cell Biol.*, 2009.

[205] N. Bang, J.P. Butler, and D.E. Ingber. Mechanotransduction across the cell surface and through the cytoskeleton. *Science*, 260 :1124–1127, 1993.

[206] Molecular basis of mechanotransduction in living cells. *Physoliogival Rev.*, 81 :685–740, 2001.

[207] C. Hahn and M.A. Schwartz. Mechanotransduction in vascular physiology anf atherogenesis. *Nat. Rev. Mol. Cell Biol.*, 2009.

[208] Sequential shape-and-solder-directed self-assemblu of functional microsystems. *Proc. Nat. Ac. Sci.*, 101(35) :12814–12817, 2004.

[209] H. Van Brussel, J. Peirs, D. Reynaerts, A. Delchambre, G. Reinhart, N. Roth, M. Weck, and E. Zussman. Assembly of microsystems. *CIRP Annals - Manufact. Techn.*, 49(2) :451–472, 2000.

[210] D.O. Popa and Harryn E. S. Micro and mesocale robotic assembly. *J. Manufact. Process*, 6(1) :52–71, 2004.

[211] R.R.A. Syms. Surface tension powered self-assembly of 3d micro-optomechanical structures. *J. Microelect. Syst.*, 8(4) :448–455, 1999.

[212] G.M. Withesides and M. Boncheva. Beyond molecules : self-assembly of mesoscopic and macroscopic components. *Proc. Nat. Ac. Sci.*, 99(8) :4769–4774, 2002.

[213] E.M. Syms, R.R.A. abd Yeatman, V.M. Bright, and G.M. Whitesides. Surface tension-powered self-assembly of microstructures - the state-of-the-art. *J. Microelectromech. Syst.*, 2003.

[214] W. Zheng and H.O. Hacobs. Fabrication of multicoponent microsystems by directed three-dimensional self-assembly. *Adv. Funct. Mat.*, 2005.

[215] S. Mastrangeli, M. adnd Abbasi, V. Varel, C. Van Hoof, J.-P. Celis, J.P. Celis, and K.F.) Bohhringer. Self-assembly from mili- to nanoscales : Methods and applications. *J. Micromech. Miroeng.*, 19(8) :083001, 2009.

[216] M. Mastrangeli, W. Ruythooren, J. Celis, and C. Van Hoof. Challenges for capillary self-assembly of microsystems. *IEEE Trans. Comp., Pack. Man. Techn.*, 1(1) :5674112, 2011.

[217] G. Skidmore, M. Ellis, A. Geisberg, K. Tsui, R. Saini, T. Huang, and J. Randall. Parallel assembly of microsystems using si micro electo mechanical systems. *Microelect. Eng.*, 2003.

[218] A.D. Stroock, S.K. Dertinger, A. Ajdari, I. Mezic, H.A. Stone, and G.M. Whitesides. Chaotix mixer for microchannels. *Science*, 295 :647–651, 2002.

[219] P. Boyland, M. Stremler, and H. Aref. Topological fluid mechanics of point vortex motions. *Phys. D : Nonlinear Phen.*, 175(1-2) :69–95, 2003.

[220] R. Rotunno. The fluid dynamics of tornadoes. *Ann. Rev. Fluid Mech.*, 45 :59–84, 2013.

[221] M. Sfakiotakis, D.M. Lane, and J.B.C. Davies. Review of fish swimming modes for aquatic locomotion. *IEEE J. Oc.Eng.*, 1999.

[222] C.E. Ellington, C.V. Den Berg, A.P. Willmott, and A.L.R. Thomas. Leading-edge vortices in insect flight. *Nature*, 384 :626–630, 1996.

[223] F.E. Fish and G.V. Lauder. Passive and active flow control by swimming fishes and mammals. *Ann. Rev. Fluid Mech.*, 38 :193–224, 2006.

[224] T.Y. Wu. Fish swimming and bird/insect flight. *Ann. Rev. Fluid Mech.*, 43 :25–58.

[225] J.C.L. Chan. The physics of tropical cyclone motion. *Ann. Rev. Fluid Mech.*, 37 :99–128, 2005.

[226] J. Jimenez, A.A. Wray, P.G. Saffman, and R.S. Rogallo. The structure of intense vorticity in isotropic turbulence. *J. Fluid Mech.*, 255 :65–90, 1993.

[227] D.I. Pullin and P.G. Saffman. Vortex dynamics in turbulence. *Annu. Rev. Fluid Mech.*, 30 :31–51, 1998.

[228] A. Gyr, W. Kinzelbach, and A. Tsinover, editors. *Fundamental problematic issued in turbulence*, chapter Turbulent statistical dynamics of a system of point vortices. Springer Basel AG, 1999.

[229] D. Fabre, L. Jacquin, and A. Loof. Optimal perturbations in a four-vortex aircraft wake in counter-rotating configuration. *J. Fluid Mech.*, 2002.

[230] S.M. Hagsater, T.G. Jensen, H. BRuus, and J.P. Kutter. Acoustic resonances in microfluidic chips : full-image micro-piv experiments and numerical simulations. *Lab on a chip*, 7 :1336–1344, 2007.

[231] P.B. Muller, R. Barnkob, M.J.H. Jensen, and H. Bruus. A numerical study of microparticle acoustophoresis driven by acoustic radiation forces and streaming-induced drag forces. *Lab Chip*, 12 :4617–4627, 2012.